

# Interaction of a Turbulent Spot with a Two-Dimensional Cavity

by

**Shuhao Wu**

A thesis submitted to the  
Faculty of Graduate and Postdoctoral Affairs  
in partial fulfillment of the requirements for the degree of

**Master of Applied Science in Mechanical Engineering**

Ottawa-Carleton Institute for Mechanical and Aerospace Engineering  
Department of Mechanical and Aerospace Engineering  
Carleton University  
Ottawa, Ontario  
November, 2021

©Copyright  
Shuhao Wu, 2021

# Abstract

A study with experimental and numerical components is conducted to establish the effect of a two-dimensional surface cavity on the structure and growth rate of a turbulent spot. The spot is artificially created in a two-dimensional laminar boundary layer developing under zero streamwise pressure gradient. Interactions of the turbulent spot and its wake with the Kelvin-Helmholtz rollers of the cavity shear layer are shown to result in significant increases in its lateral and streamwise growth rates. The underlying physics of these developments are identified.

# Acknowledgments

During the third year of my undergraduate studies, I was invited to a scholarship luncheon hosted by the Mechanical and Aerospace Engineering department. If I recall correctly, I was seated besides Prof. Metin I. Yaras. At some point during this event, I told him that one of my favourite subjects in university has been fluid dynamics and that I am looking for opportunities to go further with my studies. Prof. Yaras told me to email him to discuss about research opportunities for undergrads, which I did after a few weeks. This eventually led to at least 1200 emails, along with hundreds, if not thousands, of hours of meetings over the course of both my undergraduate and graduate studies. Through this journey, I feel that not only did I significantly expand my technical knowledge, I have also grown significantly as an individual. Prof. Yaras, I am extremely grateful for all the feedback, advice and encouragement that you have given me!

Of course, this journey was supported by many others. I am thankful for the friendship and assistance of my colleagues: Andrei Bronipolsky, Andrew Copping, Chanon Pretorius, Colin Miyata, Riley Simpson, Ted Gan, Utku Caylan and others. I also appreciate the help that I have received from Alex Proctor, Neil McFadyen, Kevin Sangster and Stephan Biljan for all the university-provided resources and facilities. I am also grateful for all the advice, discussions and opportunities provided by Prof. Mojtaba Ahmadi on some of the extracurricular, but nonetheless technical activities that I partook as a part of my graduates experience. I would like to thank Sergio Roysen, who was my boss at my part-time employment throughout this entire process, for his advice and support with regards to both my continued education as well as my professional development. Finally, I would like to thank Stephanie, for she has patiently supported me through all these years of studies.

# Preface

This is an integrated thesis as defined by Section 12.4 of the 2021-2022 Carleton University Graduate Calendar. The content is reformatted from the following article, which has been published by *Physics of Fluids* and chosen as an *Editor's Pick*:

- S. Wu and M. I. Yaras (2021), “Interaction of a Turbulent Spot with a Two-Dimensional Cavity,” *Physics of Fluids* **33**, 094114  
<https://doi.org/10.1063/5.0062617>

# Table of Contents

<b>Abstract</b>	<b>ii</b>
<b>Acknowledgments</b>	<b>iii</b>
<b>Preface</b>	<b>iv</b>
<b>Table of Contents</b>	<b>v</b>
<b>List of Tables</b>	<b>vii</b>
<b>List of Figures</b>	<b>viii</b>
<b>Nomenclature</b>	<b>xii</b>
<b>1 Background</b>	<b>1</b>
1.1 Basics of Fluid Dynamics in Close Proximity of Solid Surfaces . . . . .	1
<b>2 Introduction</b>	<b>10</b>
2.1 Physics of turbulent spots in boundary layers . . . . .	10
2.2 Physics of the shear layer over a two-dimensional rectangular cavity .	13
<b>3 Experimental setup and data processing</b>	<b>16</b>
<b>4 Computational models</b>	<b>21</b>
4.1 Modeling in the Eulerian reference frame . . . . .	21
4.1.1 Computational domain and boundary conditions . . . . .	21
4.1.2 Base flow and turbulent spot initialization . . . . .	24
4.1.3 Spatial grid . . . . .	25
4.1.4 Solution method . . . . .	26

4.2	Inviscid modeling in the Lagrangian reference frame . . . . .	28
<b>5</b>	<b>Freestream operating conditions, boundary-layer development and cavity flow development without a turbulent spot</b>	<b>32</b>
<b>6</b>	<b>Results and discussion</b>	<b>38</b>
6.1	Development of the turbulent spot upstream of the cavity . . . . .	38
6.2	Development of the turbulent spot over and downstream of the cavity	42
6.3	Development of the leading-edge region of the spot downstream of the cavity . . . . .	45
6.4	Development of spot turbulence over and downstream of the cavity .	47
6.5	Lagrangian modeling of the K-H roller distortion by the disturbance of a turbulent spot . . . . .	51
6.6	Interaction of the turbulent spot with the cavity shear layer along the lateral boundaries of the spot . . . . .	55
6.7	The wake region of the turbulent spot in the presence of feedback-driven oscillations . . . . .	59
<b>7</b>	<b>Conclusions and future work</b>	<b>64</b>
	<b>References</b>	<b>66</b>
	<b>Appendix A Design of a 2D probe traverse system for the experiment</b>	<b>74</b>
	<b>Appendix B Experimental calibrations</b>	<b>78</b>
	B.1 Pitot probe . . . . .	78
	B.2 Hotwire probe . . . . .	79
	<b>Appendix C Custom electronics for the experiment</b>	<b>81</b>
	C.1 Pulse generator . . . . .	81
	C.2 ZOC17 calibration solenoid circuit . . . . .	84
	C.3 ZOC17 channel selector . . . . .	85
	<b>Appendix D Supplemental material on the vortex filament method</b>	<b>91</b>

# List of Tables

3.1	Measurement grid . . . . .	18
4.1	Spatial grid specifications. . . . .	26
B.1	ZOC17/16Px calibration coefficients . . . . .	79

# List of Figures

1.1	Physical interpretation of Rayleigh’s necessary condition for instability via vorticity dynamics illustrated with (a) a non-inflectional and (b) an inflectional velocity profile . . . . .	4
1.2	Boundary layer velocity profiles over an airfoil . . . . .	5
1.3	Concentration of vorticity illustrated for laminar, transitional, and separating boundary layers . . . . .	7
1.4	Airfoil modified with a cavity on its suction side . . . . .	9
1.5	Aircraft wing showing cavity present near the pivot of the spoilers . . . . .	9
1.6	Growth of disturbance in a vorticity sheet through the Kelvin-Helmholtz instability: (a) Initially planar free shear layer;(b) Perturbed shear layer resulting in a sinusoidal pattern due to self-induced motion; (c) Streamwise-periodic amalgamation of shear-layer vorticity into distinct rollers. . . . .	9
2.1	Idealized schematic of a parent hairpin vortex straddled by two younger wavepackets. . . . .	12
2.2	Variation of the dominant Strouhal number with cavity length for laminar, incompressible conditions: ■▲●Sarohia [27]; ▲●Knisely and Rockwell [36]; □△○Basley <i>et al.</i> [37]; × Direct numerical simulation from the present study; + Experiment measurements from the present study. . . . .	14
3.1	Cross-section schematic of the test section. . . . .	17
4.1	Schematic of the computational domains: (a) Simulation 1: turbulent spot initialization; (b) Simulation 2: turbulent spot development without a surface cavity; (c) Simulation 3: turbulent spot development with a surface cavity. . . . .	23

4.2	(a) Streamwise and (b) wall-normal node spacing for Simulation 3. (c) Node spacing in the jet pipe in the direction parallel to the jet flow, where $\xi = 0$ is located at the jet pipe outlet. . . . .	26
4.3	Comparison of the direct numerical simulations of Valtchanov, Brinkerhoff, and Yaras [59] and Jiménez <i>et al.</i> [60]: (a) rates of turbulence-kinetic-energy production, $P^+ = -\overline{u_i u_j^+} \partial \bar{U}^+ / \partial x_j^+$ , and dissipation, $\epsilon^+ = \frac{\partial u_i}{\partial x_j} \frac{\partial u_i}{\partial x_j}^+$ and (b) profiles of streamwise velocity fluctuation. . .	29
4.4	Schematic of the vortex-filament computational model: (a) vortex filament observed at a mature stage of development; (b) a magnified view of segment $\Delta s_m$ identified in (a). . . . .	30
5.1	Wall-normal profile of time-averaged streamwise velocity at the streamwise midpoint location in the cavity ( $L/\theta_s = 46.5$ ). . . . .	35
5.2	Streamwise development of vorticity thickness over the cavity. . . . .	36
5.3	Instantaneous spatial distribution of $\omega'_z \delta_0^* / U_0$ at $z = 0$ . Negative vorticity in this view corresponds to a clockwise sense of rotation. . . . .	37
6.1	Perturbation velocity in the $y$ - $\tau$ , $y$ - $z$ , and $z$ - $\tau$ planes at the experimental measurement planes (a) $x/\delta_0^* = 121.0$ and (b) $x/\delta_0^* = 241.9$ . The $y$ - $\tau$ plane is located at the spot centerline. Dashed line shows the location of the $y$ - $z$ plane. Dotted line shows the location of the $z$ - $\tau$ plane. Black solid lines approximate the perimeter of the spot with $u_{\text{rms}}/U_0 = 0.06$ . Plots are not to scale. . . . .	39
6.2	The turbulent spot upstream of the cavity visualized through isosurfaces of $Q/(U/\delta_0^*)^2 = 2 \times 10^{-4}$ at (a) $\tau = 118$ and (b) $\tau = 301$ . . . . .	42
6.3	Perturbation velocity in the $y$ - $\tau$ , $y$ - $z$ , and $z$ - $\tau$ planes at the experimental measurement planes (a) $x/\delta_0^* = 287.3$ and (b) $x/\delta_0^* = 408.4$ . The $y$ - $\tau$ plane is located at the spot centerline. Dashed line shows the location of the $y$ - $z$ plane. Dotted line shows the location of the $z$ - $\tau$ plane. Black solid lines approximate the perimeter of the spot with $u_{\text{rms}}/U_0 = 0.06$ . Plots are not to scale. . . . .	43
6.4	Variation of spot half-width, $s_{hw}$ , with streamwise location of the spot. . . . .	45
6.5	The turbulent spot visualized through isosurfaces of $Q/(U/\delta_0^*)^2 = 2 \times 10^{-4}$ at $\tau = 451$ (a) in the absence, and (b) in the presence of the cavity. . . . .	47

- 6.6 Magnified view of the H vortices shown in Figure 6.5 overlaid with colour contours of perturbation streamwise velocity on a surface at  $y/\delta_0^* = 3.75$  (a) in the absence, and (b) in the presence of the cavity. 48
- 6.7 Turbulent spot viewed at  $\tau = 484$  with black-colour lines locating the cavity edges. (a,b): top view of isosurfaces of  $Q/(U/\delta_0^*)^2 = 2 \times 10^{-4}$ ; (c,d): bottom view of isosurfaces of  $Q/(U/\delta_0^*)^2 = 2 \times 10^{-4}$ ; (e,f): flood plot of the wall-normal component of perturbation velocity with contours of  $x$  component of perturbation vorticity,  $|\omega'_x|\delta_0^*/U_0$ , corresponding to a value of +0.25 (red colour) and -0.25 (blue colour). . . . . 49
- 6.8 The state of vortex filaments at the end of the simulation period  $\Delta\tau = 22$  subject to (a)  $u'$ , (b)  $v'$ , and (c) in-phase  $u' + v'$  perturbations. . . . . 53
- 6.9 Streamwise growth rate of an initially straight spanwise vortex filament subject to perturbation velocity of varying amplitudes. . . . . 54
- 6.10 A typical inverted vortex pair formed within the cavity visualized through isosurfaces of  $Q/(U/\delta_0^*)^2 = 2 \times 10^{-4}$  at  $\tau = 451$ . (a) Bottom view; (b) side view of only region A; (c) bottom view of only region A. 54
- 6.11 The turbulent spot viewed from the bottom visualized through isosurfaces of  $Q/(U/\delta_0^*)^2 = 2 \times 10^{-4}$  at (a)  $\tau = 539$ , (b)  $\tau = 572$ , and (c)  $\tau = 605$ . . . . . 56
- 6.12 Flood plot of streamwise perturbation velocity in a  $y - z$  plane at  $x/\delta_0^* = 320$  and  $\tau = 572$  with contours of  $Q/(U/\delta_0^*)^2 = 2 \times 10^{-4}$  superimposed. . . . . 56
- 6.13 Variation of spot half-width with streamwise location of the trailing edge of the spot. The  $\gamma$  values denote half-spot spreading angles based on line fits to corresponding segments of data. . . . . 57
- 6.14 The evolution of a K-H roller as it interacts with the wake region, visualized through isosurfaces of  $Q/(U/\delta_0^*)^2 = 2 \times 10^{-4}$  at (a)  $\tau = 705$ , (b)  $\tau = 727$ , and (c)  $\tau = 749$ . Arrow points to the cavity downstream edge. . . . . 61
- 6.15 Perturbation streamwise (a,c,e) and wall-normal (b,d,f) velocity component at  $y/\delta_0^* = 1$ . Dash rectangles follow the same region within the wake as it convects over the cavity downstream edge. Arrow points to the cavity downstream edge. . . . . 61

6.16	Distribution of $u_{\text{rms}}/U_0$ $5.6\delta_0^*$ distance downstream of the cavity downstream edge along the spot centerline: (a) $L/\theta_s = 46.7$ , (b) $L/\theta_s = 54.4$ , and (c) $L/\theta_s = 70.0$ . White solid lines: $u'/U_0 = 0.04$ ; white dashed lines: $u'/U_0 = -0.04$ . . . . .	62
A.1	Two off-the-shelf linear motion systems combined to function as a 2D traverse system . . . . .	76
A.2	The traverse system and its cradle. Detail shows the mounting of the motion systems onto the cradle. . . . .	77
B.1	An instance of the calibration curve of the hotwire probe performed with 20 values of velocity . . . . .	80
C.1	Pulse generator breadboard design . . . . .	84
C.2	Solenoid driver circuit . . . . .	85
C.3	ZOC17 channel selection guide . . . . .	86
C.4	ZOC17 channel selector circuit . . . . .	87

# Nomenclature

$D$	cavity depth (m)
$f$	cavity feedback-driven oscillation frequency (Hz)
$L$	cavity length (m)
$m$	vortex segment index
$N_x$	number of nodes in the streamwise direction in the direct numerical simulation
$N_y$	number of nodes in the wall-normal direction in the direct numerical simulation
$N_z$	number of nodes in the spanwise direction in the direct numerical simulation
$n$	number of spot generation and measurement cycles
$P^+$	non-dimensionalized turbulence-kinetic-energy production rate
$Q$	second invariant of the velocity gradient tensor ( $1/s^2$ )
$\vec{r}_m$	vector distance from vortex segment $m$ (m)
$r_c$	minimum radius of induction by the vortex filament (m)
$St_{\theta_s}$	Strouhal number based on the momentum thickness at the cavity upstream edge, $St_{\theta_s} = f\theta_s/U_0$
$\vec{s}_m$	vector length of vortex segment $m$
$s_{hw}$	turbulent spot half-width (mm)
$t$	time (s)
$U_0$	inlet and free-stream streamwise velocity (m/s)
$\bar{u}$	time-averaged streamwise velocity in the numerical simulation (m/s)
$\tilde{u}$	ensemble-averaged streamwise velocity (m/s)
$u$	instantaneous streamwise velocity (m/s)
$u'$	instantaneous perturbation streamwise velocity (m/s)
$u_{\text{rms}}$	root-mean-square of the velocity fluctuation (m/s)
$u_i, u_j$	instantaneous velocity vector in index notation (m/s)

$u_l$	local undisturbed (laminar) streamwise velocity (m/s)
$u_\tau$	friction velocity (m/s)
$v$	instantaneous wall-normal velocity (m/s)
$v'$	instantaneous perturbation wall-normal velocity (m/s)
$\vec{V}$	instantaneous velocity vector used with the vortex filament method (m/s)
$\vec{V}_{\text{background}}$	background velocity vector used with the vortex filament method (m/s)
$x_{te}$	streamwise coordinate of the turbulent-spot trailing edge (m)
$x^+$	streamwise coordinate in viscous wall units
$x_i, x_j$	coordinate written in index notation (m)
$y$	wall-normal coordinate (m)
$y^+$	wall-normal coordinate in viscous wall units
$z$	spanwise coordinate (m)
$z^+$	spanwise coordinate in viscous wall units
$\delta_0^*$	boundary-layer displacement thickness at the jet coordinate (mm)
$\delta_{\omega z}$	shear-layer vorticity thickness (mm)
$\epsilon^+$	non-dimensionalized turbulence-kinetic-energy dissipation rate
$\eta^+$	Kolmogorov length scale in viscous wall units
$\Gamma$	circulation ( $\text{m}^2/\text{s}$ )
$\Gamma'$	perturbation circulation ( $\text{m}^2/\text{s}$ )
$\gamma$	half-spot spreading angle (deg.)
$\lambda_z$	streak spanwise spacing (m)
$\nu$	kinematic viscosity ( $\text{m}^2/\text{s}$ )
$\rho$	density ( $\text{kg}/\text{m}^3$ )
$\tau$	non-dimensionalized time, $\tau = tU_0/\delta_0^*$
$\tau_w$	wall shear stress
$\theta_s$	boundary-layer momentum thickness at the cavity upstream edge (mm)
$\omega'$	perturbation vorticity
$\zeta$	coordinate that starts at the jet pipe outlet and increases towards its inlet (m)

# Chapter 1

## Background

### 1.1 Basics of Fluid Dynamics in Close Proximity of Solid Surfaces

The dynamics of a fluid in motion is affected by solid boundaries defining the geometry of the flow path. Such boundaries realize this effect through the pressure field and through the resistance to fluid motion prevailing along the solid surfaces. Due to the roughness of solid surfaces, which is present at small scales even on surfaces with a highly polished appearance, adjacent fluid molecules tend to adopt the velocity of the surface. Fluid farther from such surfaces is not affected by this resistance effect. The resultant velocity difference between the fluid adjacent to the solid surface and the fluid far from it results in the development of strain rates and associated viscous shear forces in the flow field near the solid surface. This sheared region of flow is referred to as the boundary layer. The fluid region beyond the boundary layer is conventionally referred to as the free stream. As the interface between the boundary layer and the free stream is approached, the fluid velocity in the boundary layer follows an asymptotic pattern. This asymptotic velocity variation poses a challenge to accurate positioning of this interface, thereby making the thickness of the boundary

layer,  $\delta$ , a somewhat ambiguous parameter. One unambiguous alternative to  $\delta$  is the momentum thickness of the boundary layer,  $\theta$ . This is the thickness of a layer of fluid moving at the local free-stream velocity, the streamwise momentum of which is equal to the deficit of streamwise momentum of the local boundary layer. Both  $\delta$  and  $\theta$  typically tend to increase with streamwise distance along a solid surface owing to the cumulative effect of viscous resistance as the fluid travels along this surface. This streamwise rate of growth of the boundary layer is affected by: the streamwise acceleration/deceleration of the free-stream fluid driven by the streamwise pressure gradient; the relative magnitudes of inertial and viscous forces, the ratio of which is identified as the flow Reynolds number; and the laminar versus turbulent state of the boundary layer. Streamwise free-stream acceleration, higher Reynolds number values, and a laminar state of the boundary layer all promote lower streamwise rate of growth of the boundary layer.

Higher flow Reynolds number values also promote transition of a boundary layer from laminar to turbulent state. In low-turbulence environments, this transition is the result of the boundary layer becoming unstable upon reaching a critical value of flow Reynolds number. The most common boundary-layer instability mode is driven by the viscous forces, and is known as the Tollmien-Schlichting instability. This instability physically manifests itself as streamwise-periodic groupings of spanwise vorticity, which eventually deform into three dimensional structures. This instability does not require an inflection point in the surface-normal variation of streamwise velocity in the boundary layer. When the free-stream fluid is decelerated by an adverse streamwise pressure gradient, an inflection point develops in this velocity profile. This further destabilizes the boundary layer through an inviscid instability mode due to Rayleigh's necessary condition. The physical interpretation of Rayleigh's condition can be qualitatively realized by examining the interaction between local velocity and

vorticity fields. Figure 1.1a shows three parallel sheets of vorticity within a boundary layer without an inflection point in the velocity profile. Absence of an inflection point implies that the vorticity distribution in the surface-normal direction does not have an extremum. At  $t_1$ , the fluid element A is perturbed which prompts it to descend from layer 1 to layer 2. Upon arrival at layer 2, the excess vorticity of element A with respect to its neighbours in layer 2 prompts net downwash on its right-hand side, and net upwash on its left-hand side. This causes the fluid elements B and C to move from their respective vorticity layers to layer 2, where they are identified as B' and C'. As the vorticity of element C' is greater than that of element B', the net induced velocity on element A is upwards, thus returning it to its origin on layer 1. This dynamic is stabilizing, as perturbed fluid elements tend to be returned to their origins. Conversely, if an inflection point is present in the velocity profile, with the inflection point located at layer 2 (Figure 1.1b), the vorticity magnitudes of layer 1 and 3 would be comparable. In this scenario, elements B' and C' would not be able to induce a net upward motion on element A in layer 2 to return it to its origin on layer 1. In essence, the flow would be unstable.

Small disturbances that are always present in a flow environment in one form or another are amplified in an unstable boundary layer. Upon sufficient growth of such disturbances, three-dimensional vortical structures, also known as turbulence eddies, begin to form in the boundary layer. These turbulence eddies affect the velocity field in their immediate vicinity such that inflectional velocity profiles are produced, which as per Rayleigh's condition are inviscid-unstable. This ultimately results in the regeneration of additional vortical structures and the transition of a laminar boundary layer into a turbulent one. The mutual interaction between these turbulence eddies have been the subject of a broad range of studies with a variety of

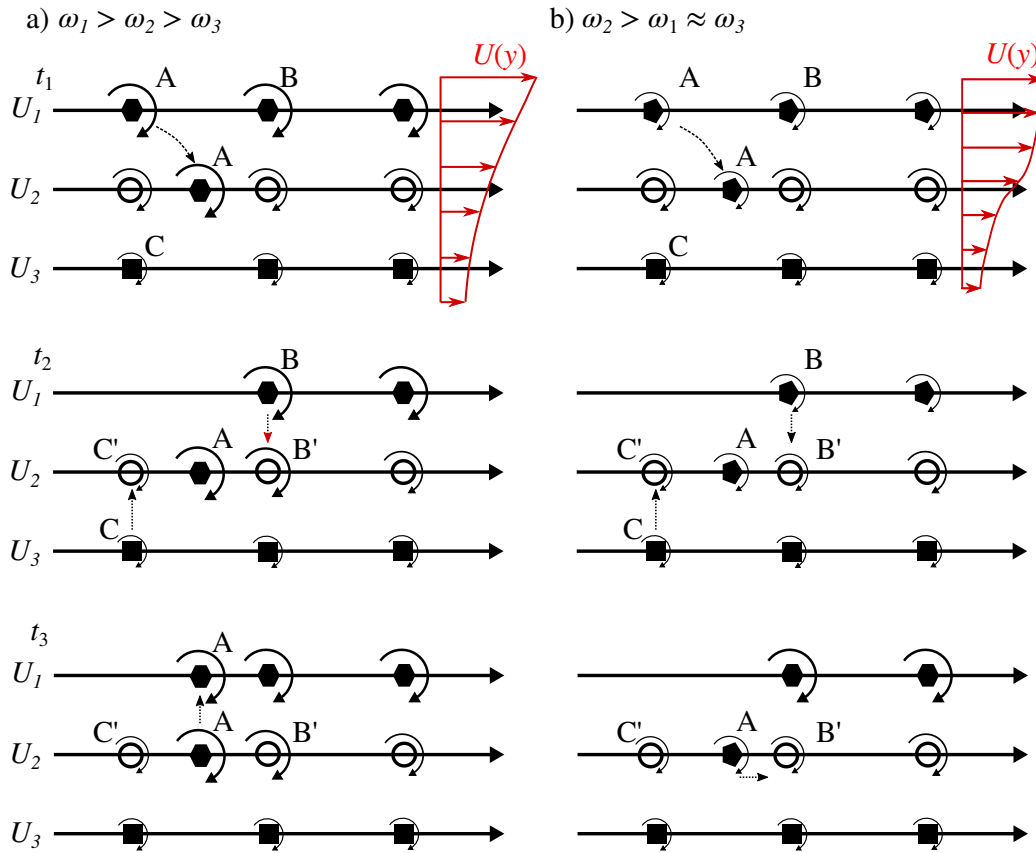


**Figure 1.1:** Physical interpretation of Rayleigh’s necessary condition for instability via vorticity dynamics illustrated with (a) a non-inflectional and (b) an inflectional velocity profile

fluid and flow parameters. The transition process described up to this point is called natural transition, and applies to conditions where the flow field is exposed to small disturbances. In cases where the laminar boundary layer experiences disturbances of relatively larger amplitudes, examples of which are local geometric discontinuities in the flow path, high intensity free-stream turbulence, large surface roughness elements, and large-amplitude surfaces vibration, the boundary layer “bypasses” the natural transition process, and instead transitions more abruptly to a turbulent state through a different transition path. This alternative path of transition is referred to as the bypass transition mode. The laminar-to-turbulent transition process of a boundary layer is notably more complex than this brief description implies. Nonetheless, the

present summary should suffice as a guide for the non-expert reader of this thesis manuscript. Figure 1.2 summarizes the aforementioned concepts in a schematic of the flow field over an airfoil.

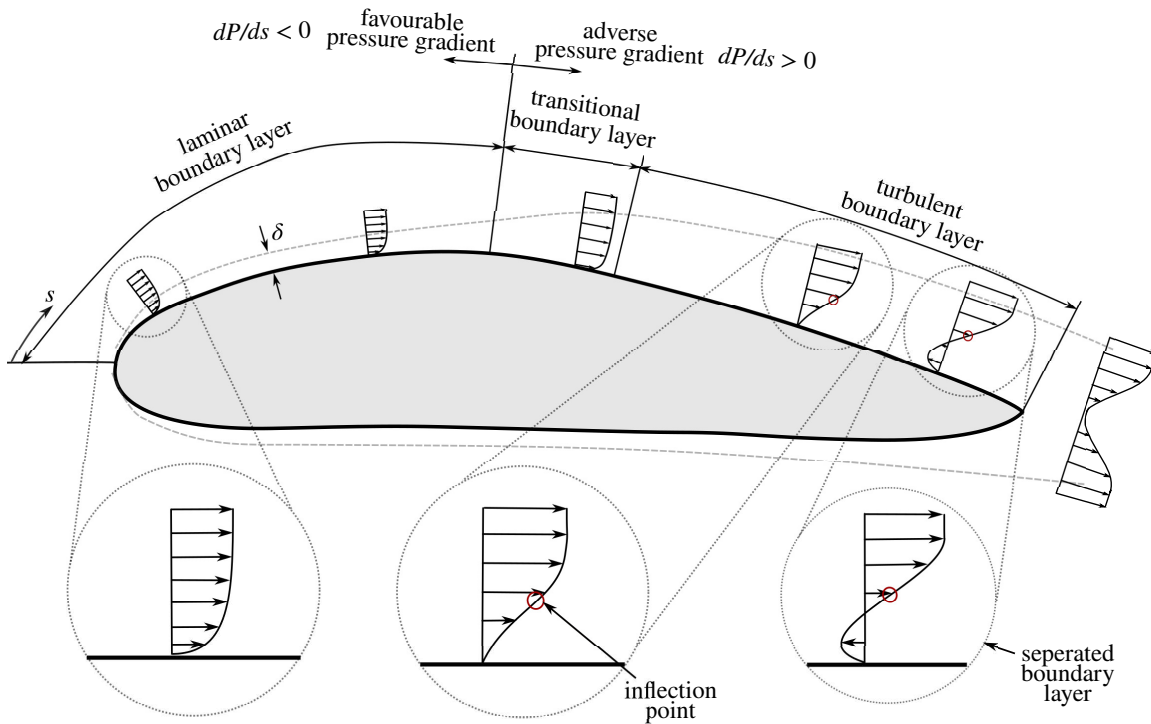


**Figure 1.2:** Boundary layer velocity profiles over an airfoil

In a laminar boundary layer, exchange of streamwise momentum between “layers” of fluid moving within the boundary layer is affected solely by the prevailing viscous shear force, which is fundamentally related to the process of molecular diffusion within the flow field. The local shear force prevailing at any point in the boundary layer acts as a force couple and imparts angular momentum to the boundary-layer fluid. The angular velocity of this local spinning motion of the fluid is quantified as one-half of the curl of the local velocity. The local vorticity vector is aligned with the local angular velocity and is defined to have twice the angular velocity magnitude. As the fluid particle moves within the boundary layer, its vorticity is altered as it is exposed to varying values of shear force during its travel. In a two-dimensional laminar boundary

layer, fluid motion is planar, with the velocity field being a function of only the surface-normal and streamwise spatial directions, as was shown in Figure 1.2. As such, in this type of a boundary layer, the axis of fluid-particle rotation and hence the vorticity vector is perpendicular to this planar fluid motion for all fluid particles. In the presence of instabilities promoting boundary-layer turbulence, this vorticity field of the boundary layer is significantly altered, both in the local magnitude and direction of vorticity, which in part results in the creation of turbulence eddies as described earlier. The mechanism of momentum exchange within a turbulent boundary layer is dominated by the mixing actions of these turbulence eddies, resulting in a surface-normal distribution of vorticity that is, in a time-mean sense, more concentrated near the surface than for the corresponding laminar boundary-layer state. This increased concentration of vorticity in close vicinity of the surface is also reflected in the time-mean surface-normal distribution of streamwise velocity within the boundary layer. Turbulence promotes a fuller shape for this velocity profile. This is schematically illustrated for the boundary layer on the suction side of an airfoil in Figure 1.3.

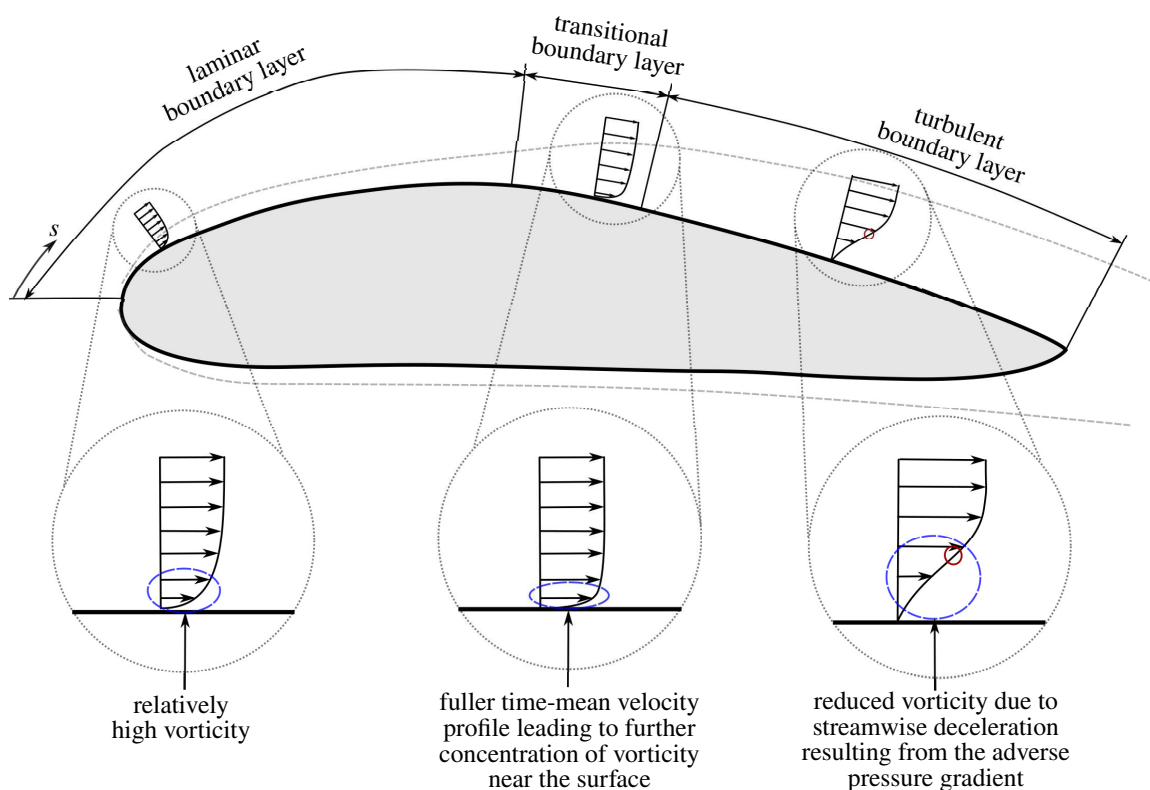


**Figure 1.3:** Concentration of vorticity illustrated for laminar, transitional, and separating boundary layers

As was stated earlier, one possible form of disturbance that may promote transition of a boundary layer to the turbulent state is geometric discontinuities associated with the solid surfaces that define the geometry of the flow path. Geometric discontinuity can take many forms, one of which is an interruption of the solid surface along the streamwise direction by the presence of a cavity or recess. This scenario is schematically illustrated for the example airfoil in Figure 1.4. In practical situations, such cavities may be found along the perimeters of access ports for mechanical systems on aircraft wings as well as along the edges of aircraft control surfaces in their stored configurations such as the cavities illustrated in Figure 1.5. This particular aeronautical application was the original motivation for the present study. The inflectional shape of the velocity distribution in the shear layer over the cavity makes

the flow inviscid unstable in the same manner as was described for a boundary layer under adverse streamwise pressure gradient. As illustrated in Figure 1.6, the initially planar shear layer (Figure 1.6a) is deformed by the inviscid instability mode into a streamwise-sinusoidal pattern (Figure 1.6b). Such deformation of the vorticity sheet exposes parts of the sheet to the faster-moving stream, and the remaining parts to the slower-moving stream. This results in relative streamwise displacement of these parts as illustrated with the straight arrows in Figure 1.6b. This eventually causes the vorticity to amalgamate in a streamwise-periodic fashion to produce distinct “rollers” (Figure 1.6c) at predictable wavelengths. Since the shear layer of the present study develops over a cavity, the rollers that form over it eventually impinge upon the downstream edge, which create pressure oscillations that amplify the initial disturbances within the shear layer at the upstream end of the cavity, completing a feedback loop. The interaction of boundary-layer turbulence with these rollers in the transitional state is the focus of this thesis. It is worth pointing out that the dynamics described for the free shear layer over the cavity fundamentally also apply to the wake of the airfoil where the same inviscid instability mode prevails.

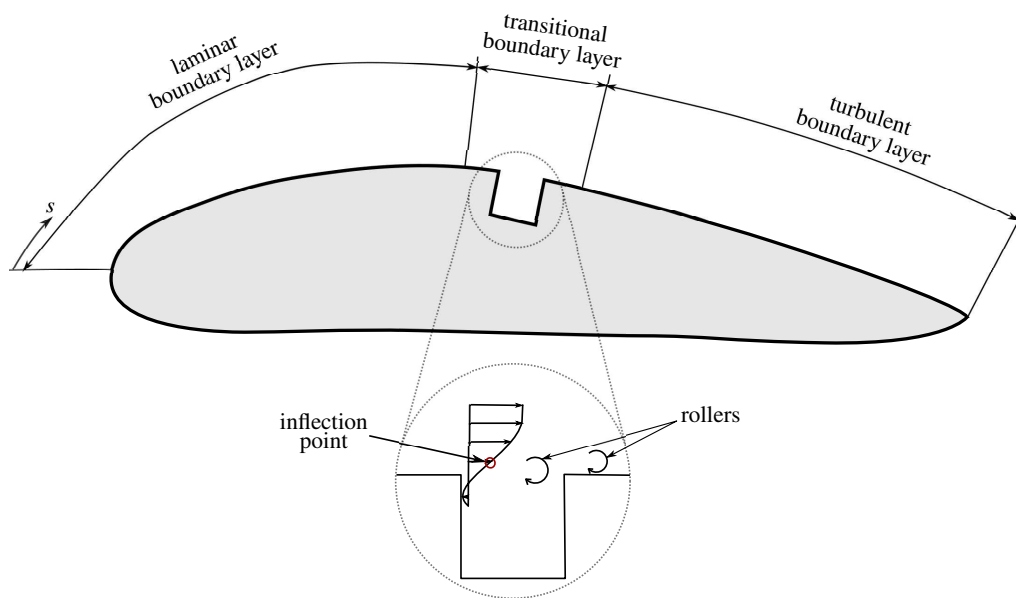


**Figure 1.4:** Airfoil modified with a cavity on its suction side



**Figure 1.5:** Aircraft wing showing cavity present near the pivot of the spoilers<sup>(a)</sup>

<sup>(a)</sup> M., Wrinkler, *Aircraft Wing*, Pexels licensed free-to-use, Jan. 28, 2020. Accessed: Nov. 4, 2021. [Online]. Available: <https://www.pexels.com/photo/aircraft-wing-3639869/>

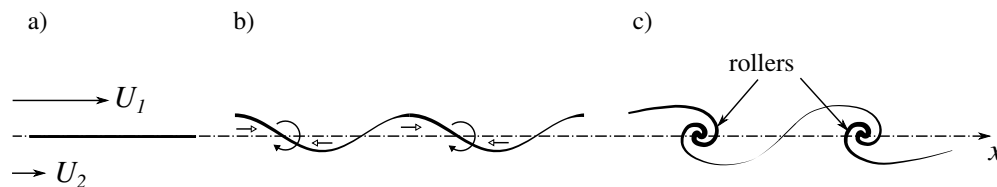


**Figure 1.6:** Growth of disturbance in a vorticity sheet through the Kelvin-Helmholtz instability: (a) Initially planar free shear layer; (b) Perturbed shear layer resulting in a sinusoidal pattern due to self-induced motion; (c) Streamwise-periodic amalgamation of shear-layer vorticity into distinct rollers.

## Chapter 2

# Introduction

### 2.1 Physics of turbulent spots in boundary layers

A typical turbulent spot contains multiple generations of wavepackets of coherent vortical structures [1–3]. Mutual interactions among the wavepackets produce a seemingly random pattern of vortical structures within the spot. However, upon formation, a wavepacket tends to consist of a relatively more organized set of approximately-hairpin-shaped vortical structures [1, 4, 5]. The vortices tend to approximately align in the streamwise direction in groups of three to five, with each hairpin vortex approximately oriented with its streamwise legs extending in the upstream direction and its head lifted away from the solid surface due to self-induction effects [1, 4]. The flow physics underlying the formation of such a wavepacket are more readily traceable along the side edges of a turbulent spot. At these locations, hairpin vortices of prevailing wavepackets locally destabilize the laminar flow field adjacent to the turbulent spot, thereby promoting the formation of new wavepackets [1, 6, 7]. The typical process of destabilization is realized by the formation of streamwise streaks of velocity perturbations, induced by the up- and down-wash motions of the streamwise legs of prevailing mature hairpin vortices, schematically illustrated in Figure 2.1. These

streaks adopt a predictable spanwise spacing dictated by a balance between increased viscous diffusion in small-wavelength perturbations and decreased wall-normal induced velocity in large-wavelength perturbations [8]. The resultant spanwise spacing has a mean value of 100 viscous wall units, with a log-normal probability distribution with a dense range between 60 to 180 viscous wall units [4, 9, 10]. The viscous wall unit is based on the kinematic viscosity,  $\nu$ , density,  $\rho$ , and wall shear stress,  $\tau_w$ , through  $\nu/\sqrt{\tau_w/\rho}$ . The shear layer enveloping each such velocity streak is known to be inviscid unstable to sinuous and varicose modes [11, 12], resulting in streamwise grouping of the vorticity of the shear layer around the streak at predictable wavelengths of several hundred viscous wall unit [4, 13]. These groups of vorticity subsequently develop coherence to form new hairpin vortices as illustrated in Figure 2.1, which shows one of a multitude of spatial arrangements where they straddle the streamwise legs of the parent hairpin vortex [14, 15]. The same fundamental mechanism of new wavepacket formation likely also prevails within the turbulent spot [1]. Albeit, the cause-and-effect relations in the flow development are notably more difficult to discern in these regions in mature spots as multiple wavepackets of different generations, sizes and states of partial/full overlap participate in the process. The noted process of wavepacket formation along the sides of a turbulent spot has been suggested to be a primary mechanism driving the spanwise growth of a turbulent spot [1]. While the rate of this growth is shown to be independent of the original disturbance creating the spot [16], it is also found to negatively correlate with streamwise acceleration of the local freestream [17–19].

Younger generations of wavepackets in the spot are located in closer proximity of the solid surface where they form and convect in the streamwise direction at relatively lower velocity [1]. The older wavepackets are larger, extending as far as several

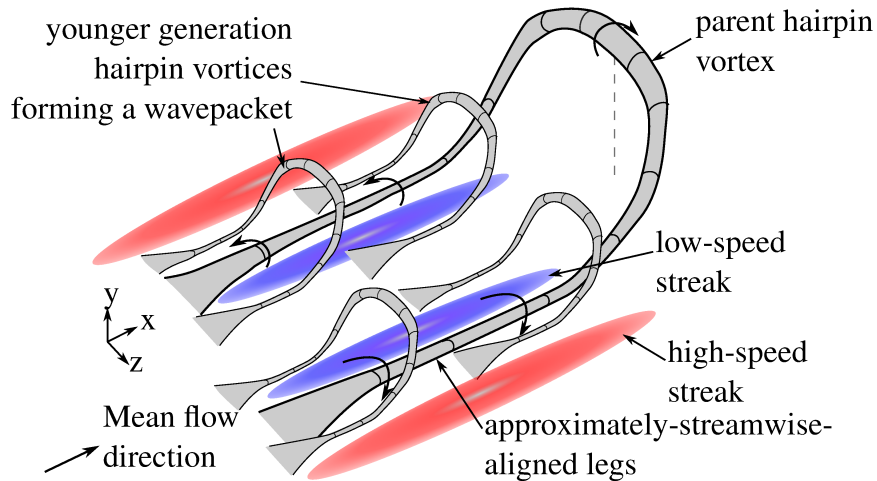


**Figure 2.1:** Idealized schematic of a parent hairpin vortex straddled by two younger wavepackets.

local undisturbed boundary layer thicknesses away from the surface and accordingly convect downstream at higher velocity [16, 20]. Expectedly, this results in the larger wavepackets to preferentially locate near the leading side of the spot, and the spot trailing edge to be populated by younger-generation wavepackets. The noted difference in the leading and trailing edge convection speeds is a primary mechanism driving the streamwise growth of the turbulent spot [17, 20]. The heads of the larger hairpin vortices at the spot leading edge extend over the laminar boundary layer ahead of the spot and promote entrainment of laminar fluid, which further promotes growth of the spot [16, 20].

The turbulent spot is well-known to promote stability or calming effect in its wake, an effect realized by perturbation spanwise vorticity trailing the spot in close proximity of the surface. The downwash induced by this vorticity yields a relatively fuller and thus more stable wall-normal profile of streamwise velocity [1, 21, 22]. Viscous diffusion of this vorticity ensures the streamwise length of the calmed wake to be finite [1]. This effect of the perturbation vorticity is reduced under the influence of favourable streamwise pressure gradients [21].

## 2.2 Physics of the shear layer over a two-dimensional rectangular cavity

In broad terms, the shear layer over a two-dimensional cavity behaves in a manner similar to a free shear layer, with the Kelvin-Helmholtz instability mode promoting streamwise-periodic amalgamation of spanwise vorticity, at times leading to the formation of spanwise vortices (K-H rollers) [23–25]. The length scales deemed relevant to this shear-layer development are cavity length ( $L$ ), cavity depth ( $D$ ), and the boundary-layer momentum thickness at the cavity upstream edge ( $\theta_s$ ) [26]. The streamwise motion within the cavity driven by the shear layer is terminated by the downstream bounding wall of the cavity, resulting in the formation of a primary vortex in the cavity, which scales on the shorter of the  $L$  and  $D$  dimensions [27]. Upon impingement on the downstream edge of the cavity, parts of the K-H rollers are clipped and merged with the recirculating flow within the cavity [28, 29]. The pressure fluctuation generated by the impingement process at the dominant K-H frequency feeds back into the evolution of the cavity shear layer, thus creating a feedback loop to produce notably more distinctive peaks in the pressure and velocity spectra of the cavity shear layer than in an unconfined free shear layer [30, 31]. The natural frequency of the cavity shear layer, expressed as a Strouhal number,  $St_{\theta_s} = f\theta_s/U_0$ , is within the band of frequencies amplified by the Kelvin-Helmholtz instability and varies with  $L/\theta_s$  as shown in Figure 2.2. Three distinct modes are evident, and the  $St_{\theta_s}$  value is noted to decrease with cavity length within each mode. Feedback-driven large-amplitude oscillations are generally not observed for  $L/\theta_s$  values below about 50 [27, 32]. This is attributed to the fact that rollers in these cases do not have enough

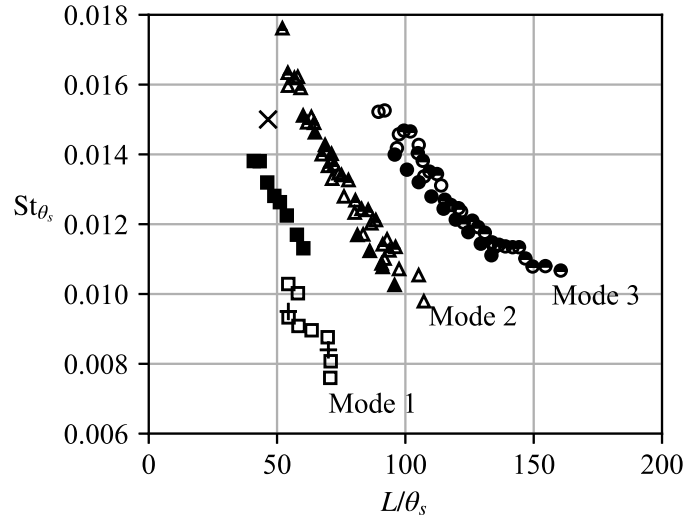


**Figure 2.2:** Variation of the dominant Strouhal number with cavity length for laminar, incompressible conditions:  $\blacksquare$   $\blacktriangle$   $\bullet$  Sarohia [27];  $\triangle$   $\circ$  Knisely and Rockwell [36];  $\square$   $\Delta$   $\circ$  Basley *et al.* [37];  $\times$  Direct numerical simulation from the present study;  $+$  Experiment measurements from the present study.

time to grow to sufficient strength prior to impingement [27, 32]. At times, feedback-driven oscillations and the regular formation of rollers within the cavity shear layers are not observed even for  $L/\theta_s$  values above this threshold [33–35].

In some cases where the cavity shear layer originates from a laminar upstream boundary layer, the cavity shear layer may undergo secondary instabilities that result in the spanwise-way deformation of the K-H rollers prior to impingement [38, 39]. In such cases, upon impingement the rollers are observed to reorganize into spanwise arrays of hairpin vortices [39]. The detailed mechanisms dictating the development of the vorticity field in such instances remain unexplored. In cases where the cavity shear layer originates from a turbulent upstream boundary layer, the formation of spanwise coherent rollers over a cavity tends to be inhibited by spanwise non-uniform deflections of the vorticity sheet induced by hairpin vortices prevailing in the upstream turbulence [39]. Despite this, clusters of small-scale coherent structures are observed

to form in a streamwise-periodic manner at a Strouhal number of  $St_{\theta_s} \approx 0.016$  [40, 41]. Streamwise streaks associated with upstream turbulence are also observed to lose their streamwise coherence beyond the first 1/3rd of the cavity length, which is attributed to the mutual interaction between the newly-formed vortices within the cavity shear layer and the streaks in the prevailing turbulence [39, 42].

Few studies [43, 44] have investigated the effects of a cavity on triggering transition onset in a laminar boundary layer. A cavity appears to trigger transition by amplifying the Tollmien-Schlichting waves prevailing in the approaching boundary layer as well as through instability modes that develop within the cavity [44]. These effects appear to depend on both  $L$  and  $\theta_s$  [44].

The present study aims to complement existing literature by investigating the effects of a cavity on a boundary layer that is already in transition upon encountering the cavity. Specifically, the study aims to establish the extent to which the rate of transition is modified by such an encounter and the underlying physics of this interaction. Such an understanding may then enable optimization of the streamwise location and geometry of the cavity to promote an effect on the transition process that is favourable to the application involved.

## Chapter 3

# Experimental setup and data processing

The experiments were performed in a closed-circuit wind tunnel with test-section dimensions of 508 mm height, 762 mm width, and 1900 mm length. A 19 mm-thick test surface with an elliptic leading edge of 3-to-1 axis ratio and a spanwise-oriented cavity forms the floor of the test section (Figure 3.1). Some of the wind-tunnel air entering the test section is allowed to escape under the test surface such that the flow at the test-surface leading edge is at a nominal angle of attack of zero degrees. The side walls and ceiling of the test section are streamwise-slotted. The slot dimensions were optimized as per established literature on the design of slotted-wall wind-tunnel test sections [45–48]. The use of slotted walls ensures zero streamwise pressure gradient in the test section.

The spanwise-oriented cavity on the test surface is  $D = 527$  mm deep and spans the full width of the test section. The upstream edge of the cavity is positioned 486 mm from the test-surface leading edge. Three cavity lengths of 42, 49, and 63 mm are investigated. They respectively correspond to 46.5, 54.4, and 70.0 times the momentum thickness of the undisturbed laminar boundary layer at the cavity upstream edge ( $\theta_s$ ), and to 33.8, 39.5, and 50.8 times the displacement thickness of

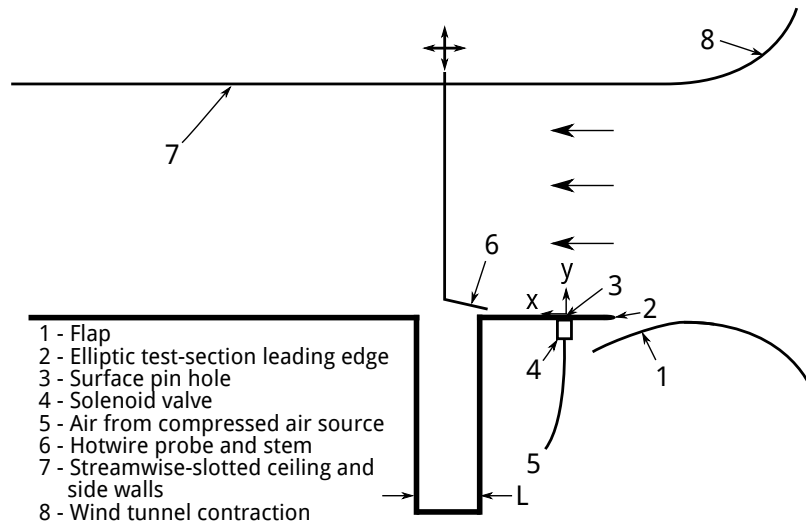


**Figure 3.1:** Cross-section schematic of the test section.

the undisturbed laminar boundary layer at the location where the turbulent spot is generated ( $\delta_0^*$ ).

A wall-normal jet of air is introduced into the test-section flow intermittently through a pinhole of 0.75 mm diameter on the test surface located 179 mm from the test-surface leading edge and offset by 15 mm from midspan. In each instance, the jet is activated for a period of 50 ms with a discharge velocity that is 7.5 times the test-section freestream velocity. A train of turbulent spots is produced by activating the jet at a frequency in the range of 1.1-1.9 Hz, which was established to be suitable for allowing the laminar boundary layer and the cavity flow to return to their undisturbed states before the arrival of the next turbulent spot.

Measurements of the flow velocity as per the matrix given in Table 3.1 was performed with a single-sensor constant-temperature hotwire probe with a tungsten sensor of 1.3 mm length and 5  $\mu\text{m}$  diameter. The sensor is oriented in the spanwise ( $z$ ) direction, which makes it sensitive to the  $x$ - and  $y$ -components of velocity. The body of the probe is inclined at an angle of 10 deg. to the test surface to best mitigate any flow blockage effects in the near-wall region [49, 50]. The anemometer signal is

**Table 3.1:** Measurement grid

Streamwise locations of measurement planes	$x = 328 \text{ mm}, 473 \text{ mm}, 530 \text{ mm}, 672 \text{ mm}^{(a)(b)}$
Wall-normal traverses per measurement plane	24 $y$ -traverses from $z = -80 \text{ mm}$ to $z = 8 \text{ mm}$ at increments of $\Delta z = 3.8 \text{ mm}^{(c)}$
Measurement points per wall-normal traverse	75 points from $y = 0.2 \text{ mm}$ to $y = 16 \text{ mm}$ clustered towards the wall
Sensor position uncertainty	$x: \pm 1.2 \text{ mm}; y: \pm 0.02 \text{ mm}; z: \pm 0.6 \text{ mm}$

<sup>(a)</sup>Additional selective measurements were performed at  $x = 400$  &  $595 \text{ mm}$  to capture the spanwise growth of the turbulent spot.

<sup>(b)</sup>Stated coordinates corresponds to a cavity length of  $L = 42 \text{ mm}$ . When the cavity length is increased,  $x$  coordinates of measurement planes located at  $x > 522 \text{ mm}$  are increased by the increase in cavity length.

<sup>(c)</sup>Additional traverses were performed at increments of  $\Delta z = 2.5 \text{ mm}$  to better capture the streaky structures in the spot.

sampled at a rate of  $10 \text{ kHz}$  and is low-pass filtered with a 9-pole filter of  $5 \text{ kHz}$  cut-off frequency, which is conservatively higher than the frequency range of the turbulence in the present flow. Sampling of the probe signal is synchronized with the time-periodic production of turbulent spots, and the data sampling duration is set to allow for the turbulent spot and its wake region to move past the probe. At each measurement position, 70 such spot-generation and measurement cycles are performed, which was confirmed to be sufficient for statistical convergence of the ensemble-averaged velocity and the root-mean-square (rms) value of its fluctuating component.

The uncertainty in the measured instantaneous velocity is conservatively estimated to be  $\pm 5\%$ , which increases to  $\pm 9\%$  for flow velocity values less than  $1.5 \text{ m/s}$ . The stated uncertainty values are primarily dictated by the analog drift in the anemometer circuitry between calibrations. Compensation of the hotwire anemometer signal for ambient temperature variations during the experiment is based on the method of Bruun [51].

The normalized perturbation velocity,  $u'$ , is calculated as:

$$u'(x, y, z, t) = \frac{u(x, y, z, t) - u_l(x, y, z)}{U_0}, \quad (3.1)$$

where  $u$  is the instantaneous measured velocity,  $u_l$ , the “laminar” velocity, is the time average of the velocity measured at the location in the absence of the turbulent spot and its wake, and  $U_0$  is the freestream velocity. The ensemble average of  $u'$  and  $u$  over  $N = 70$  measurement cycles are denoted by  $\tilde{u}'$  and  $\tilde{u}$ , respectively. During the experiments,  $U_0$  was correlated to the pressure difference of the wind-tunnel contraction leading to the test section which was sampled in conjunction with the hotwire signal.

The root-mean-square of the velocity fluctuation is calculated as:

$$u_{\text{rms}}(x, y, z) = \frac{1}{U_0} \sqrt{\frac{1}{n} \left[ \sum_n (u(x, y, z, t) - \tilde{u}(x, y, z))^2 \right]}, \quad (3.2)$$

To determine the spatial extent of the turbulent spot, the leading, trailing and spanwise edges are located at each cross-stream ( $y$ - $z$ ) measurement plane. It was found that the leading edge is most reliably identified by a specific value of the local perturbation velocity. Varying the threshold value of  $u'$  in the 2% to 5% range yields leading-edge locations that remain within 30 wall units distance of each other. This range is deemed sufficiently low to declare  $u'$  a reliable indicator of the leading edge location. The final value of the location is based on the average of the locations corresponding to five evenly-spaced threshold values of  $u'$  between 2% and 5%.

As the wake region of the spot is not free of velocity fluctuations,  $u_{\text{rms}}$  is found to be more effective than  $u'$  in locating the spot trailing edge. This finding is consistent with published literature [20, 22], and is also adopted for locating the spanwise edges of the spot in the present study. Locations corresponding to five evenly-spaced threshold

values of  $u_{\text{rms}}$  are averaged in each instance. A threshold range of 4% to 8% was deemed most effective upstream of the cavity and 10% to 15% downstream of the cavity.

Normalization of all distance measurements with the viscous length scale is performed based on the spatially-averaged wall shear stress under the footprint of the turbulent spot in absence of a surface cavity. The instant chosen for this evaluation corresponds to the most mature state of the turbulent spot in the numerical simulation, with the spot leading edge located at  $x/\delta_0^* = 400$ . Data from the numerical simulation was preferred over the experimental data for obtaining the wall shear stress under the footprint of the spot owing to the higher spatial resolution in the numerical simulation. The wall shear stress extracted from the numerical data is within 20% of the same extracted from the wall-normal profiles of time-averaged streamwise velocity using the Clauser plot technique.

## Chapter 4

# Computational models

### 4.1 Modeling in the Eulerian reference frame

The experimental investigation is complemented by a direct numerical simulation with consistent geometry and flow conditions. For computational efficiency, the generation of the turbulent spot via a wall-normal jet pulse and the downstream development of the turbulent spot are respectively captured in two separate simulations. The stream-wise development of the spot is simulated with and without the cavity on the test surface to comparatively establish the effects of the cavity on the spot structure. The simulation of the spot generation (Simulation 1), and the simulation of the streamwise spot development in the absence of the surface cavity (Simulation 2) were previously performed by Brinkerhoff and Yaras [1]. Simulation 3 involves presence of the surface cavity and was performed as part of the present study.

#### 4.1.1 Computational domain and boundary conditions

The computational domains of the three simulations are shown in Figure 4.1. Each domain consists of a flat, no-slip test surface at the bottom of the domain and free-slip surfaces at the sides and the top of the domain. A turbulent spot is generated

in Simulation 1 at mid-span with a pulsed jet from a rectangular sub-domain serving as a jet pipe positioned  $124\delta_0^*$  downstream of the leading edge of the no-slip surface, where  $\delta_0^*$  is the displacement thickness of the undisturbed boundary layer at the jet location. The domains for Simulation 2 and 3 are each larger than for Simulation 1 to allow for the growth of the spot without artificial influence from the free-slip-surface boundary conditions. The free-slip condition allows for motion only within the plane of the boundary. Avoiding any artificial influence by this constraint on the local velocity magnitude and direction requires that the boundary be placed in a region of flow where the natural flow motion is consistent with this constraint. The spanwise boundaries are placed such that they are at least  $30\delta_0^*$  away from the closest edge of the turbulent spot at its most mature state in the respective simulations. Insensitivity of the spot development to the spanwise domain width was confirmed by Brinkerhoff and Yaras [1], who observed no change in the spanwise growth rate of the turbulent spot with 50% increase in the domain width of Simulation 2. The domain height for each simulation is adjusted in the streamwise direction to follow the displacement thickness distribution of a Blasius boundary layer at the local flow Reynolds number. This ensured a constant freestream static pressure along the length of the domain.

The upstream edge of the cavity is  $274\delta_0^*$  downstream of the spot-generating jet. This distance is sufficient for the spot to develop several generations of wavepackets, thereby developing an internal structure that is representative of more mature states of turbulence [1]. The cavity has a streamwise dimension of  $L = 30\delta_0^* = 46.5\theta_s$ , and a depth of  $D = 300\delta_0^* = 465\theta_s$ . The depth of the cavity is chosen to ensure that the spot is not influenced by the bottom wall of the cavity. The cavity spans the entire domain which corresponds to more than seven cavity lengths. This span is notably larger than that required to avoid three-dimensional flow in the cavity due to end

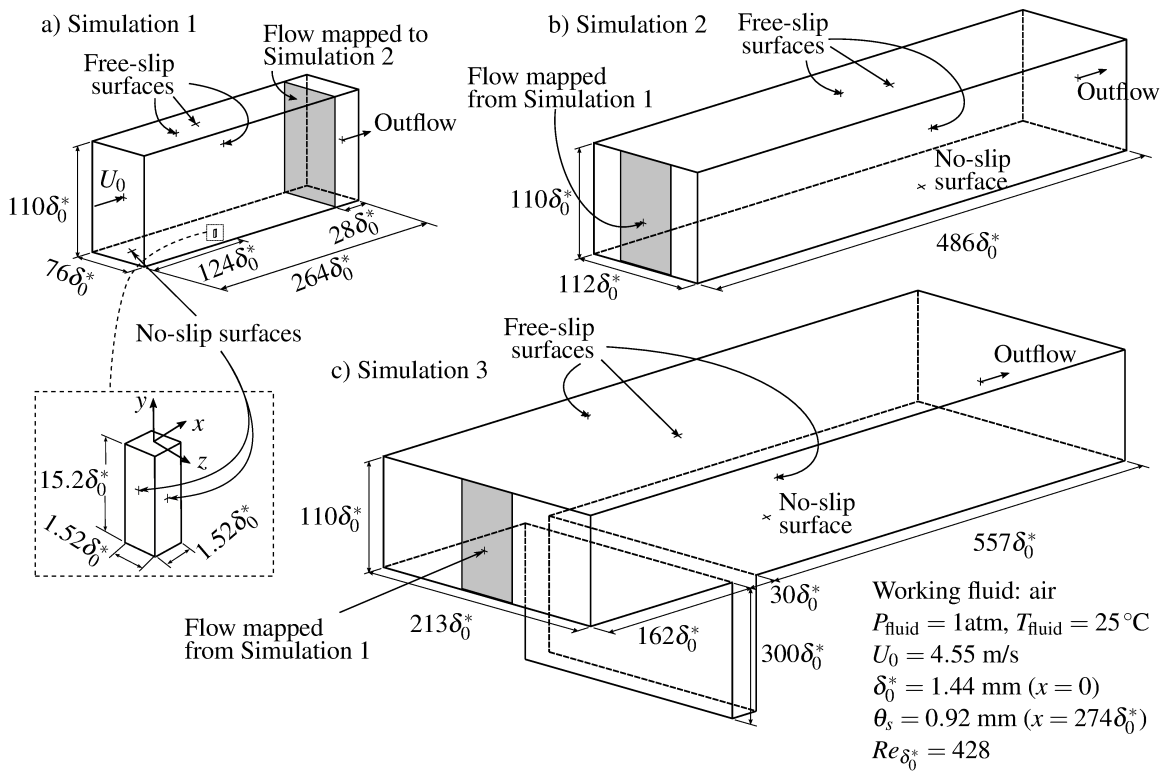


**Figure 4.1:** Schematic of the computational domains: (a) Simulation 1: turbulent spot initialization; (b) Simulation 2: turbulent spot development without a surface cavity; (c) Simulation 3: turbulent spot development with a surface cavity.

effects [52]. The chosen cavity length is sufficient to enable the wavepackets of the turbulent spot to interact with the free-shear layer of the cavity, while it is sufficiently short to avoid bypass transition affected by interaction of the cavity shear layer with the cavity downstream edge. The cavity length in the simulation corresponds to the shortest cavity length considered in the experiments. Dynamic similarity between the simulation and the experiments is realized by matching the flow Reynolds number to within 15%.

For all three simulations, the static pressure at the outflow boundary is kept fixed in an area averaged sense. The inflow data for Simulation 2 and 3 are mapped from a plane in Simulation 1 that is  $28\delta_0^*$  upstream of the domain outflow boundary (Figure 4.1). This distance to the outflow boundary was established by Brinkerhoff and Yaras [1] to be sufficient to avoid any artificial effects of standing waves that may result due to the pressure-field constraint imposed at this boundary.

#### 4.1.2 Base flow and turbulent spot initialization

Prior to introducing the spot, a laminar boundary layer is developed on the no-slip surfaces of Simulations 1, 2 and 3, including a statistically-steady cavity flow in Simulation 3. A turbulent spot is then artificially triggered by impulsively introducing a spatially uniform jet of air at the inlet of the jet pipe with a velocity  $7.7U_0$ , for a duration of  $\Delta\tau_{\text{jet}} = 27$  time units, where  $\tau = tU_0/\delta_0^*$  is a dimensionless time coordinate and  $t$  is dimensional time. The jet is activated at  $\tau = 0$  into a developed undisturbed laminar boundary layer, and Simulation 1 is continued until the laminar boundary layer fully recovers at  $\tau = 330$ . The instantaneous velocity data on the mapping plane in Simulation 1 is mapped to both Simulation 2 and 3 over a  $\Delta\tau = 200$  period ( $130 \leq \tau \leq 330$ ), during which the spot and its wake region are fully convected

through the mapping plane. The last timestep for which the wake region is observable on the mapping plane occurs at  $\tau = 319$ . The streamwise extent of the wake region is defined by the most upstream coordinate where the streamwise component of perturbation velocity is 5% of the freestream velocity. A time-independent velocity field corresponding to the local Blasius profile is imposed at the inflow of Simulation 2 and 3 for  $\tau > 330$ . Temporal integration is continued until  $\tau = 595$  and  $\tau = 905$  for Simulation 2 and 3, respectively.

### 4.1.3 Spatial grid

The spatial grids consist of hexahedral cells mapped in a structured layout. To resolve all aspects of flow turbulence, the spatial and temporal resolution must be on the order of the Kolmogorov length and time scale. The Kolmogorov length scale typically has a minimum value of  $\eta^+ \approx 2$  close to the no-slip surface in turbulent boundary layers [53, 54]. The superscript + denotes normalization by viscous length and time scales, which for the present study are computed based on spatially-averaged friction velocity,  $u_\tau = \sqrt{\tau_w/\rho}$ , under the footprint of the spot at its most mature state in absence of the cavity. The grid-node distributions are summarized in Table 4.1 and Figure 4.2. The nodes are clustered in regions where relatively high gradients in flow variables are anticipated. In regions of non-uniform node-spacing, the rate of change of node spacing is kept below 10% in all three grid directions. The smallest grid-node spacing in the  $x$ ,  $y$ , and  $z$  directions outside the jet pipe corresponds to about 4 to 10 times the Kolmogorov scale. This has been shown to be suitable for accurate direct numerical simulations of turbulent boundary layers [55–57]. The jet sub-domain is discretized with 60 nodes in each of the mutually perpendicular directions normal to the jet flow ( $x$  and  $z$ ), with uniform values of  $\Delta x^+ = 0.52$  and  $\Delta z^+ = 0.52$ . The direction parallel to the jet flow is discretized with 88 nodes distributed as shown in

**Table 4.1:** Spatial grid specifications.

	Node spacings			Node counts		
	$\Delta x^+$	$\Delta z^+$	$\Delta y_{\text{wall}}^+$	$N_x$	$N_y$	$N_z$
Simulation 1	20	8	0.7	345	82	197
Simulation 2	20	7	0.7	456	82	266
Simulation 3	See Figure 4.2(a)	8 <sup>(a)</sup>	0.7	707	82 ( $y^+ \geq 0$ ); 95 ( $y^+ < 0$ )	437

<sup>(a)</sup> Between  $-83 \leq z/\delta_0^* \leq 83$ . Otherwise increases by 10% per node up to the spanwise boundaries.

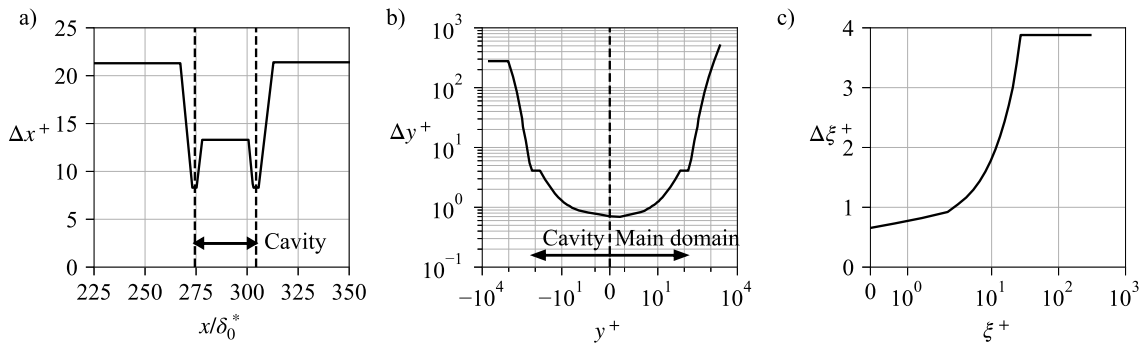


**Figure 4.2:** (a) Streamwise and (b) wall-normal node spacing for Simulation 3. (c) Node spacing in the jet pipe in the direction parallel to the jet flow, where  $\xi = 0$  is located at the jet pipe outlet.

Figure 4.2(c), where the coordinates are defined such that  $\xi = 0$  coincides with the outlet of the jet pipe and increases towards its inlet.

#### 4.1.4 Solution method

The incompressible form of the mass and momentum equations are solved with the commercial software package ANSYS CFX 16.2. Spatial discretization is based on the vertex-centered finite volume approach with values of velocity and pressure collocated at grid nodes. Interpolation of nodal values to integration points on the

control-volume surface is performed in manners equivalent to second-order central differencing for the diffusion terms, and a blend of first-order upwind and second-order central differencing schemes for the convection terms. Temporal derivatives are discretized with second order Euler backward differencing. For Simulation 1, a timestep of  $\Delta t = 7 \times 10^{-6}$  s is chosen such that the pulsed jet takes 10 timesteps to penetrate a distance of  $\delta_0^*$  into the undisturbed boundary layer. For Simulations 2 and 3, a timestep of  $\Delta t = 3.5 \times 10^{-5}$  s ( $\Delta t^+ = 0.11$ ) is chosen, where the + superscript denotes normalization by the viscous time scale,  $\nu/u_\tau$ . This is a more conservative temporal resolution than the recommended value of  $\Delta t^+ = 0.2$  to resolve the dynamics of coherent structures of boundary-layer turbulence [58].

The discretized mass and momentum equations are solved in each timestep by computing up to eight iterations that converge the coefficients of the linearized equations, with the solution of the linearized equations in each iteration realized through a W-type algebraic multigrid cycle over six grid levels. At each grid level, one and three solution sweeps are respectively performed during the restriction and prolongation passes of the cycle. For each timestep, the solution is declared as converged when the root-mean-square normalized residuals values of the governing equations are reduced to less than  $10^{-6}$ . Simulation 1 and Simulation 2 were partitioned and solved by Brinkerhoff and Yaras [1] with 20 Intel L5410 Xeon processors. Simulation 3 is partitioned and solved with 128 AMD Opteron 6272 processors.

This algorithm has been demonstrated by Valtchanov, Brinkerhoff, and Yaras [59] and earlier studies by the authors' research group to be suitable for simulating boundary layers in transitional and turbulent regimes through a benchmark direct numerical simulation of zero-pressure-gradient turbulent boundary layer (ZPGTBL). The Reynolds number of the ZPGTBL simulation is  $Re_\theta = 900$  based on the boundary layer momentum thickness, which is higher than the present simulation's  $Re_\theta = 401$ ,

calculated based on the average momentum thickness in the spot at its most mature state. As such, the ZPGTBL study realizes a broader spectrum of turbulence scales, and thus serves as a more stringent validation. The grid nodes of the ZPGTBL are spaced at  $\Delta x^+ = \Delta z^+ = 3$ . The  $y^+$  value of the first node from the no-slip boundary is 0.85 and the node spacing closely follows the distribution shown in Figure 4.2(b). The result of the validation study, shown in Figure 4.3, achieve excellent agreement with the turbulence kinetic energy budgets and streamwise velocity fluctuation profiles of Jiménez *et al.* [60] for a Reynolds number of  $Re_\theta = 1100$ . Further validation of the present numerical algorithm by the authors' research group for boundary and free-shear layer flows in both compressible and incompressible flow conditions [55–57, 61], showing good agreement in velocity fluctuation spectra, turbulence-kinetic-energy production rate budgets, and mean velocity profiles, complement the results observed in the validation study of Valtchanov, Brinkerhoff, and Yaras [59]. The same algorithm was used by Brinkerhoff and Yaras [1] for the study of turbulent spots. In that study, it was demonstrated that, owing to the relatively large coherent structures prevailing in a turbulent spot, these structures can be suitably resolved with somewhat coarser spatial grids based on  $\Delta x^+ = 22$ ,  $\Delta z^+ = 11$ , and  $\Delta y_{\text{wall}}^+ = 0.85$ . The grid resolution of the present study is based on these findings.

## 4.2 Inviscid modeling in the Lagrangian reference frame

Hairpin vortices of turbulence induce velocity on themselves and other hairpin vortices in their vicinity primarily through inviscid mechanisms. To help shed light on the flow physics, the computational approach described in Section 4.1 is complemented by a

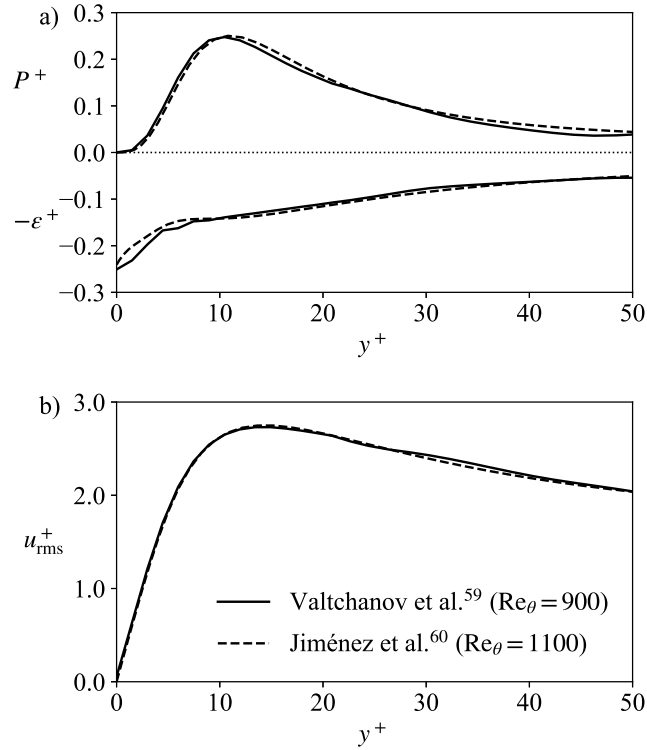


**Figure 4.3:** Comparison of the direct numerical simulations of Valtchanov, Brinkerhoff, and Yaras [59] and Jiménez *et al.* [60]: (a) rates of turbulence-kinetic-energy production,  $P^+ = -\overline{u_i u_j}^+ \partial \bar{U}^+ / \partial x_j^+$ , and dissipation,  $\epsilon^+ = \overline{\frac{\partial u_i}{\partial x_j} \frac{\partial u_i}{\partial x_j}}^+$  and (b) profiles of streamwise velocity fluctuation.

localized Lagrangian vortex-filament-based inviscid model. This model is initialized with a single Kelvin-Helmholtz roller in the form of a vortex filament embedded in an idealized background two-dimensional streamwise velocity distribution based on the time-averaged velocity over the cavity obtained from the Eulerian model described in Section 4.1. This velocity distribution is then perturbed with a spanwise-periodic sinusoidal perturbation in the  $x$  and  $y$  components of velocity ( $u'$  and  $v'$ ) with an amplitude of about 10% of freestream velocity and a wavelength of about 100 viscous

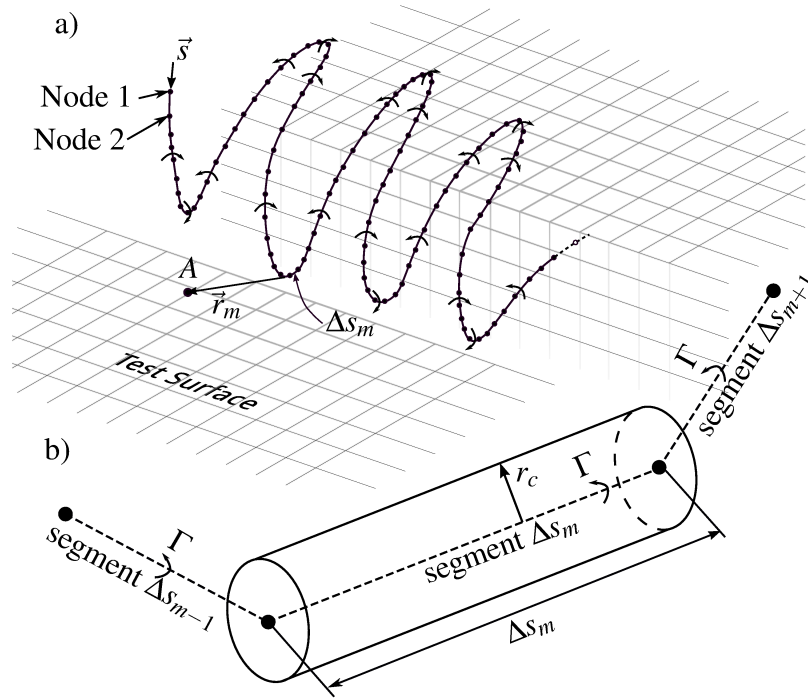


**Figure 4.4:** Schematic of the vortex-filament computational model: (a) vortex filament observed at a mature stage of development; (b) a magnified view of segment  $\Delta s_m$  identified in (a).

wall units ( $4.5\delta_0^*$ ). This computational model is summarized in Figure 4.4. The velocity at a point of interest,  $A$ , is the vector sum of the background velocity,  $\vec{V}_{\text{background}}$ , and the velocity induced by the vortex filament as described by the Biot-Savart law:

$$\vec{V} = \vec{V}_{\text{background}} + \frac{\Gamma}{4\pi} \int_{-\infty}^{\infty} \frac{\vec{r}_m \times d\vec{s}_m}{|\vec{r}_m|^3} \quad (4.1)$$

$$\vec{V} \approx \vec{V}_{\text{background}} + \frac{\Gamma}{4\pi} \sum_m \frac{\vec{r}_m \times \Delta\vec{s}_m}{|\vec{r}_m|^3}, \quad (4.2)$$

where  $\Gamma$  denotes the circulation of the vortex filament set to a value of  $\delta_0^*U_0$  based on the roller circulation observed in the Eulerian model in the absence of the turbulent spot. The remaining terminology is summarized in Figure 4.4.

The modeled vortex filament is  $40\delta_0^*$  long. This is close to ten times the spanwise wavelength of the dominant instability mode expected in turbulent spots [62] ( $\Delta z = 100^+ = 4.5\delta_0^*$ ). Discretization of the vortex filament into 200 segments, each with an initial length of  $0.2\delta_0^*$ , produces results that are insensitive to the segment length. During the evolution of the vortex filament, the segments are subdivided whenever they exceed a length of  $0.75\delta_0^*$  due to stretching, thus ensuring consistency of spatial resolution over the simulated development time. A time-independent finite radius of  $r_c = 0.6\delta_0^*$  is assigned to each segment to prevent numerical instability, where the segment is not able to induce a velocity on itself within the core volume defined by this radius. The inviscid nature of this Lagrangian model is justified on the basis of the Kelvin-Helmholtz roller taking less than 15% of the viscous diffusion time scale,  $r_c^2/\nu$ , to convect across the length of the cavity. The vortex filament is developed in time using the same timestep size of the direct numerical simulation described in Section 4.1. The vortex filament takes 200 timesteps to convect from its initial position set at the cavity surface halfway along the length of the cavity to the downstream edge of the cavity.

## Chapter 5

# Freestream operating conditions, boundary-layer development and cavity flow development without a turbulent spot

In the experiment, the location of the cavity upstream edge corresponds to a Reynolds number of  $195,000 \pm 5000$  based on the freestream velocity and the distance from the test-surface leading edge. The freestream velocity of  $U_0 = 6$  m/s and turbulence intensity of 0.4% is uniform throughout the length of the test section. Upstream of the cavity, the undisturbed Blasius boundary layer with a shape factor that remains in the 2.4 to 2.8 range grows to a displacement thickness of 1.24 mm at the streamwise location of the spot-generating jet ( $\delta_0^*$ ) and a momentum thickness of 0.9 mm at the upstream edge of the cavity ( $\theta_s$ ).  $\delta_0^*$  and  $\theta_s$  are used as reference length scales in the remainder of the paper. Downstream of the shortest cavity considered ( $L/\theta_s = 46.5$ ), the boundary layer remains laminar at least up to the most downstream measurement location, which is positioned at 1000 mm ( $806\delta_0^*$ ) from the test-surface leading edge. Immediately downstream of the cavity, the time-averaged velocity profile of the boundary layer is relatively less full corresponding to a shape factor of 1.9, which

gradually returns to a value of 2.6 at 3.5 cavity lengths ( $120\delta_0^*$ ) from the cavity. Two-dimensionality of the cavity flow for all three cavity lengths was confirmed through measurements of the laminar cavity velocity field at several spanwise locations.

Consistent with the experimental observations, the boundary layer in the simulations remains laminar with a shape factor of 2.5 up to the cavity, with a displacement thickness that agrees with the corresponding Blasius value to within 4%. The simulation flow Reynolds number based on the streamwise location of the cavity and the freestream velocity is 170,600, and the freestream turbulence intensity is 0.2%. The low level of freestream turbulence is the result of temporal velocity fluctuations caused by round-off errors in the computation, and was not set explicitly. The time-averaged states of the cavity shear layer and the boundary layer downstream of the cavity are computed from seven full vorticity shedding cycles once the computed flow attains a statistically steady state. The cycle-to-cycle variation in streamwise peak velocity oscillation amplitude was noted to remain within 6%. Comparable with the experimental observations, the shape factor of the boundary layer varies from 2.1 immediately downstream of the cavity to 2.5 at three cavity lengths downstream. The reduction in the shape factor value to 2.1 is accompanied by a 12% reduction in the boundary layer displacement thickness with reference to the corresponding Blasius value. At the downstream location where the shape factor returns to the Blasius value of 2.5, the displacement thickness is only 3% below the corresponding Blasius value. These observations indicate that the boundary layer is able to fully recover from its encounter with the cavity in this particular configuration.

In the simulation with  $L/\theta_s = 46.5$  cavity length, feedback-driven oscillations of  $0.2U_0$  magnitude are observed in the streamwise velocity of the shear layer over and downstream of the cavity at a frequency of  $St_{\theta_s} = 0.015$  consistent with published literature (Figure 2.2). The length of the cavity corresponding to  $L/\theta_s = 46.5$  is

very close to the threshold separating the oscillating and non-oscillating flow regimes [27, 32]. This threshold has been shown to be sensitive to Reynolds number and cavity depth [33–35], resulting in some uncertainty regarding the existence of oscillations in close proximity of the threshold. Absence of flow oscillations at the  $L/\theta_s = 46.5$  value in the present experiments may be due to this variability. To nonetheless allow for a complementary analysis of the computed and experimental results, two additional cavity lengths corresponding to  $L/\theta_s = 54.4$  and  $L/\theta_s = 70.0$  were included in the experimental study. Both of these cavity configurations produce the expected feedback-driven oscillatory flow field, with Strouhal-number values of  $St_{\theta_s} = 0.0095$  and  $0.0084$ , respectively. This trend in oscillation frequency with cavity length is consistent with literature (Figure 2.2). The amplitude of velocity oscillation increases from  $0.05U_0$  to  $0.15U_0$  as  $L/\theta_s$  is increased from 54.4 to 70.0, which is also in agreement with past studies [43, 63].

The boundary layer downstream of the cavity remains laminar for  $L/\theta_s = 46.5$  in both the simulation and the experiments, but transitions to turbulence in the experiments with  $L/\theta_s = 54.4$  and  $70.0$ . The transition to turbulence in these two cases is observed to be completed by 6 cavity lengths from the downstream edge of the cavity. This location is determined based on the turbulence intermittency in the boundary layer reaching a value of 100%, with the intermittency quantified from time traces of the local velocity using the method of Volino, Schultz, and Pratt [64].

The time-averaged velocity field at the streamwise midpoint of the cavity is plotted in Figure 5.1. The agreement between experimental and computational results is noted to be favourable. The time-averaged shear layer over the cavity is further characterized through streamwise variation of vorticity thickness determined with this velocity field as plotted in Figure 5.2. This thickness is defined as:

$$\delta_{\omega z} = U_0 / (d\bar{u}/dy)_{\max} \quad (5.1)$$

In the figure,  $\delta_{\omega z}$  is normalized by the same at the cavity upstream edge. Vorticity thickness is preferred for this characterization over alternative shear layer thicknesses, such as displacement and momentum thicknesses, as the latter thicknesses are found to be less informative on the flow physics in the presence of recirculation within the cavity. The streamwise variation of  $\delta_{\omega z}$  in the present study is noted to compare favourably with that of Sarohia [27]. This is not surprising given the similar values of  $L/D$  and  $L/\theta_s$  for the present study and the study of Sarohia [27]. The agreement with the data of Basley *et al.* [37] is also reasonable. However, the data of Chang, Constantinescu, and Park [39] suggests a notably higher rate of shear layer growth, particularly over the second half of the cavity length. This may be explained by the formation of hairpin vortices at  $x/L = 0.5$  that the authors attribute to three-dimensional instability originating in their cavity. This is not observed in the present study, likely due to the larger cavity depth.

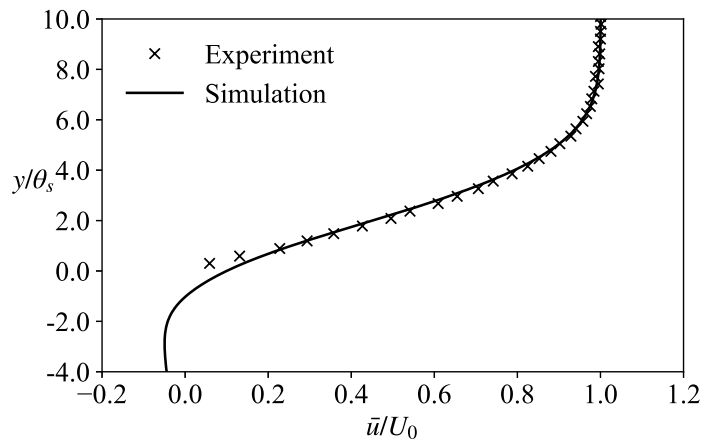


**Figure 5.1:** Wall-normal profile of time-averaged streamwise velocity at the streamwise midpoint location in the cavity ( $L/\theta_s = 46.5$ ).

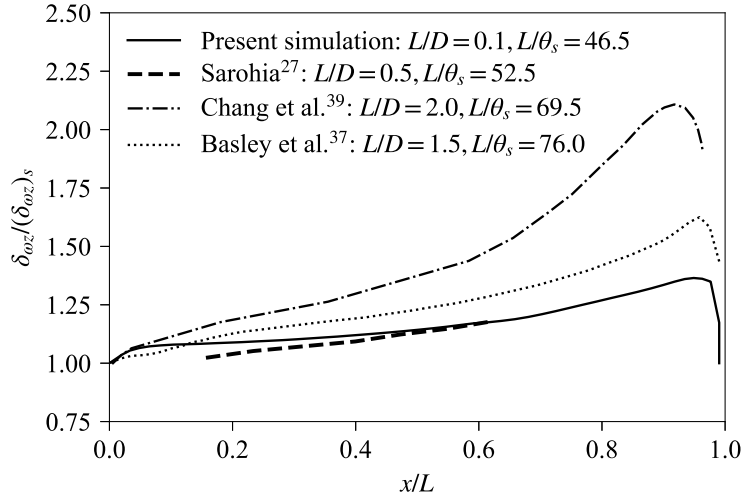


**Figure 5.2:** Streamwise development of vorticity thickness over the cavity.

Figure 5.3 shows the instantaneous distribution of the spanwise component of perturbation vorticity on the midspan plane at a statistically steady state in the simulation. The perturbation vorticity vector,  $\vec{\omega}'$ , is defined as the curl of the perturbation velocity vector,  $\vec{u}'$ .  $\vec{u}'$  is determined by subtracting the instantaneous velocity,  $\vec{u}$ , from the time-averaged velocity,  $\vec{u}$ . Kelvin-Helmholtz rollers are observed to develop within the cavity shear layer and are identified with the black-coloured contour lines of  $\omega'_z \delta_0^*/U_0 = -0.0158$ . The rollers induce downwash on their downstream side and upwash on their upstream side, creating time-periodic positive and negative perturbation in the local velocity field. The rollers are further characterized by their circulation,  $\Gamma'$ . In each instance, this circulation is determined by summing up  $\omega'_z$  over the area enclosed by the  $\omega_z \delta_0^*/U_0 = -0.0158$  contour. The circulation values noted in the figure are obtained by averaging the values over six shedding cycles. The rollers reach their peak circulation immediately prior to the impingement on the cavity downstream edge. During the impingement, a smaller portion of each roller is swept into the cavity while the majority is convected downstream. Downstream of the cavity, the interaction of the rollers with the wall results in the generation of

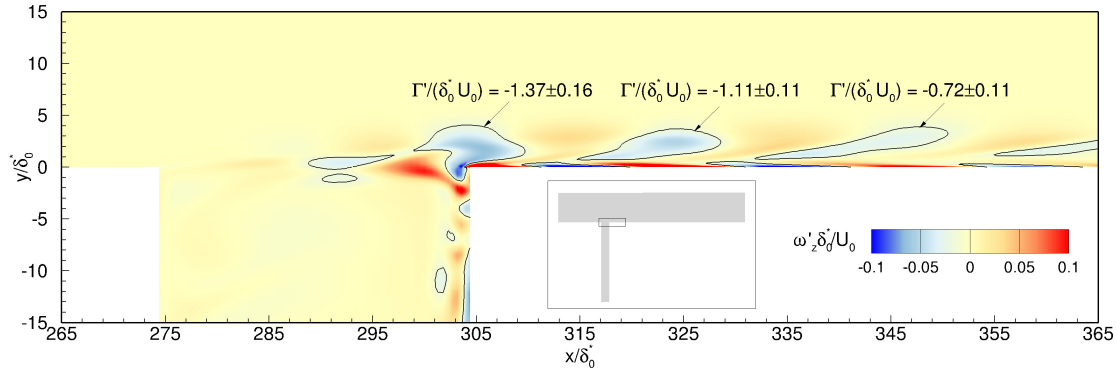


**Figure 5.3:** Instantaneous spatial distribution of  $\omega'_z \delta_0^*/U_0$  at  $z = 0$ . Negative vorticity in this view corresponds to a clockwise sense of rotation.

perturbation vorticity of the opposite sign beneath each roller, causing the rollers to weaken with streamwise distance. The simulation domain is not long enough for the vorticity to be completely eliminated as the counter rotating vorticity beneath the rollers also weakens with streamwise distance. This computational result is in agreement with the experimental results, where velocity oscillations remain detectable 15 cavity lengths downstream of the cavity, which is near the outlet of the test section. In close vicinity of the cavity downstream edge, the rollers have an average streamwise spacing and convection speed of  $23\theta_s \pm 1\theta_s$  and  $0.36U_0 \pm 0.01U_0$ , respectively. The convection speed agrees well with the speed of  $0.4U_0$  reported by Chang, Constantinescu, and Park [39]. The noted streamwise spacing and convection velocity corresponds to a Strouhal number value of  $St_{\theta_s} = 0.015$ . This value is consistent with the Strouhal number calculated from the measured time trace of velocity in the cavity shear layer,  $0.1L$  upstream of the downstream edge of the cavity.

## Chapter 6

# Results and discussion

### 6.1 Development of the turbulent spot upstream of the cavity

The turbulent spot measured in the experiment at distances of  $175\theta_s$  ( $x/\delta_0^* = 121.0$ ) and  $8\theta_s$  ( $x/\delta_0^* = 241.9$ ) upstream of the  $46.5\theta_s$ -long cavity is visualized through the ensemble-averaged perturbation velocity distribution in Figure 6.1. As noted previously,  $\delta_0^*$  denotes the boundary-layer displacement thickness at the jet coordinate. The  $y$ - $\tau$  plane shows the turbulent spot centerline while the  $y$ - $z$  and  $z$ - $\tau$  planes are located such that the dominant features of the turbulent spot are most clearly visualized. The  $y$ - $\tau$  plane shows a turbulent spot of conventional shape, with a height that is about twice the local boundary-layer thickness. A larger region of negative perturbation velocity resides over a smaller region of positive perturbation velocity. An overhang region is observed downstream of the turbulent spot while a wake with a positive perturbation velocity that has a stabilizing (calming) effect is observed on its upstream side. These observations are consistent with experimental and numerical studies on turbulent spots subject to zero streamwise pressure gradient [1, 20]. In the  $z$ - $\tau$  plane,

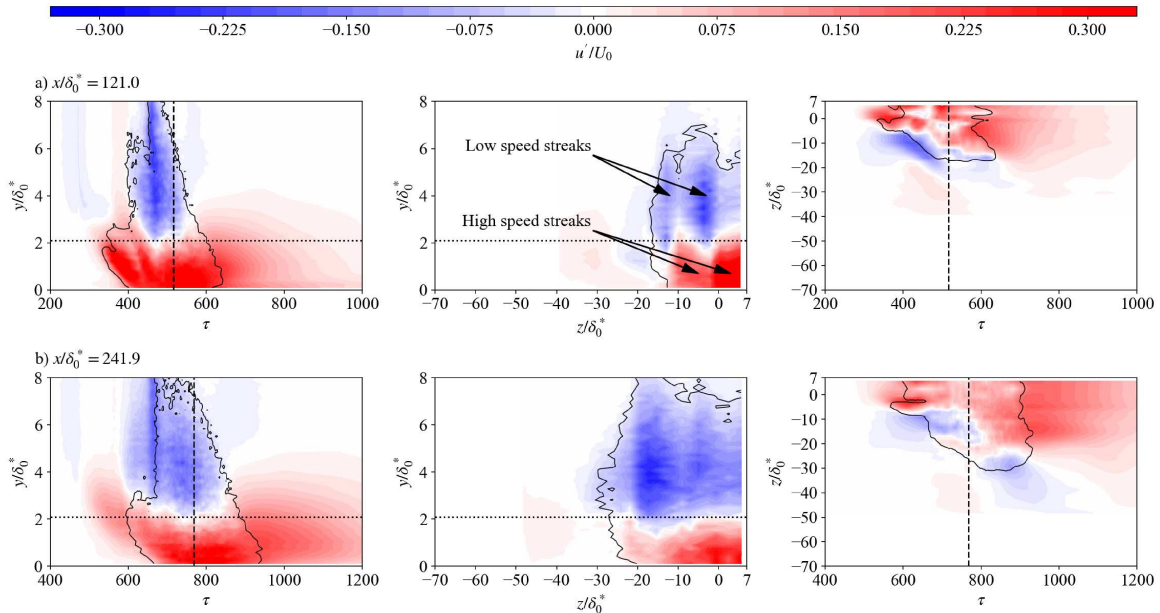


**Figure 6.1:** Perturbation velocity in the  $y$ - $\tau$ ,  $y$ - $z$ , and  $z$ - $\tau$  planes at the experimental measurement planes (a)  $x/\delta_0^* = 121.0$  and (b)  $x/\delta_0^* = 241.9$ . The  $y$ - $\tau$  plane is located at the spot centerline. Dashed line shows the location of the  $y$ - $z$  plane. Dotted line shows the location of the  $z$ - $\tau$  plane. Black solid lines approximate the perimeter of the spot with  $u_{\text{rms}}/U_0 = 0.06$ . Plots are not to scale.

the turbulent spot follows a conventional shape approximating a downstream-pointing arrowhead. High- and low-speed streaks are visible in both the  $z$ - $\tau$  and  $y$ - $z$  planes. The spanwise streak spacing is determined to be  $\lambda_z^+ \approx 160$ . This value is comparable to those reported in published literature [4, 10]. The spanwise-smearing appearance of the streaks when observed through ensemble-averaged quantities is likely due to spanwise meandering of the streaks, a phenomenon commonly observed unless diminished by high streamwise acceleration driven by strong favourable streamwise pressure gradients [20, 49]. The perturbation velocity magnitude for the high-speed streaks near the wall reaches 30% of the freestream velocity. This is just above the threshold of 26% suggested to be necessary for the sinuous streak instability to be significant in a zero-pressure-gradient boundary layer [11]. This may further contribute to the spanwise smearing of the streaks.

The edges of the spot are located using the method outlined in Chapter 3. Using data obtained at streamwise locations of  $x/\delta_0^* = 121.0, 181.5$  and  $241.9$ , the lateral growth of the spot as it convects in the streamwise direction is determined to correspond to a spreading angle of  $7.3$  deg. This is consistent with values quoted in the literature for zero-pressure-gradient boundary layers [6, 16]. The leading and trailing edge celerities are calculated to be  $0.6U_0$  and  $0.3U_0$  respectively, which are lower than the often-cited values of  $0.9U_0$  and  $0.55U_0$  [17, 20]. This difference may be explained by the lower wall-normal coordinates at which the leading and trailing edges of the relatively young spot are situated. The rate of streamwise growth of the turbulent spot, as dictated by the difference between the leading- and trailing-edge celerities, remains consistent with literature.

Large-scale turbulent-spot features such as streak spacing, streak perturbation velocity magnitude, and spot longitudinal and lateral spreading rates are consistent between the experiment and the simulations. Further details on the internal structure of the spot are more readily gleaned from the simulations. In the absence of cavity effects (Simulation 1 and 2), these details were described comprehensively by Brinkerhoff and Yaras [1]. To serve as a reference for the structure of the spot past the cavity, a summary of the observations of Brinkerhoff and Yaras [1] is presented here, with an emphasis on flow structures that will be shown to play an important role in the spot/cavity flow interaction.

Figure 6.2 shows the turbulent spot as it develops from a young spot with only two generations of hairpin vortices (Figure 6.2a) until it reaches  $30\delta_0^*$  upstream of the cavity upstream edge (Figure 6.2b). The spot is visualized with isosurfaces of the second invariant of the velocity gradient tensor, denoted  $Q$ , normalized by  $(U_0/\delta_0^*)^2$ .  $Q$  is defined as:

$$Q = \frac{1}{2} \left( \frac{\partial u_i}{\partial x_i} \frac{\partial u_j}{\partial x_j} - \frac{\partial u_i}{\partial x_j} \frac{\partial u_j}{\partial x_i} \right), \quad (6.1)$$

where Einstein summation is implied over the indexed terms. The illustrated isosurface value is  $Q/(U/\delta_0^*)^2 = 2 \times 10^{-4}$ , which allows the dominant vortical structures to be visible most clearly. Upon introduction of a wall-normal jet pulse into the laminar boundary layer at  $\tau = 0$ , a pair of counter rotating, streamwise-oriented vortices (labeled A) form downstream of the jet. The induced velocity field of the A vortices reorients the local background spanwise vorticity to develop a wall-normal component. The reoriented vorticity is then stretched by the background shear in the  $x$ - $y$  plane and forms the initial wavepackets (labeled B and C) that straddle the A vortices. By  $\tau = 118$ , the turbulent spot contains about two generations of wavepackets, with the more mature generation (B and C) evolving into the familiar hairpin shape. By  $\tau = 301$ , the turbulent spot contains several generations of wavepackets, most of which are situated at a wall-normal position comparable to the centerline position of the Kelvin-Helmholtz rollers over the cavity. A few of the larger vortical structures in the leading edge region of the spot, such as C, are located at  $y/\delta_0^* \approx 10$ , which is about twice the wall-normal distance of the rollers' uppermost portions over and downstream of the cavity (Figure 5.3). At this moment, the turbulent spot has developed a pattern of growth that will be present for its entire lifetime if it is allowed to convect over the surface without any geometric or other external perturbations: (1) older vortical structures, such as C, D, and G, are enlarged and concentrated near the leading edge of the spot; (2) hairpin vortices of a range of spatial scales occupy the interior of the spot, where turbulence is sustained by the perpetual generation of new smaller hairpin vortices in streamwise-aligned groups (wavepackets) via the induced and destabilizing effects of the existing larger hairpin vortices; and (3) the laminar

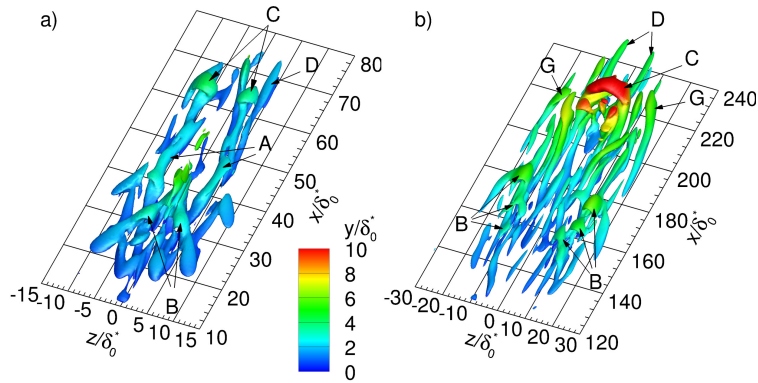


**Figure 6.2:** The turbulent spot upstream of the cavity visualized through isosurfaces of  $Q/(U/\delta_0^*)^2 = 2 \times 10^{-4}$  at (a)  $\tau = 118$  and (b)  $\tau = 301$ .

flow along the side edges of the spot is similarly destabilized to produce wavepackets in this previously undisturbed region, thus promoting lateral spot growth [1]. Mutual interactions of the hairpin vortices within a mature spot can cause the shape of the vortices to deviate significantly from the idealized hairpin shape. For example, much of the streamwise-oriented structures noted in Figure 6.2b, such as structure G, evolved originally from hairpin vortices.

The leading edge of the spot arrives at the cavity upstream edge at approximately  $\tau = 330$ . Thus, the spot structure shown in Figure 6.2b at  $\tau = 301$  closely represents the spot at the start of the interaction with the cavity.

## 6.2 Development of the turbulent spot over and downstream of the cavity

The first measurement plane downstream of the cavity is at  $4\delta_0^*$  distance from the downstream edge of the cavity. The turbulent spot measured at this location ( $x/\delta_0^* = 287.3$ ) is illustrated in Figure 6.3a. In contrast to the spot structure upstream of the

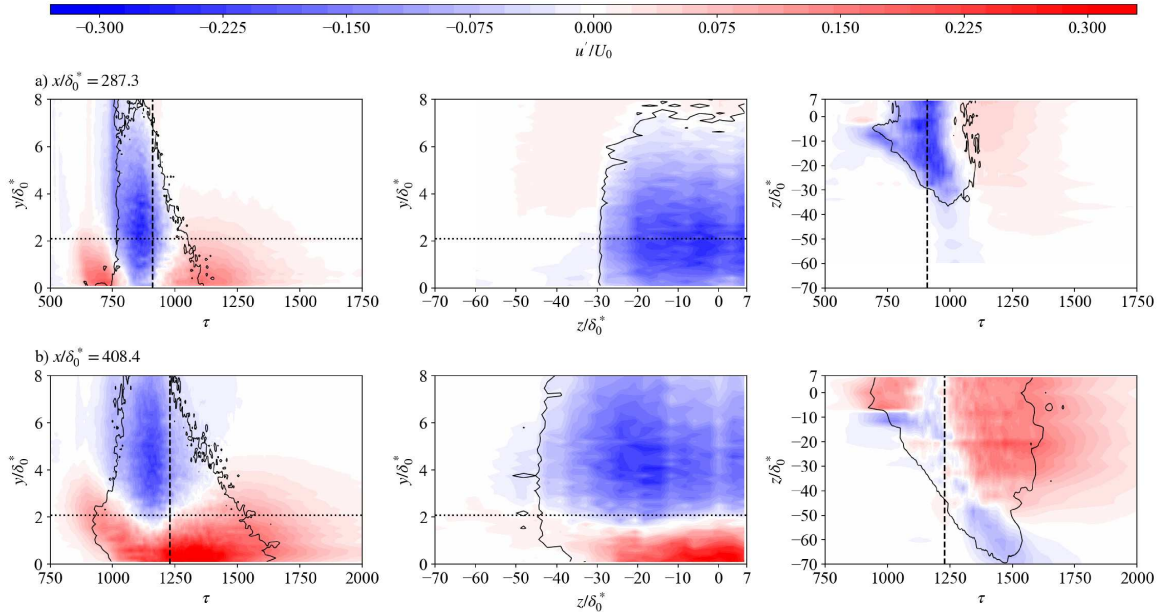


**Figure 6.3:** Perturbation velocity in the  $y$ - $\tau$ ,  $y$ - $z$ , and  $z$ - $\tau$  planes at the experimental measurement planes (a)  $x/\delta_0^* = 287.3$  and (b)  $x/\delta_0^* = 408.4$ . The  $y$ - $\tau$  plane is located at the spot centerline. Dashed line shows the location of the  $y$ - $z$  plane. Dotted line shows the location of the  $z$ - $\tau$  plane. Black solid lines approximate the perimeter of the spot with  $u_{\text{rms}}/U_0 = 0.06$ . Plots are not to scale.

cavity illustrated in Figure 6.1b, the high-speed streaks positioned in close vicinity of the wall are notably weaker, disappearing completely in the middle portion of the spot's length. Measurements over the cavity, at  $22\delta_0^*$  (65% of cavity length) from the cavity upstream edge, indicate that velocity fluctuations due to the spot turbulence extend into the cavity by about 2 to  $2.5\delta_0^*$ . This suggests the spot to slightly descend into the cavity as it travels over the cavity. This is consistent with the expected mutually-induced downward motion of the streamwise legs of the hairpin vortices in the absence of a solid boundary that would prevent such a motion. As a result of this downward motion, the high-speed streaks created by the induced motions of the hairpin vortices appear to impinge on the downstream wall of the cavity, and get at least partially swept into the cavity instead of convecting over the cavity downstream edge. By  $126.6\delta_0^*$  distance from the cavity downstream edge ( $x/\delta_0^* = 408.4$ ), shown in

Figure 6.3b, the high-speed streaks are observed to regain their strength. However, both low- and high-speed streaks appear merged with their neighbouring streaks compared to the observation upstream of the cavity. This suggests a less organized distribution of the streaks and/or increased meandering, and is consistent with past experimental and numerical studies of turbulent boundary layers downstream of a cavity [39, 42].

The streamwise variation of the spot half-width is plotted in Figure 6.4. Upstream of the cavity, the half-spot spreading angle of 7.3 deg. is constant over at least  $120\delta_0^*$  streamwise distance, indicating that the mechanisms driving the spanwise growth of the spot in this region are well-established and independent of the disturbance that created the spot. The spreading angle downstream of the cavity is 16.1 deg., which is notably higher than the value of 7.3 deg. measured upstream of the cavity. This indicates a significant increase in the lateral growth rate of the spot upon encountering the cavity. The relatively minor amount of deviation from a linear trend downstream of the cavity suggests that the physical mechanisms resulting in the increased lateral growth rate are established upstream of the cavity downstream edge and remain intact for at least  $100\delta_0^*$  distance downstream. The mechanisms driving lateral growth will be discussed further in Section 6.6. Encountering the cavity also affects the streamwise growth rate of the spot, which will be discussed in Section 6.7.

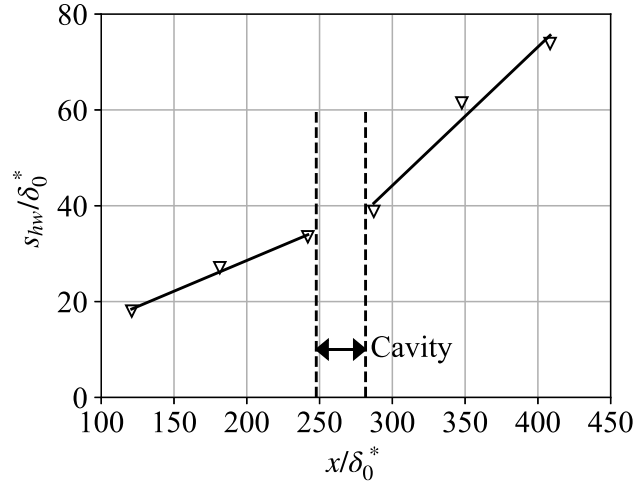


**Figure 6.4:** Variation of spot half-width,  $s_{hw}$ , with streamwise location of the spot.

### 6.3 Development of the leading-edge region of the spot downstream of the cavity

Prior to the arrival of the turbulent spot, Kelvin-Helmholtz (K-H) rollers over and downstream of the cavity are coherent and spanwise uniform. The leading-edge region of the spot convects faster than the rollers, allowing it to overtake and interact with multiple rollers. Since most vortical structures within the leading-edge region of the spot are larger-scale structures located high above the rollers, changes to these vortical structures and the K-H rollers are not observed until they reach a location that is one to two cavity lengths downstream of the cavity. By  $\tau = 451$ , the spot leading edge has overtaken two K-H rollers and has traversed two cavity lengths on the downstream surface. The spot at this instant in time is illustrated via isosurfaces of  $Q$  in Figure 6.5b. For reference, the spot at the same instant in time in the absence of the cavity is shown in Figure 6.5a. Vortical structure C, which is higher up than the other structures as per the colour scale is essentially the same

in Figure 6.5a and Figure 6.5b, suggesting that it has avoided any interaction with the rollers. Streamwise-elongated vortical structure labeled G extends by  $60\delta_0^*$  in the streamwise direction in absence of the cavity (Figure 6.5a). In the presence of the cavity (Figure 6.5b), this structure has been tilted in the direction of the rollers' induced velocity. The part of the G structure immediately downstream of roller 2 is convected towards the wall to a wall-normal coordinate that is half of where this structure resides at in the absence of the cavity. Although such tilting of streamwise-aligned vortices is observed throughout the leading edge region of the spot, its impact on the composition of the spot is relatively limited as the tilted structures appear to evolve in a similar manner to the corresponding structures in absence of the cavity. A notably larger effect of the cavity on the spot structure is observed near the coordinates of roller 2 ( $310 \leq x/\delta_0^* \leq 330$ ) where a spanwise-row of hairpin vortices not observed in absence of the cavity, labeled H, is observed in place of roller 2. The mechanism of their formation is demonstrated by correlating their positions with the positions of high-speed streaks, shown in Figure 6.6. In this figure, streamwise perturbation velocity is shown on a surface at  $y/\delta_0^* = 3.75$ , which intersects with the centerline of roller 2. High-speed streaks labeled J are present within the spot both with and without the cavity and have a spanwise spacing of approximately  $\lambda_z = 12\delta_0^*$ . The locations of the H vortices coincide with the locations of these streaks. Examination of a time series of  $Q$  isosurfaces and perturbation velocity contours shows the following sequence of events: (1) as the high-speed streak overtakes roller 2, the initially-spanwise vorticity of roller 2 reorients into the streamwise direction in accordance with the spanwise wavelength of the streaks; and (2) self-induced lift-up and the subsequent stretching into the streamwise direction causes the H vortices to form. The same process is observed for all rollers that are initially spanwise coherent and uniform that are subsequently overtaken by the spot. These hairpin vortices thus

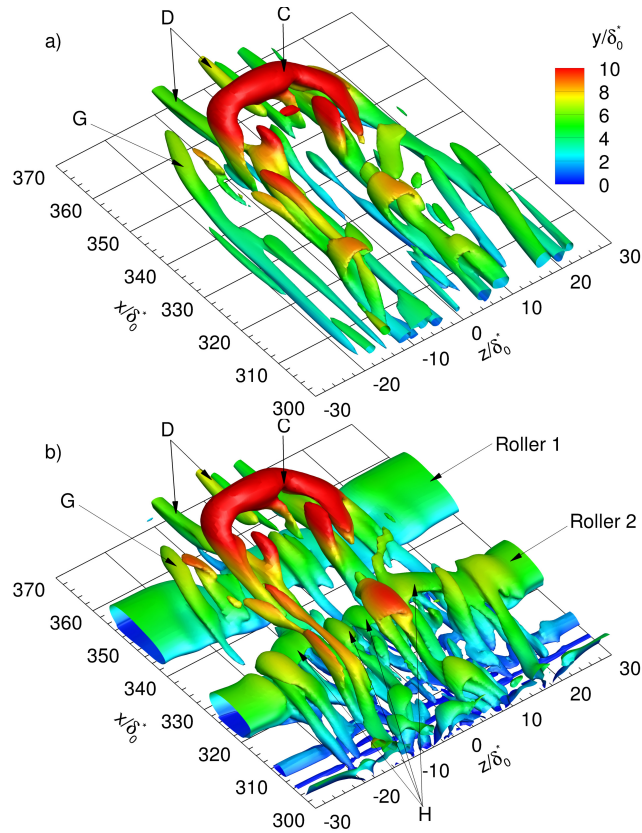


**Figure 6.5:** The turbulent spot visualized through isosurfaces of  $Q/(U/\delta_0^*)^2 = 2 \times 10^{-4}$  at  $\tau = 451$  (a) in the absence, and (b) in the presence of the cavity.

have a streamwise spacing identical to that of the K-H wavelength and a spanwise spacing matching the prevailing streak spacing of the spot.

## 6.4 Development of spot turbulence over and downstream of the cavity

By  $\tau = 484$ , about half of the streamwise length of the turbulent spot has convected past the cavity. Figure 6.7a illustrates this moment from a top-down view with  $Q$

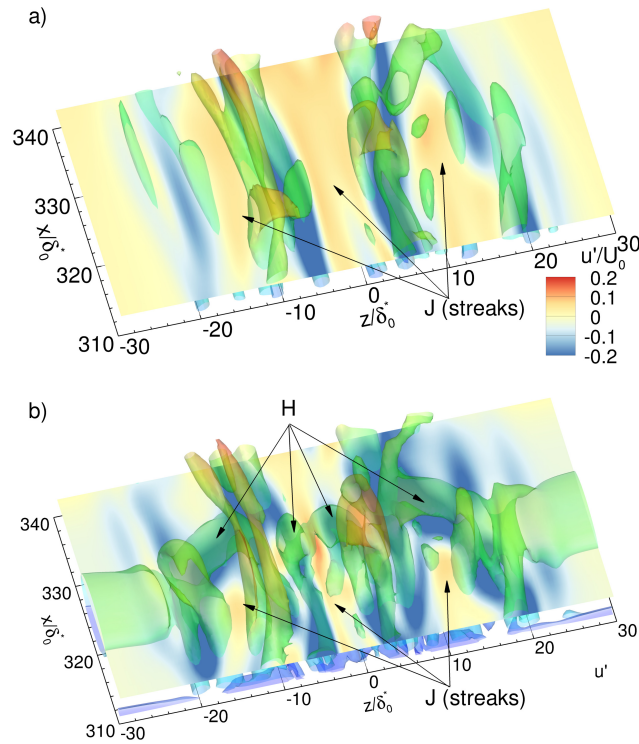


**Figure 6.6:** Magnified view of the H vortices shown in Figure 6.5 overlaid with colour contours of perturbation streamwise velocity on a surface at  $y/\delta_0^* = 3.75$  (a) in the absence, and (b) in the presence of the cavity.

isosurfaces. For reference, Figure 6.7b shows the spot at the same instant in time in absence of the cavity. Qualitatively, larger-scale turbulent-spot structures located relatively far from the no-slip surface appear unaltered by the encounter with the cavity (Figure 6.7a vs Figure 6.7b). Downstream of the cavity downstream edge and close to the surface, the number of vortical structures appears to be notably larger in the presence of the cavity. When viewed from the bottom (Figure 6.7c), most of these structures are oriented to be within 15 deg. of the streamwise direction, and in a few instances appear to form an upstream-pointing,  $\Lambda$ -like shape. The formation of these structures can be traced back to the inverted hairpin vortices that formed directly over the cavity. Inverted hairpin vortices have heads that are located upstream and

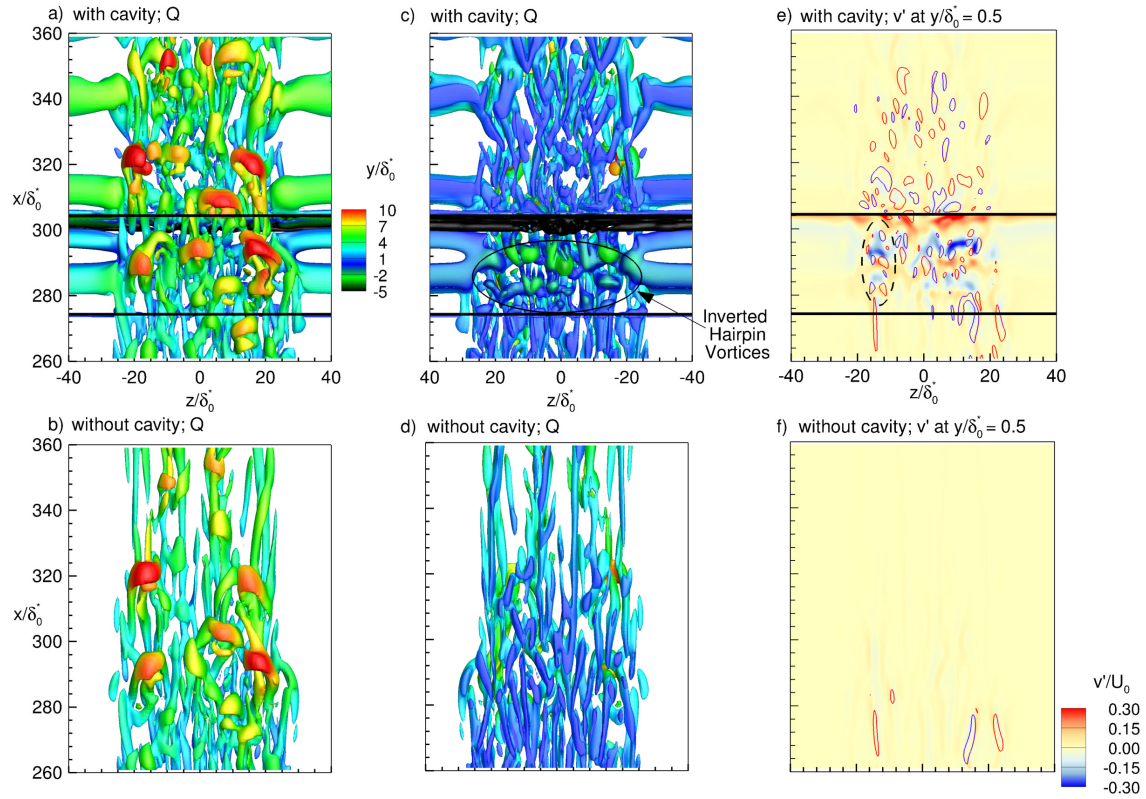


**Figure 6.7:** Turbulent spot viewed at  $\tau = 484$  with black-colour lines locating the cavity edges. (a,b): top view of isosurfaces of  $Q/(U/\delta_0^*)^2 = 2 \times 10^{-4}$ ; (c,d): bottom view of isosurfaces of  $Q/(U/\delta_0^*)^2 = 2 \times 10^{-4}$ ; (e,f): flood plot of the wall-normal component of perturbation velocity with contours of  $x$  component of perturbation vorticity,  $|\omega'_x|\delta_0^*/U_0$ , corresponding to a value of  $+0.25$  (red colour) and  $-0.25$  (blue colour).

below their streamwise-oriented legs, and are typically suppressed in boundary layer turbulence due to the friction exerted by the wall [65, 66]. Their presence over the cavity (Figure 6.7c) is not surprising as the no-slip condition of the wall is absent there. The origin of these inverted hairpin vortices is explored in more detail in Section 6.5. Their heads extend around  $2.5\delta_0^*$  into the cavity, which is consistent with the elevated  $u_{\text{rms}}$  observed at the same depth into the cavity in the experiments. When the inverted hairpin vortices impinge against the downstream edge of the cavity, the heads are swept into the cavity while the approximately-streamwise-aligned legs

convect downstream of the cavity. Thus, the legs of the inverted hairpin vortices appear to account for the majority of the near-wall vortical structures downstream of the cavity downstream edge.

Additionally, wavepacket regeneration is also observed over the cavity. Figure 6.7(e,f) show the perturbation wall-normal velocity on a plane located at  $y/\delta_0^* = 0.5$  in presence and in absence of the cavity, respectively. Due to the no-penetration condition at the wall, perturbation wall-normal velocity is low at all coordinates except directly over the cavity. Wall-normal velocity induced by hairpin vortices prevailing in the spot grows to  $\pm 0.2U_0$  at a streamwise distance of around 30% of the cavity length downstream of the cavity upstream edge, where it coincides with a high level of streamwise vorticity as shown by the contour lines. Similar wall-normal perturbation velocity and streamwise vorticity distributions have been observed in several previous studies [39, 42]. Three streamwise-aligned upright hairpin vortices are observed to form at approximately the same time over the cavity, enclosed in a dashed ellipse in Figure 6.7e. These coordinates are occupied by a streamwise-continuous high-speed streak in absence of the cavity, which suggests that the three hairpin vortices formed over the cavity belong to the same wavepacket. Since the corresponding wavepacket is not observed in absence of the cavity, its accelerated formation over the cavity is suggested to also contribute to the elevated number of vortical structures downstream of the cavity.

The streamwise lengths of high- and low-speed streaks downstream of the cavity are observed to be shorter than those of the streaks within the spot in absence of the cavity. Such loss in streamwise coherence has been observed in past studies of turbulent boundary layers that convect over cavities [39, 42]. In addition to the shorter lengths, streaks over and downstream of the cavity are observed to be

streamwise-wavy with wavelengths that correlate with the spacing between sequential generations of inverted hairpin vortices, which are themselves correlated with each spanwise K-H roller that prevails outboard of the spot. The reduction in length and increase in streamwise-waviness of the streaks may explain the spanwise-smearred ensemble-averaged appearance of the spot measured downstream of the cavity in the experiments.

## 6.5 Lagrangian modeling of the K-H roller distortion by the disturbance of a turbulent spot

A Lagrangian model described in Section 4.2 was utilized to better understand the interaction of the rollers that develop through the K-H instability of the cavity shear layer with the streaky perturbations in velocity associated with the passing of a turbulent spot. The initially straight, spanwise-aligned vortex filament model was subjected to three different perturbations in velocity in three separate computations. First, a spanwise-sinusoidal perturbation in the streamwise component of velocity is applied. Second, the same perturbation is applied to the wall-normal component of velocity. Lastly, the two mentioned perturbations in the streamwise and wall-normal directions are linearly superimposed in phase. The wavelength and amplitude of the sinusoidal perturbations are  $4.5\delta_0^*$  and  $0.055U_0$ , respectively. These perturbation characteristics were chosen to approximate the perturbation of the cavity shear layer by the passing of a turbulent spot, albeit at a lower amplitude. The perturbations in all three cases are applied for the entire duration of the Lagrangian computations, which lasts for  $\Delta\tau = 22$ , which is the time required for a roller to convect from the middle of the cavity to the cavity downstream edge. Figure 6.8 shows the state of the vortex filament at the end of the three computations. In Figure 6.8a, the vortex

filament is only subject to a perturbation in the streamwise velocity component. This causes the initially-spanwise vorticity to be reoriented into the streamwise direction according to the wavelength of the imposed sinusoidal perturbation. Self-induced lift-up effects of the streamwise-aligned vorticity reorients the distorted segments of the vortex filament in the wall-normal direction where they are then stretched by the background shear. This results in hairpin-shaped loops in the vortex filament that have a streamwise length of about  $4\delta_0^*$  and a wall-normal height of around  $1\delta_0^*$ . In Figure 6.8b, the vortex filament is subject to a perturbation in the wall-normal velocity component. This immediately reorients the initially-spanwise vorticity into the wall-normal direction, prompting stretching in the streamwise direction by the background shear. The resulting streamwise growth rate of the hairpin-shaped loops is much higher than the growth rate observed for the vortex filament subject to only streamwise velocity perturbations. In the last scenario, shown in Figure 6.8c, where both streamwise and wall-normal components of velocity are perturbed in phase, the resulting vortex filament is even longer in the streamwise direction, and appears to take on a shape and dimension that are the linear superposition of the flow developments described in Figure 6.8a and b. This is expected given the linear nature of Laplace's equation for the velocity potential function which governs such flows that are driven by inviscid phenomena.

Figure 6.9 shows the effect of perturbation velocity amplitude on the temporal growth rate of the vortex filament, where the temporal growth rate is calculated by dividing the streamwise length of the filament at the end of the simulation normalized with  $\delta_0^*$  by the dimensionless time duration. The growth rate is noted to scale linearly on the streamwise perturbation amplitude, whereas the effect of wall-normal perturbation on the growth rate decreases with increasing perturbation amplitudes.

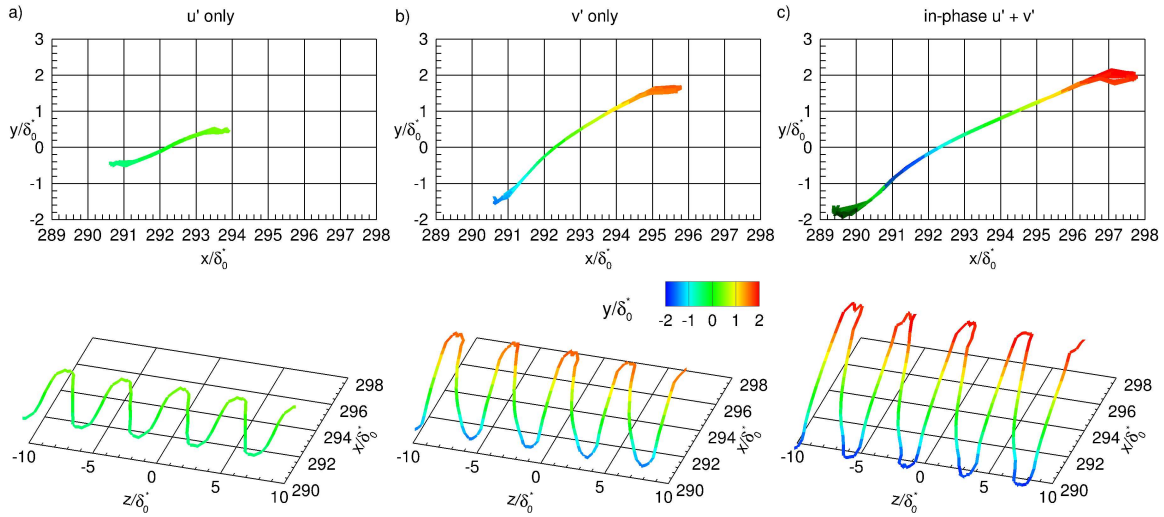


**Figure 6.8:** The state of vortex filaments at the end of the simulation period  $\Delta\tau = 22$  subject to (a)  $u'$ , (b)  $v'$ , and (c) in-phase  $u' + v'$  perturbations.

These results were noted to be insensitive to the chosen perturbation wavelength. The case with perturbations in both streamwise and wall-normal directions is deemed to most closely approximate the hairpin vortex dynamics of a turbulent spot as the spot traverses over the cavity. This is because both streamwise and wall-normal perturbations associated with the velocity streaks in the spot are free to develop in the absence of a wall.

To compare the results of the Lagrangian computation with streamwise and wall-normal velocity perturbations to the Eulerian computation, Figure 6.10 shows inverted hairpin vortices formed over the cavity for two sequential rollers in the Eulerian computation. The vortex filament and the inverted hairpin vortices (Figure 6.8c vs Figure 6.10b) are noted to have very similar shapes: each of them has a “head” located at a depth of  $2\delta_0^*$  into the cavity and each has legs pointed into the downstream direction with a tilt away from the cavity opening at a comparable angle. The highlighted inverted hairpin vortices in Region A develop over the same time interval as

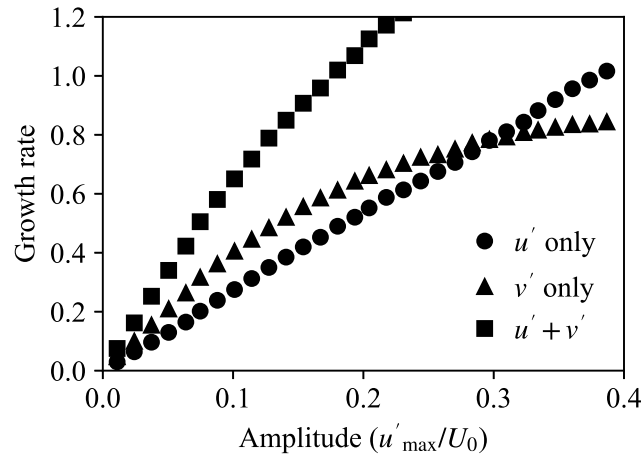


**Figure 6.9:** Streamwise growth rate of an initially straight spanwise vortex filament subject to perturbation velocity of varying amplitudes.

the Lagrangian vortex filament and both grow to streamwise length and wall-normal height values of about  $10\delta_0^*$  and  $4\delta_0^*$  respectively, comparing favourably to the results of the Lagrangian computation. The favourable agreement suggests that the inverted hairpin vortices formed over the cavity are products of the deformed spanwise vorticity grouped together by the K-H instability over the cavity. Inverted hairpin vortices are observed for nearly all roller generations while the spot is over the cavity, with the exception of the first two roller generations that only interact with the larger-scale structures near the leading edge of the spot. This exception is expected, as these

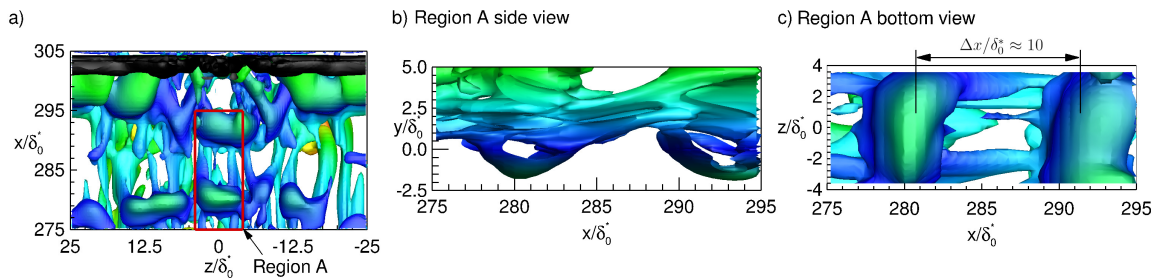


**Figure 6.10:** A typical inverted vortex pair formed within the cavity visualized through isosurfaces of  $Q/(U/\delta_0^*)^2 = 2 \times 10^{-4}$  at  $\tau = 451$ . (a) Bottom view; (b) side view of only region A; (c) bottom view of only region A.

structures are located farther away from the cavity opening and thus do not induce large enough velocity perturbation amplitudes to cause the formation of such inverted hairpin vortices directly over the cavity.

## 6.6 Interaction of the turbulent spot with the cavity shear layer along the lateral boundaries of the spot

In absence of the cavity, creation of new hairpin vortices at the lateral boundaries occurs mostly in the trailing half of the spot, as the “parent” hairpin vortices prevailing in this region of the spot are located closer to the wall [1]. In presence of the cavity, this process of hairpin vortex creation appears to accelerate as the trailing half of the spot approaches the cavity downstream edge. Figure 6.11 shows isosurfaces of  $Q$  for the  $-z$  half of the spot viewed from the bottom at three different instances in time. Figure 6.12 shows the perturbation streamwise velocity field at one of these times ( $\tau = 572$ ). At  $\tau = 539$  (Figure 6.11a), the trailing edge of the spot is just about to reach the cavity upstream edge and an inverted hairpin vortex labeled P0 is situated at the lateral edge of the spot. This vortex P0 is formed from a deformed K-H roller with the mechanisms described in Section 6.5, and is just about to impinge upon the cavity downstream edge. Between  $\tau = 539$  and  $\tau = 572$ , P0 impinges against the cavity downstream edge such that its head is swept into the cavity while the legs are convected downstream. At  $\tau = 572$  (Figure 6.11b), the spot is terminated at its spanwise edge by a streamwise oriented leg of the P0 vortex, which rotates in the opposite direction compared to an upright hairpin vortex that would occupy this region in absence of the cavity. This induces upwash outboard of the turbulent spot, and

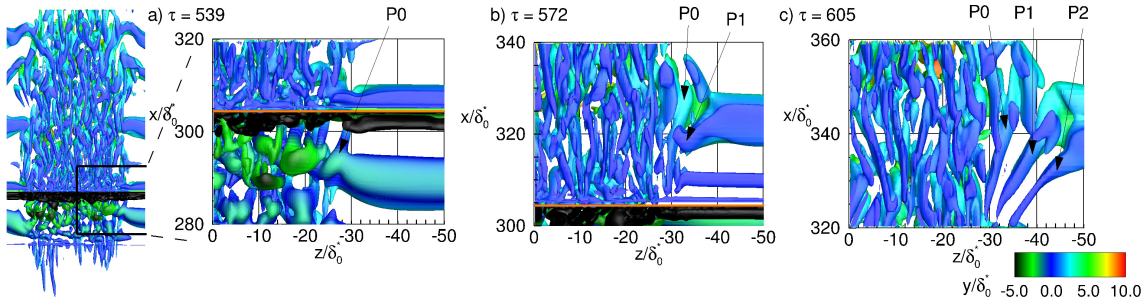


**Figure 6.11:** The turbulent spot viewed from the bottom visualized through isosurfaces of  $Q/(U/\delta_0^*)^2 = 2 \times 10^{-4}$  at (a)  $\tau = 539$ , (b)  $\tau = 572$ , and (c)  $\tau = 605$ .

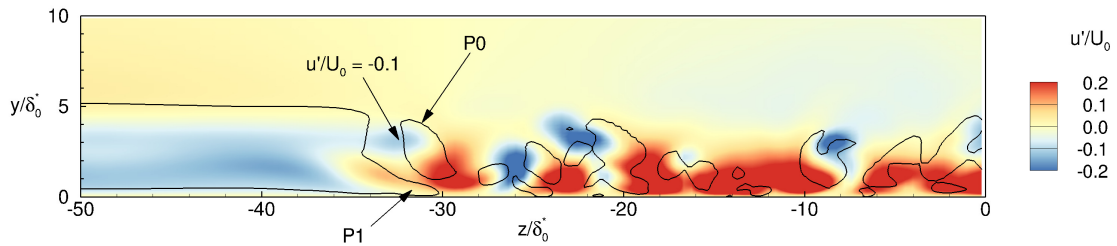


**Figure 6.12:** Flood plot of streamwise perturbation velocity in a  $y - z$  plane at  $x/\delta_0^* = 320$  and  $\tau = 572$  with contours of  $Q/(U/\delta_0^*)^2 = 2 \times 10^{-4}$  superimposed.

causes a low-speed streak with a magnitude of  $-0.1U_0$  to form (Figure 6.12). The low-speed streak reorients the initially-spanwise vorticity concentrated in the roller outboard of the spot backwards into the streamwise direction, which causes the formation of another inverted hairpin vortex, P1. Self-induced lift-up effect causes the head of P1 to be convected towards the wall, where torque exerted by wall shear appears to reduce the vorticity magnitude over time (Figure 6.11c). The inner-facing leg of P1 never forms completely, likely due to its viscous interaction with P0, which has a larger vorticity magnitude of the opposite sense of rotation. The process is repeated between  $\tau = 572$  and  $\tau = 605$ , which results in the formation of P2.

Multiple groups of such flow structures are observed on both lateral edges of the spot within  $100\delta_0^*$  downstream distance of the cavity downstream edge, which is consistent with the experimental results showing an increased lateral growth rate in the same streamwise region. In the simulation results, the edges of the turbulent spot are determined using threshold values for the magnitude of the streamwise component of vorticity. This approach follows the work of Strand and Goldstein [6] and Brinkerhoff and Yaras [1]. Specifically, eight uniformly spaced values of  $|\omega_x|\delta_0^*/U_0$  are averaged in the range of 0.06 and 0.19 and used as the threshold value. The uncertainty of the edge positions, and thus the spot dimensions, are calculated as the 95% confidence interval of this average. The coordinates of structures such as P0, P1, and P2 are consistently detected to coincide with the lateral boundaries of the spot, which suggests that the accelerated lateral growth of the spot over and downstream of the cavity can be attributed to these structures. To allow for comparison of the lateral

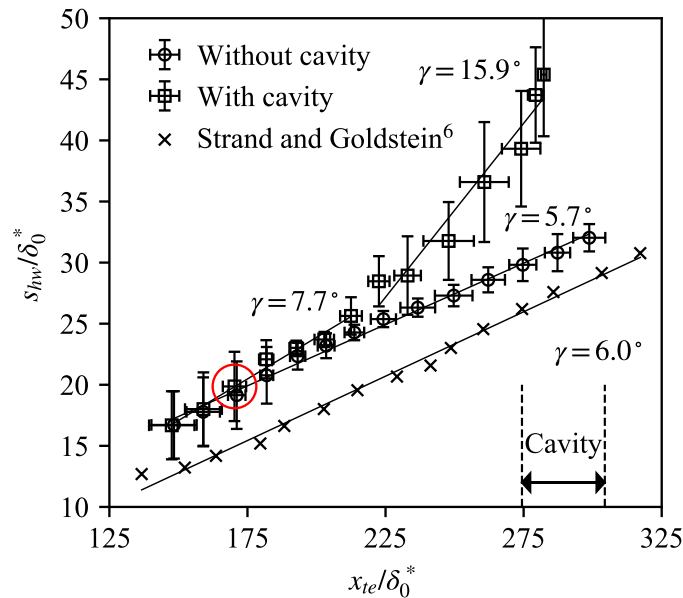


**Figure 6.13:** Variation of spot half-width with streamwise location of the trailing edge of the spot. The  $\gamma$  values denote half-spot spreading angles based on line fits to corresponding segments of data.

growth rate between the present and past numerical studies of turbulent spots in the absence of a cavity, the maximum spot half-width is plotted with respect to the streamwise location of the spot's trailing edge,  $x_{te}$ , in Figure 6.13. Since this abscissa makes it unclear when the spot encounters the cavity, a red circle is drawn to mark the spot trailing edge coordinate at the instant when the spot leading edge reaches cavity upstream edge. The results of Strand and Goldstein [6] show a spot that is consistently smaller than the present study. This discrepancy is likely due to the larger initial disturbance of the present study in the form of a strong wall-normal jet, whereas the spot of Strand and Goldstein [6] is triggered by the temporary presence of a small roughness element. The strong jet of the present study causes a rapid initial growth phase that results in a larger starting width for the spot. Before the spot encounters the cavity ( $x_{te} < 175$ ), the lateral growth rate of the turbulent spot agrees favourably with the growth rate in absence of a cavity of both the present study and the study by Strand and Goldstein [6]. The lateral growth rate of the spot remains unchanged as the leading half of the spot convects over the cavity ( $175 \leq x_{te} < 225$ ) and approximately doubles when the trailing half of the spot reaches close to the cavity downstream edge ( $x_{te} \geq 225\delta_0^*$ ). The latter trend is expected since the inverted hairpin vortices are predominantly generated in the trailing streamwise half of the spot. The increase in lateral growth rate and the width of the spot normalized by  $\delta_0^*$  agree favourably with the corresponding experimental data that was presented in Figure 6.4.

## 6.7 The wake region of the turbulent spot in the presence of feedback-driven oscillations

The wake region is a ubiquitous region upstream of the turbulent spot where a fuller streamwise velocity profile enhances stability [22]. The extra momentum that yields the fuller velocity profile is accounted for by the presence of high-speed streaks within the wake that are non-turbulent [1, 22, 67]. The formation of these streaks is promoted by wall-normal momentum transfer induced by perturbation spanwise vorticity associated with the turbulent spot in close proximity of the wall [1]. Defining the upstream boundary of the wake to coincide with the location where perturbation streamwise velocity is 4% of  $U_0$  and the downstream boundary to coincide with the spot trailing edge, the streamwise extent of the wake is 40% of the spot's length at the instant when the spot trailing edge is at the upstream end of the cavity. Figure 6.14 visualizes the interaction of the spot's wake with the cavity shear layer with  $Q$  isosurfaces at three equally-spaced instances in time. At  $\tau = 705$ , 80% of the wake length has already convected past the cavity downstream edge. The labeled K-H roller in Figure 6.14a is about to impinge on the downstream edge of the cavity. As this impingement process is about to occur, the upwash and downwash motions associated with this roller are observed to be spanwise nonuniform as illustrated through the perturbation velocity plots in Figure 6.15a and b. This non-uniformity is explained by the deformation of the K-H roller through its interaction with the high-speed streaks prevailing in the wake of the turbulent spot. These streaks are located within the dashed rectangles drawn on Figure 6.15a and are relatively faint due to their relatively low magnitude. At  $\tau = 727$ , the region of upwash induced by the K-H roller coincides with the downstream edge of the cavity and transfers fluid out of the cavity at a velocity magnitude of around  $0.15U_0$  (Figure 6.15d). In response, to locally satisfy conservation of mass,

near-wall fluid immediately downstream of the cavity is accelerated in the streamwise direction and momentarily increases the streamwise component of velocity at this region (Figure 6.15c). Since the upwash is spanwise non-uniform and is correlated with the existing streaks in the wake, the correlated streamwise acceleration follows the same pattern and increases the streak perturbation velocity amplitude to  $0.25U_0$ . Since these strengthened streaks are on the upstream side of the roller, they are preceded by a region of relatively low perturbation streamwise velocity due to the downwash of the roller on its downstream side. Between  $\tau = 727$  and  $\tau = 749$ , the newly-formed high-speed streaks reorient the spanwise vorticity of the K-H roller into the streamwise direction, resulting in the formation of a spanwise row of hairpin vortices (Figure 6.14c). This process is repeated for every roller that forms within the wake of the spot, although the time and hence streamwise distance required for each roller to reorganize into hairpin vortices is progressively longer towards the upstream end of the spot's wake. Since the streak-velocity amplitude within the spot's wake decreases in the upstream direction, each subsequent generation of high-speed streaks generated at the cavity downstream edge is amplified to progressively lower amplitudes, which in turn causes lesser reorientation of the roller's spanwise vorticity. Downstream of the cavity, wavepacket regeneration is observed along the legs of some of these roller-originating hairpin vortices, which implies that the length of the turbulent spot has effectively increased over the cavity. The simulation is not long enough to determine how long after the passing of the turbulent spot the cavity shear layer returns to its undisturbed state.

The stated observations in the numerical study are supported by the experimental measurements. Figure 6.16 shows the  $u_{\text{rms}}$  distribution  $5.6\delta_0^*$  distance downstream of

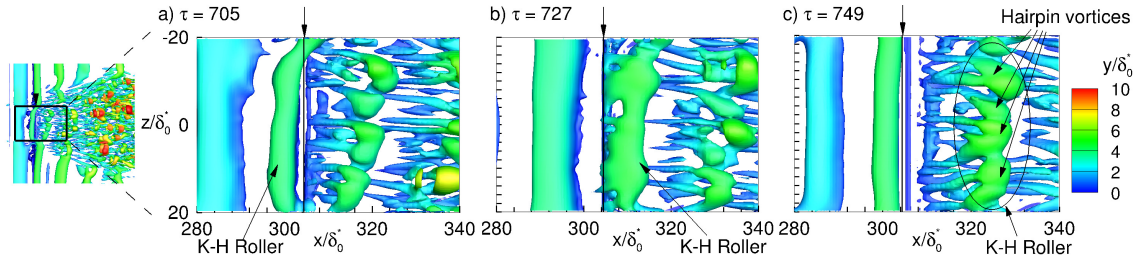


**Figure 6.14:** The evolution of a K-H roller as it interacts with the wake region, visualized through isosurfaces of  $Q/(U/\delta_0^*)^2 = 2 \times 10^{-4}$  at (a)  $\tau = 705$ , (b)  $\tau = 727$ , and (c)  $\tau = 749$ . Arrow points to the cavity downstream edge.

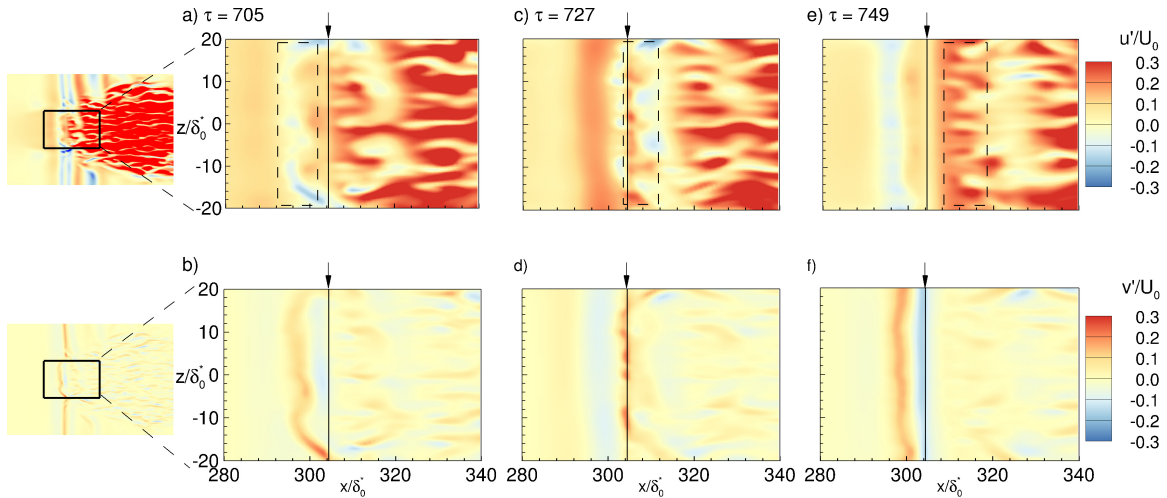


**Figure 6.15:** Perturbation streamwise (a,c,e) and wall-normal (b,d,f) velocity component at  $y/\delta_0^* = 1$ . Dash rectangles follow the same region within the wake as it convects over the cavity downstream edge. Arrow points to the cavity downstream edge.

the cavity during the passing of the turbulent spot for the three cavity lengths tested. The extent of the wake region in the time dimension is visualized with perturbation velocity contours of  $u'/U_0 = \pm 0.04$ . For the cavity length of  $L/\theta_s = 46.5$  (Figure 6.16a), the wake region remains relatively unchanged from its appearance observed just upstream of the cavity (Figure 6.1b). This seems to suggest that no significant changes occurs in the wake as a result of the interaction of the spot and its wake with the

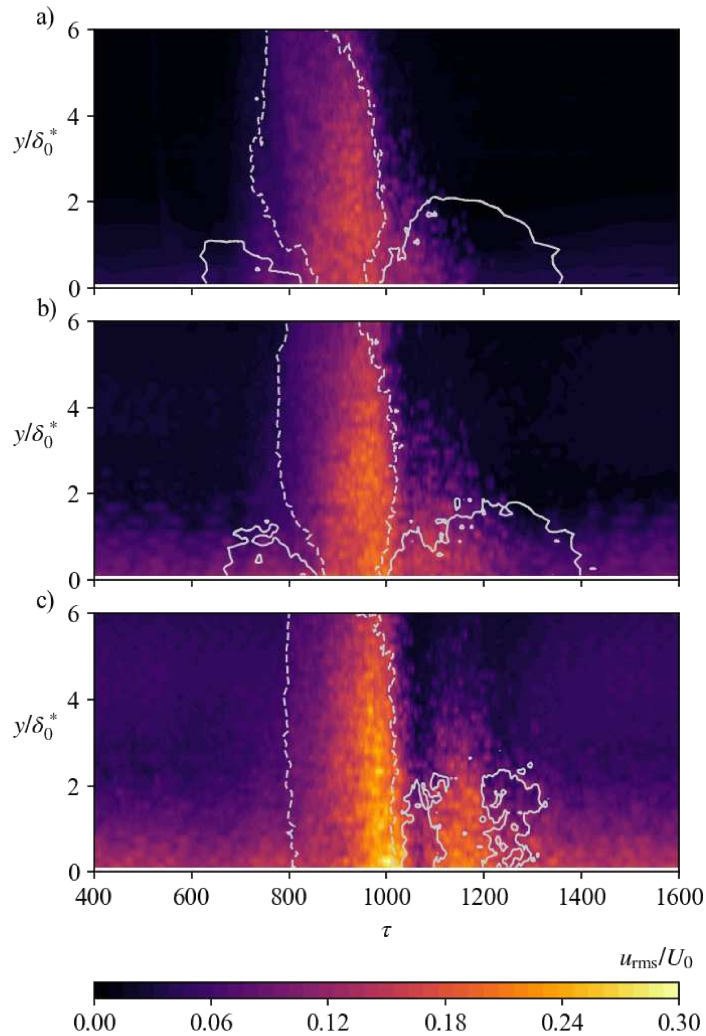


**Figure 6.16:** Distribution of  $u_{\text{rms}}/U_0$   $5.6\delta_0^*$  distance downstream of the cavity downstream edge along the spot centerline: (a)  $L/\theta_s = 46.7$ , (b)  $L/\theta_s = 54.4$ , and (c)  $L/\theta_s = 70.0$ . White solid lines:  $u'/U_0 = 0.04$ ; white dashed lines:  $u'/U_0 = -0.04$ .

cavity. Figure 6.16b and c show the spot structure after interaction with cavities of  $L/\theta_s = 54.4$  and  $L/\theta_s = 70.0$  length, respectively. In these cases, feedback-driven oscillation develops with amplitudes of  $0.05U_0$  and  $0.15U_0$ , respectively. The size of the region of elevated  $u_{\text{rms}}$  and its magnitude are noted to positively correlate with increasing oscillation amplitude. Specifically, the peak  $u_{\text{rms}}$  value within the wake of the spot that convects past the longest cavity ( $L/\theta_s = 70.0$ ) reaches a magnitude comparable to the values observed within the spot itself. Furthermore, at least 50% of the wake length has elevated values of  $u_{\text{rms}}$ . Although this cavity is longer than the one studied numerically, the feedback-driven velocity oscillation amplitude of the experiment is within 25% of that observed in the simulation. Thus, the elevated  $u_{\text{rms}}$  values observed in Figure 6.16c supports the simulation results where hairpin vortices are formed in the spot's wake from the rollers following their impingement with the cavity downstream edge. Since significantly elevated  $u_{\text{rms}}$  values in the spot's wake exist only when feedback-driven oscillations accompany the upwash and downwash motions induced by the rollers, the experiment supports the idea that the upwash induced by the rollers plays a crucial role in the genesis of hairpin vortices within the wake. Towards the upstream end of the wake, values of  $u_{\text{rms}}$  return to the background level. This again is consistent with the simulation results, where the formation of hairpin vortices was described to require progressively longer periods of time towards the upstream end of the wake.

## Chapter 7

### Conclusions and future work

The evolution of coherent structures within an artificially-triggered turbulent spot convecting past a deep cavity with a nominal aspect ratio of  $L/D = 0.1$  is studied with hotwire measurements in a close-circuit wind tunnel. The experimental results are complemented by dynamically similar direct numerical simulations and Lagrangian computations of an idealized vortex filament representing a K-H roller of the cavity shear layer subject to spanwise-sinusoidal velocity perturbations to mimic the effect of the turbulent spot on the roller. The experiments are conducted with a Reynolds number of 195,000 at the cavity upstream edge with three different cavity lengths of  $L/\theta_s = 46.5, 54.4,$  and  $70.0$ . The simulations are performed with a Reynolds number of 170,610 and a single cavity length of  $L/\theta_s = 46.5$ .

The interaction of the turbulent spot with the cavity shear layer is observed to produce a notable increase in the number of coherent vortical structures associated with the spot. Most of these flow structures are inverted hairpin vortices that are created through interaction of the K-H rollers of the cavity shear layer with the trailing half of the spot. Along the lateral edges of the spot, the K-H rollers of the cavity shear layer are deformed to approximately the shape of an inverted hairpin vortex. In each instance, the induced velocity of this flow structure reorients the spanwise vorticity

concentrated in the K-H roller on its outboard side into the streamwise direction, forming a new vortex that in turn repeats the process farther along the span of the roller. This process is noted to result in approximately doubling of the lateral growth rate of the spot, which continues to remain in effect as the spot convects over the surface downstream of the cavity. In the wake of the turbulent spot, the K-H rollers upstream of the turbulent spot are observed to deform into spanwise-wavy patterns by the streamwise velocity streaks in the wake of the spot. Interaction of these deformed K-H rollers with the downstream edge of the cavity is shown to strengthen the prevailing streamwise streaks, which in turn promote the formation of spanwise rows of hairpin vortices from the deformed K-H rollers. This development is noted to be correlated with the presence of strong feedback-driven oscillations in the cavity flow, and results in significant increase in the streamwise size of the turbulent spot.

The present study is limited to zero streamwise pressure gradient. Given the well-known effects of streamwise pressure gradients on shear layer stability, the next natural phase of this study would be investigation of the effects of streamwise favourable and adverse pressure gradients on the flow physics identified in the present study. It is plausible that these flow physics could be further altered by cavity lengths and depths beyond the limited ranges considered in the present study. Based on existing knowledge of the effects of these cavity geometric parameters on the cavity flow field, it would be reasonable to expect that interaction of boundary layer turbulence with the cavity free-shear layer may be altered by such geometric features. Consideration of such geometric variations for the cavity would therefore be a worthwhile future study.

## References

- [1] J. R. Brinkerhoff and M. I. Yaras, “Numerical investigation of the generation and growth of coherent flow structures in a triggered turbulent spot,” *J. Fluid Mech.*, vol. 759, pp. 257–294, Nov 2014.
- [2] X. Wu, P. Moin, J. M. Wallace, J. Skarda, A. Lozano-Durán, and J.-P. Hickey, “Transitional–turbulent spots and turbulent–turbulent spots in boundary layers,” *Proc. Natl. Acad. Sci. U.S.A.*, vol. 114, pp. E5292–E5299, Jul 2017.
- [3] X. Wu, J. M. Wallace, and J.-P. Hickey, “Boundary layer turbulence and freestream turbulence interface, turbulent spot and freestream turbulence interface, laminar boundary layer and freestream turbulence interface,” *Phys. Fluids*, vol. 31, p. 045104, Apr 2019.
- [4] R. J. Adrian, C. D. Meinhart, and C. D. Tomkins, “Vortex organization in the outer region of the turbulent boundary layer,” *J. Fluid Mech.*, vol. 422, pp. 1–54, Nov 2000.
- [5] C. Lee and X. Jiang, “Flow structures in transitional and turbulent boundary layers,” *Phys. Fluids*, vol. 31, p. 111301, Nov 2019.
- [6] J. S. Strand and D. B. Goldstein, “Direct numerical simulations of riblets to constrain the growth of turbulent spots,” *J. Fluid Mech.*, vol. 668, pp. 267–292, Feb 2011.

- [7] D. Goldstein, J. Chu, and G. Brown, “Lateral spreading mechanism of a turbulent spot and a turbulent wedge,” *Flow Turbul. Combust.*, vol. 98, pp. 21–35, Jan 2017.
- [8] S. I. Chernyshenko and M. F. Baig, “The mechanism of streak formation in near-wall turbulence,” *J. Fluid Mech.*, vol. 544, pp. 99–131, Dec 2005.
- [9] A. E. Perry, T. T. Lim, and E. W. Teh, “A visual study of turbulent spots,” *J. Fluid Mech.*, vol. 104, pp. 387–405, Mar 1981.
- [10] C. R. Smith and S. P. Metzler, “The characteristics of low-speed streaks in the near-wall region of a turbulent boundary layer,” *J. Fluid Mech.*, vol. 129, pp. 27–54, Apr 1983.
- [11] P. Andersson, L. Brandt, A. Bottaro, and D. S. Henningson, “On the breakdown of boundary layer streaks,” *J. Fluid Mech.*, vol. 428, pp. 29–60, Feb 2001.
- [12] J. R. Brinkerhoff and M. I. Yaras, “Numerical investigation of transition in a boundary layer subjected to favourable and adverse streamwise pressure gradients and elevated free stream turbulence,” *J. Fluid Mech.*, vol. 781, pp. 52–86, Oct 2015.
- [13] C. R. Smith, “A synthesized model of the near-wall behavior in turbulent boundary layers,” University of Missouri-Rolla, 1984.
- [14] B. A. Singer and R. D. Joslin, “Metamorphosis of a hairpin vortex into a young turbulent spot,” *Phys. Fluids*, vol. 6, pp. 3724–3736, Nov 1994.
- [15] A. Schröder and J. Kompenhans, “Investigation of a turbulent spot using multi-plane stereo particle image velocimetry,” *Exp. Fluids*, vol. 36, pp. 82–90, Jan 2004.

- [16] I. Wygnanski, M. Sokolov, and D. Friedman, “On a turbulent ‘spot’ in a laminar boundary layer,” *J. Fluid Mech.*, vol. 78, pp. 785–819, 1976.
- [17] J. P. Gostelow, N. Melwani, and G. J. Walker, “Effects of streamwise pressure gradient on turbulent spot development,” *J. Turbomach.*, vol. 118, pp. 737–743, Oct 1996.
- [18] S. K. Reinink and M. I. Yaras, “Study of coherent structures of turbulence with large wall-normal gradients in thermophysical properties using direct numerical simulation,” *Phys. Fluids*, vol. 27, p. 065113, Jun 2015.
- [19] S. Suryanarayanan, D. B. Goldstein, A. R. Berger, E. B. White, and G. L. Brown, “Effect of pressure gradients on the different stages of roughness induced boundary layer transition,” *Int. J. Heat Fluid Flow*, vol. 86, p. 108688, Dec 2020.
- [20] T. P. Chong and S. Zhong, “On the three-dimensional structure of turbulent spots,” *J. Turbomach.*, vol. 127, pp. 545–551, Jul 2005.
- [21] Y. Katz, A. Seifert, and I. Wygnanski, “On the evolution of the turbulent spot in a laminar boundary layer with a favourable pressure gradient,” *J. Fluid Mech.*, vol. 221, pp. 1–22, Dec 1990.
- [22] J. P. Gostelow, G. J. Walker, W. J. Solomon, G. Hong, and N. Melwani, “Investigation of the calmed region behind a turbulent spot,” *J. Turbomach.*, vol. 119, pp. 802–809, Oct 1997.
- [23] A. Michalke, “On spatially growing disturbances in an inviscid shear layer,” *J. Fluid Mech.*, vol. 23, pp. 521–544, Nov 1965.
- [24] C. Ho and P. Huerre, “Perturbed free shear layers,” *Annu. Rev. Fluid Mech.*, vol. 16, pp. 365–422, Jan 1984.

- [25] D. Rockwell and E. Naudascher, “Self-sustained oscillations of impinging free shear layers,” *Annu. Rev. Fluid Mech.*, vol. 11, no. 1, pp. 67–94, 1979.
- [26] D. Rockwell and E. Naudascher, “Review – self-sustaining oscillations of flow past cavities,” *J. Fluids Eng.*, vol. 100, pp. 152–165, Jun 1978.
- [27] V. Sarohia, “Experimental investigation of oscillations in flows over shallow cavities,” *AIAA J.*, vol. 15, pp. 984–991, 1977.
- [28] T. M. Faure, P. Adrianos, F. Lusseyran, and L. Pastur, “Visualizations of the flow inside an open cavity at medium range reynolds numbers,” *Exp. Fluids*, vol. 42, pp. 169–184, Feb 2007.
- [29] N. Arya and A. De, “Effect of vortex and entropy sources in sound generation for compressible cavity flow,” *Phys. Fluids*, vol. 33, p. 046107, Apr 2021.
- [30] D. Rockwell and C. Knisely, “The organized nature of flow impingement upon a corner,” *J. Fluid Mech.*, vol. 93, pp. 413–432, Aug 1979.
- [31] Q. Liu and D. Gaitonde, “Acoustic response of turbulent cavity flow using resolvent analysis,” *Phys. Fluids*, vol. 33, p. 056102, May 2021.
- [32] S. Yamouni, D. Sipp, and L. Jacquin, “Interaction between feedback aeroacoustic and acoustic resonance mechanisms in a cavity flow: a global stability analysis,” *J. Fluid Mech.*, vol. 717, pp. 134–165, Feb 2013.
- [33] S. M. Grace, W. G. Dewar, and D. E. Wroblewski, “Experimental investigation of the flow characteristics within a shallow wall cavity for both laminar and turbulent upstream boundary layers,” *Exp. Fluids*, vol. 36, pp. 791–804, May 2004.

- [34] G. Ashcroft and X. Zhang, “Vortical structures over rectangular cavities at low speed,” *Phys. Fluids*, vol. 17, p. 015104, Dec 2004.
- [35] L. Ukeiley and N. Murray, “Velocity and surface pressure measurements in an open cavity,” *Exp. Fluids*, vol. 38, pp. 656–671, May 2005.
- [36] C. Knisely and D. Rockwell, “Self-sustained low-frequency components in an impinging shear layer,” *J. Fluid Mech.*, vol. 116, pp. 157–186, Mar 1982.
- [37] J. Basley, L. R. Pastur, N. Delprat, and F. Lusseyran, “Space-time aspects of a three-dimensional multi-modulated open cavity flow,” *Phys. Fluids*, vol. 25, p. 064105, Jun 2013.
- [38] D. Rockwell and C. Knisely, “Observations of the three-dimensional nature of unstable flow past a cavity,” *Phys. Fluids*, vol. 23, pp. 425–431, Mar 1980.
- [39] K. Chang, G. Constantinescu, and S.-O. Park, “Analysis of the flow and mass transfer processes for the incompressible flow past an open cavity with a laminar and a fully turbulent incoming boundary layer,” *J. Fluid Mech.*, vol. 561, pp. 113–145, Aug 2006.
- [40] J. C. Lin and D. Rockwell, “Organized oscillations of initially turbulent flow past a cavity,” *AIAA J.*, vol. 39, no. 6, pp. 1139–1151, 2001.
- [41] S. Bian, J. F. Driscoll, B. R. Elbing, and S. L. Ceccio, “Time resolved flow-field measurements of a turbulent mixing layer over a rectangular cavity,” *Exp. Fluids*, vol. 51, pp. 51–63, Jul 2011.
- [42] C. Haigermoser, L. Vesely, M. Novara, and M. Onorato, “A time-resolved particle image velocimetry investigation of a cavity flow with a thick incoming turbulent boundary layer,” *Phys. Fluids*, vol. 20, Oct 2008.

- [43] H. Yao, R. K. Cooper, and S. Raghunathan, “Numerical simulation of incompressible laminar flow over three-dimensional rectangular cavities,” *J. Fluids Eng.*, vol. 126, pp. 919–927, Nov 2004.
- [44] S. Beguet, J. Perraud, M. Forte, and J.-P. Brazier, “Modeling of transverse gaps effects on boundary-layer transition,” *J. Aircr.*, vol. 54, no. 2, pp. 794–801, 2017.
- [45] W. J. Nelson and J. M. Cabbage Jr, “Effects of slot size and geometry on the flow in rectangular tunnels at mach numbers up to 1.4,” Tech. Rep. NACA-RM-L53B16, NASA Langley, 1953.
- [46] S. B. Berndt, “Inviscid theory of wall interference in slotted test sections,” *AIAA J.*, vol. 15, no. 9, pp. 1278–1287, 1977.
- [47] S. Raimondo and P. Clark, *Slotted wall test section for automotive aerodynamic test facilities*. AIAA, 1982.
- [48] J. T. Templin and S. Raimondo, “Experimental evaluation of test section boundary interference effects in road vehicle tests in wind tunnels,” *J. Wind Eng. Ind. Aerod.*, pp. 129–148, Jun 1986.
- [49] M. I. Yaras, “An experimental study of artificially-generated turbulent spots under strong favorable pressure gradients and freestream turbulence,” *J. Fluids Eng.*, vol. 129, pp. 563–572, May 2007.
- [50] D. B. Ancrum and M. I. Yaras, “Measurements of the effects of streamwise riblets on boundary layer turbulence,” *J. Fluids Eng.*, vol. 139, p. 111203, Nov 2017.
- [51] H. H. Bruun, *Hot-wire anemometry: principles and signal analysis*. Oxford University Press, 1995.

- [52] K. K. M. Ahuja, “Effects of cavity dimensions, boundary layer, and temperature on cavity noise with emphasis on benchmark data to validate computational aeroacoustic codes,” Tech. Rep. NASA CR-4653, NASA Langley, Apr 1995.
- [53] H. T. Kim, S. J. Kline, and W. C. Reynolds, “The production of turbulence near a smooth wall in a turbulent boundary layer,” *J. Fluid Mech.*, vol. 50, pp. 133–160, Nov 1971.
- [54] M. Stanislas, L. Perret, and J.-M. Foucaut, “Vortical structures in the turbulent boundary layer: a possible route to a universal representation,” *J. Fluid Mech.*, vol. 602, pp. 327–382, May 2008.
- [55] J. R. Brinkerhoff and M. I. Yaras, “Interaction of viscous and inviscid instability modes in separationbubble transition,” *Phys. Fluids*, vol. 23, p. 124102, Dec 2011.
- [56] C. Azih, J. R. Brinkerhoff, and M. I. Yaras, “Direct numerical simulation of convective heat transfer in a zero-pressure- gradient boundary layer with supercritical water,” *J. Therm. Sci.*, vol. 21, pp. 49–59, Feb 2012.
- [57] C. Azih and M. I. Yaras, “Effects of spatial gradients in thermophysical properties on the topology of turbulence in heated channel flow of supercritical fluids,” *Phys. Fluids*, vol. 30, p. 015108, Jan 2018.
- [58] H. Choi and P. Moin, “Effects of the computational time step on numerical solutions of turbulent flow,” *J. Comput. Phys.*, vol. 113, no. 1, pp. 1–4, 1994.
- [59] H. Valtchanov, J. R. Brinkerhoff, and M. I. Yaras, “Numerical study of passive forcing on the secondary instability of a laminar planar free shear layer,” *J. Turbul.*, vol. 21, pp. 259–285, Jun 2020.

- [60] J. Jiménez, S. Hoyas, M. P. Simens, and Y. Mizuno, “Turbulent boundary layers and channels at moderate reynolds numbers,” *J. Fluid Mech.*, vol. 657, pp. 335–360, Aug 2010.
- [61] B. R. McAuliffe and M. I. Yaras, “Transition mechanisms in separation bubbles under low- and elevated-freestream turbulence,” *J. Turbomach.*, vol. 132, p. 011004, 2010.
- [62] M. Gad-El-Hak, R. F. Blackwelder, and J. J. Riley, “On the growth of turbulent regions in laminar boundary layers,” *J. Fluid Mech.*, vol. 110, pp. 73–95, Sep 1981.
- [63] M. B. Tracy and B. Plentovich, “Cavity unsteady-pressure measurements at subsonic and transonic speeds,” Tech. Rep. NASA TP-3669, NASA, 1997.
- [64] R. J. Volino, M. P. Schultz, and C. M. Pratt, “Conditional sampling in a transitional boundary layer under high freestream turbulence conditions,” *J. Fluids Eng.*, vol. 125, pp. 28–37, Jan 2003.
- [65] C. Vanderwel and S. Tavoularis, “Coherent structures in uniformly sheared turbulent flow,” *J. Fluid Mech.*, vol. 689, pp. 434–464, Dec 2011.
- [66] S. Dong, A. Lozano-Durán, A. Sekimoto, and J. Jiménez, “Coherent structures in statistically stationary homogeneous shear turbulence,” *J. Fluid Mech.*, vol. 816, pp. 167–208, Apr 2017.
- [67] D. Sabatino and C. Smith, “Turbulent spot flow topology and mechanisms for surface heat transfer,” *J. Fluid Mech.*, vol. 612, pp. 81–105, 2008.

## Appendix A

# Design of a 2D probe traverse system for the experiment

A 2D traverse system was designed and built for the wind tunnel located in ME 3224 to automatically move the pitot and hotwire probes during the experiment with the desired spatial resolution and positioning accuracy. The main design objectives of the system were to:

- Enable automated traverse in the wall-normal and streamwise direction;
- provide a positioning increment of 0.025 mm;
- provide at least 50 mm of traverse distance in the wall-normal direction;
- be easily relocatable in the streamwise direction to cover a streamwise measurement range beyond the traverse range of the system;
- have adequate stiffness and vibration characteristics;
- and allow for installation by a single person.

The traverse system consists of two parts: the motion-related mechanism which consists of two ball-screw-based linear axes each with a stroke of 100 mm (Figure A.1),

and a cradle that secures the linear axes over the test section (Figure A.2). Each axis is driven by a NEMA23 stepper motor (A). The two axes are joined together by a 3D-printed ABS adapter plate (B). To validate that the yield stress of the 3D-printed ABS is sufficient to secure the vertical axis, a conservative calculation was performed by assuming that the weight of the vertical axis would be countered by a single bolt through one of the off-centered holes in the adapter plate B. The calculation results in a maximum stress value that is less than 20% of the value of yield stress for the 3D-printed ABS, which was deemed to be sufficient. The probe stem was secured within a shaft collar mounted on another 3D printed support bracket (C). The two ribs on the back of B and C are added for alignment purposes. A secondary support plate (D) is included to ensure the probe stem has two points of contact. The system was calibrated and yielded spatial resolution and positioning accuracy of  $0.0247 \pm 0.0003$  mm for both axis over the entire stroke. The traverse system has a mass of 10 kg.

The cradle component of the system designed to hang off a pair of C-channels (E) of a pre-existing support frame is located directly over the test section of the wind tunnel located in room 3224 of the Mackenzie Building. The cradle structure makes use of 20 mm 80/20<sup>®</sup> aluminum extrusions, with the exception of the traverse mount (F), which uses 30 mm 80/20<sup>®</sup> extrusions to better align with the linear axis. Fasteners mostly consist of M5 hex socket bolts, although a small number of M4, M6, 8-32, and 6-32 machine screws are required to secure third-party parts such as the shaft collar and the toggle clamps. A slide-and-lock docking system (G1, H1) was designed to allow the traverse system to be taken off the cradle with ease. The same dock is duplicated at a higher position (H2) to optionally store the traverse system when it is not in use. The cradle without the motion systems has a mass of 6 kg.

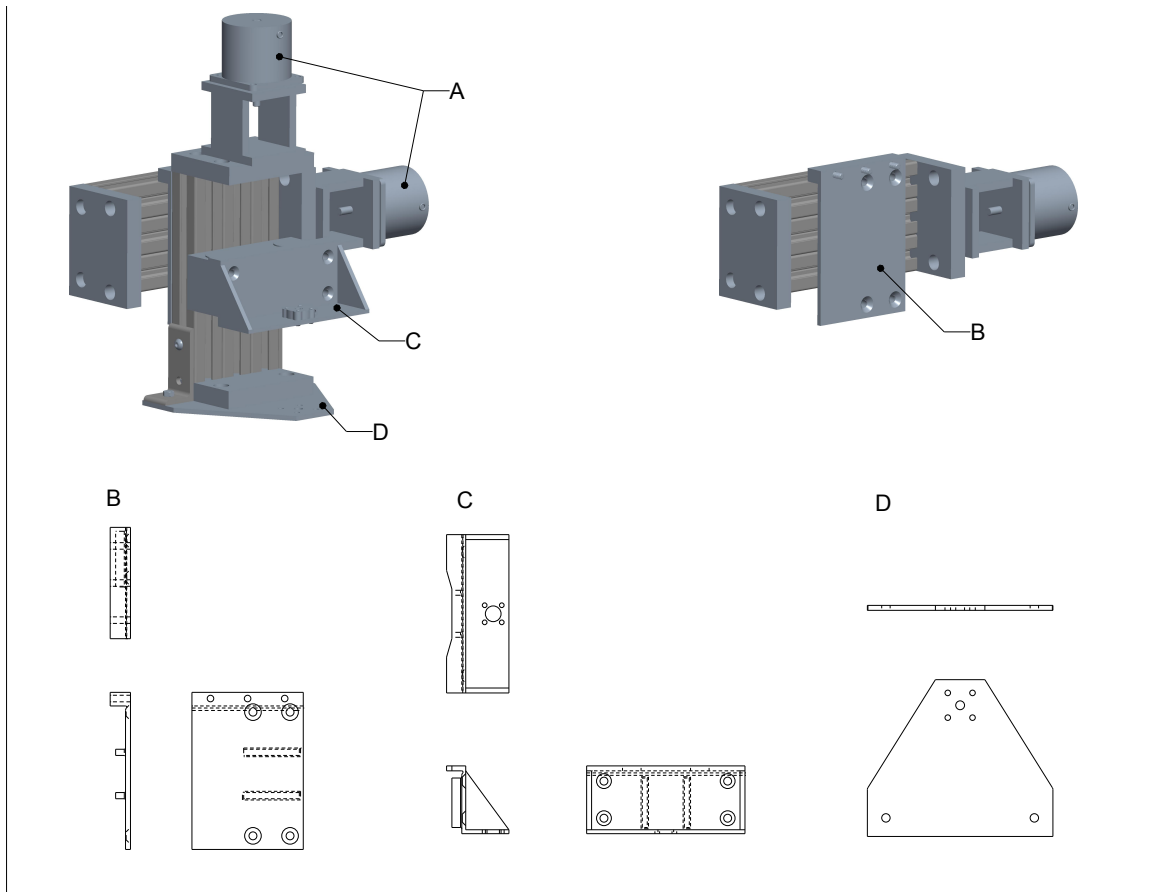


**Figure A.1:** Two off-the-shelf linear motion systems combined to function as a 2D traverse system

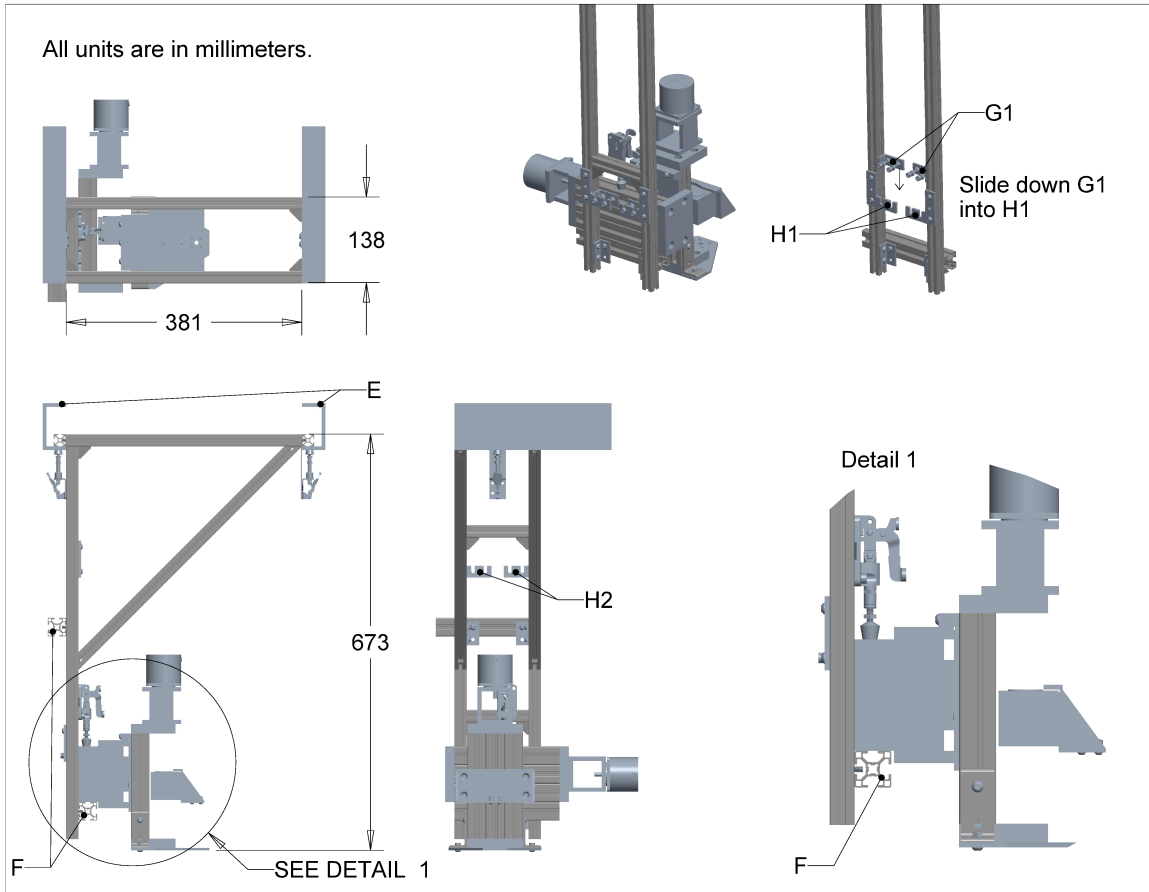


**Figure A.2:** The traverse system and its cradle. Detail shows the mounting of the motion systems onto the cradle.

## Appendix B

# Experimental calibrations

### B.1 Pitot probe

The experiments were conducted with a single-sensor hotwire probe connected to an AN-1003 constant-temperature anemometer measuring the instantaneous local flow velocity as described in the main text. The velocity measured with the hotwire probe is normalized by a reference velocity determined from the freestream dynamic pressure,  $P_{\text{inlet}} - P_0$ , measured with a Scanivalve ZOC17/16Px pressure transducer.  $P_{\text{inlet}}$  is the static pressure measured downstream of the wind-tunnel contraction at the test-section inlet and  $P_0$  is the stagnation pressure measured at the inlet of the contraction.

Three Scanivalve ZOC17/16Px pressure transducers with serial numbers of 294, 291, and 280 were setup in differential mode for the present study. Only channel 16 was used on each transducer as the channel selector described in Appendix C.3 was not available at the time of the experiment. To calibrate these transducers, channel 16 of the each transducer was in parallel connected to one side of a high-precision U-shaped manometer filled with water while the reference port of each transducer was connected to a syringe, which was connected to the other side of the manometer.

**Table B.1:** ZOC17/16Px calibration coefficients

Serial number	Calibration coefficient (Pa/mV)	Used in experiment
280	$1.555 \pm 0.01$	Yes
291	$1.668 \pm 0.01$	No
294	$1.443 \pm 0.01$	Yes

The full-scale range of the ZOC17/16Px transducer is 10 inches of water (2.5 kPa) which far exceeds the differential pressure range expected in the experiments. A total of 60 measurements were made between  $-800$  Pa and  $800$  Pa where 40 of the measurements were distributed within  $-200$  Pa and  $200$  Pa. While three transducers were calibrated, only two were used (serial number 280 and 294). The calibrated coefficients are presented in Table B.1.

## B.2 Hotwire probe

The hotwire system was calibrated at the beginning of each day of experiment. The probe was calibrated using a TSI Air Velocity Calibrator with 20 equidistant values of velocity between 0 and 12 m/s. An example calibration curve is provided in Figure B.1. In each instance, a 6th-order polynomial was fitted to the calibration data. The resulting curve was checked at the end of each experiment day for drift. The largest drift observed was 5% and 9% for velocity values above and below 1.5 m/s respectively.

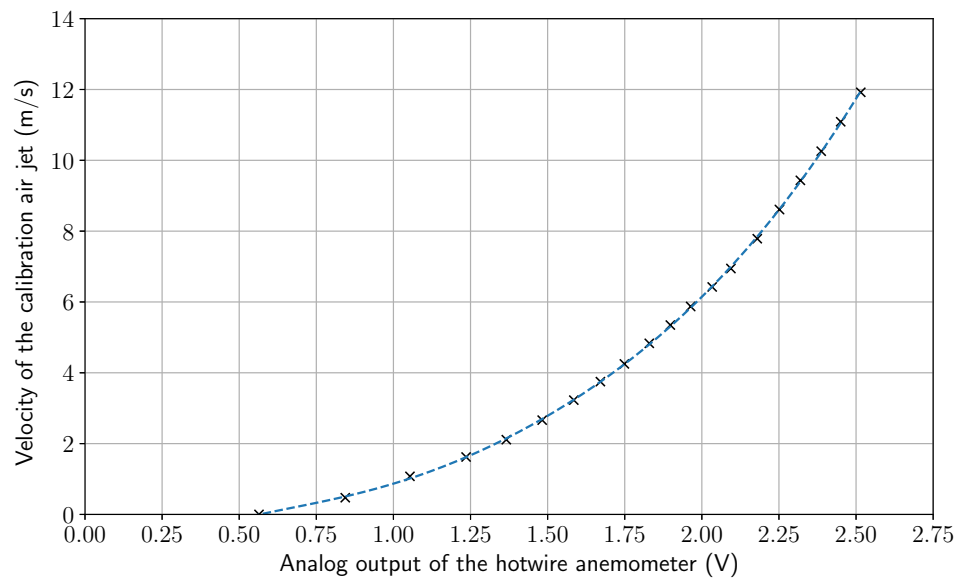


**Figure B.1:** An instance of the calibration curve of the hotwire probe performed with 20 values of velocity

## Appendix C

# Custom electronics for the experiment

### C.1 Pulse generator

The turbulent spot was generated via a puff of air in the experiment. A 24VDC solenoid valve was flipped on and off at a configurable frequency. A data acquisition system (DAQ) was configured to begin acquiring a fixed number of samples at the same moment the valve turns on.

For reasons that are beyond the scope of this document, the DAQ was setup to acquire hotwire data once its trigger input line reaches 2VDC. This trigger input line was initially connected to a waveform generator that can generate a 50% duty cycle square wave of just over 2V amplitude. Two problems exist with this setup: (a) the 24VDC solenoid cannot be activated by the 2VDC signal and (b) the 50% duty cycle and a one-second interval between two sequential spots would imply an air puff of 0.5 seconds duration, which would result in the creation of a turbulent wedge instead of the intended turbulent spot.

Thus, a custom pulse generator was built. The 2VDC signal of the waveform generator is connected to the analog input terminal of an Arduino-Nano-compatible microcontroller. When the 2VDC signal is read by the microcontroller, it sends out

a 5VDC pulse of a configurable duration to a MOSFET (P/N: FQP30N06L), which then activates the solenoid via a 24VDC power supply. The duration of the 5VDC pulse can be configured with two buttons: the green button (BTN1) increases the pulse duration up to a maximum duration of 1000ms, at which point the duration is reset to 0. The blue button (BTN2) controls the speed at which one can cycle through the possible pulse durations using the green button. The pulse duration is displayed in a dot-matrix LCD module. The whole unit is powered via its mini-USB port and it is also re-programmable via the same port. The code for the system is shown in Listing C.1. The complete circuit diagram is shown in Figure C.1.

### Listing C.1: Pulse generator source code

```
#include "Arduino.h"
#include <LiquidCrystal.h>
#include <Bounce2.h>

// The code here is compiled via PlatformIO and possible compilable via the
// Arduino IDE. The LiquidCrystal and Bounce2 library is needed.

#define PIN_RS 12
#define PIN_RW 11
#define PIN_E 10
#define PIN_D4 9
#define PIN_D5 8
#define PIN_D6 7
#define PIN_D7 6

#define PIN_BTN1 3
#define PIN_BTN2 4

#define PIN_INPUT A3
#define PIN_OUTPUT 2
#define PIN_LED 13

// Defines the maximum pulse width in ms.
#define MAX_WIDTH 1001

// Defines the threshold voltage to trigger the pulse
// This value is out of 1023 and 1023 is 5V. It is based on the ADC of the arduino.
#define INPUT_THRESHOLD 390

uint16_t on_width = 11, step = 1;
bool update_display = false;
int last_input_state = 0, current_input_state = 0;

char line1[17] = {0};
char line2[17] = {0};

LiquidCrystal lcd(PIN_RS, PIN_RW, PIN_E, PIN_D4, PIN_D5, PIN_D6, PIN_D7);
Bounce btn1 = Bounce();
```

```

Bounce btn2 = Bounce();

void pulse() {
  digitalWrite(PIN_OUTPUT, HIGH);
  digitalWrite(PIN_LED, HIGH);
  if (on_width < 15) {
    // Maximum value for delayMicroseconds is uint16_t, which is about 16ms
    delayMicroseconds(on_width * 1000);
  } else {
    delay(on_width);
  }
  digitalWrite(PIN_OUTPUT, LOW);
  digitalWrite(PIN_LED, LOW);
}

void refresh_display() {
  sprintf(line1, "WIDTH=%4dms", on_width);
  sprintf(line2, "INCR.= %4dms", step);
  lcd.setCursor(0, 0);
  lcd.print(line1);
  lcd.setCursor(0, 1);
  lcd.print(line2);
}

void setup() {
  // set up the LCD's number of columns and rows:
  lcd.begin(16, 2);
  btn1.attach(PIN_BTN1, INPUT);
  btn1.interval(25);
  btn2.attach(PIN_BTN2, INPUT);
  btn2.interval(25);
  pinMode(PIN_LED, OUTPUT);
  pinMode(PIN_OUTPUT, OUTPUT);
  refresh_display();
}

void loop() {
  update_display = false;
  btn1.update();
  btn2.update();

  if (btn1.fell()) {
    // button 1 clicked
    on_width = (on_width + step);
    if (on_width > MAX_WIDTH) {
      on_width = 0;
    }
    update_display = true;
  }

  if (btn2.fell()) {
    if (step < 10) {
      step++;
    } else {
      step += 10;
    }
  }

  step = step % 110;
}

```

```

    update_display = true;
}

current_input_state = analogRead(PIN_INPUT) > INPUT_THRESHOLD;
if (current_input_state && !last_input_state) {
    pulse();
}
last_input_state = current_input_state;

if (update_display) refresh_display();
}

```

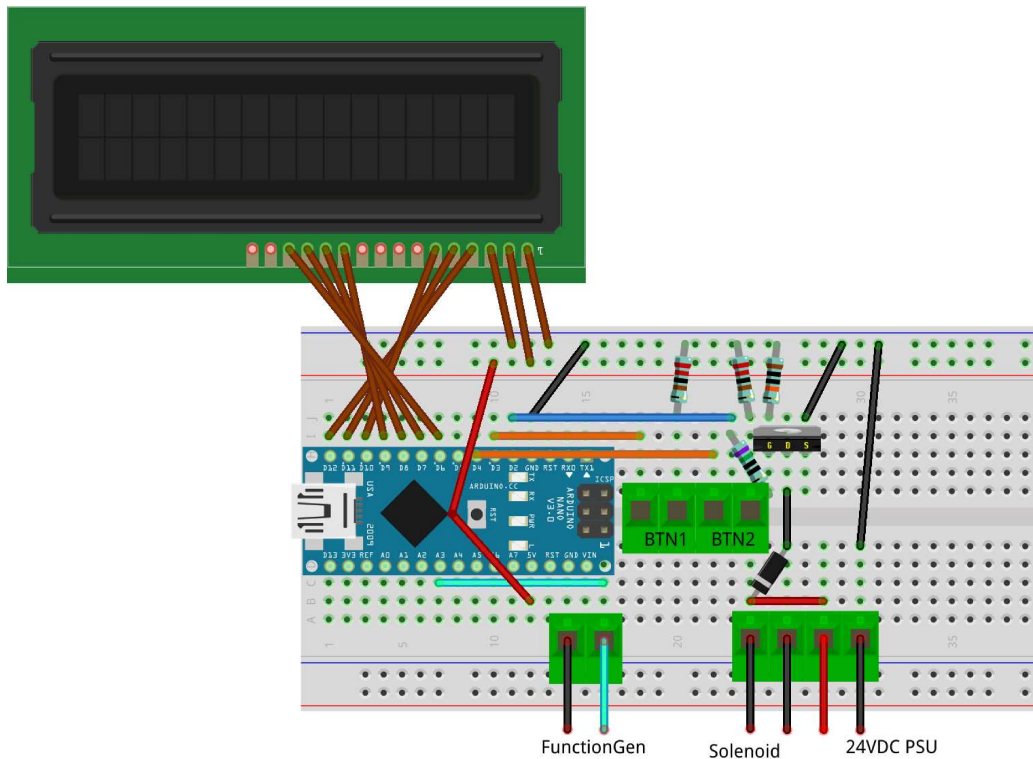


Figure C.1: Pulse generator breadboard design

## C.2 ZOC17 calibration solenoid circuit

The Scanivalve ZOC17 pressure-transducer unit has a calibration mode that requires two ports to be pressurized to 90psi. If these two ports are connected to a compressed air source through a solenoid, the process of setting the transducer into calibration

mode to obtain the zero-differential-pressure voltage of each sensor of the 16 channels of the transducer can be controlled by software, through a circuit shown in Figure C.2.

Although the circuit was built, the software was not written for this final system. Software can be written to emit a 5V digital signal from a computer, perhaps via a National Instrument IO device, to the CTRL+/- port of this circuit. This prompts the MOSFET (P/N: FQP30N06L) to close the 24VDC power circuit of the solenoid and thereby activating the calibration mode.

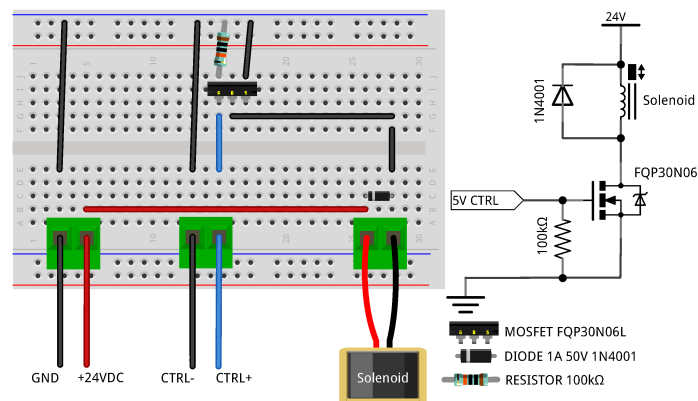


**Figure C.2:** Solenoid driver circuit

### C.3 ZOC17 channel selector

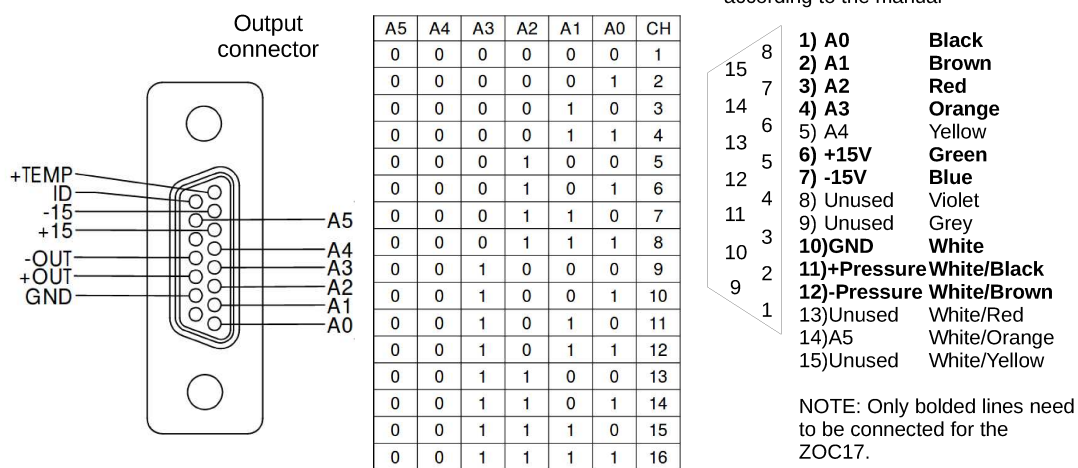
*Note: although this device was built, it was not integrated in the experiment.*

The Scanivalve ZOC17 pressure-transducer unit has 16 transducers each, although it can only output the signal of one transducer at a time. To select the desired output, certain input lines must be pulled to ground. The principle of operation is shown in Figure C.3. To control this in software, a MOSFET circuit is designed such that when a 5V signal is received, the A0-A4 lines on the ZOC17 are pulled to ground. The circuit diagram and layout schematic is shown in Figure C.4. An example C program that operates this circuit using the NIDAQmx library is shown in Listing C.2 for

reference. The functions defined can be dropped into a larger project and called as shown in the `main()` function. It should be noted that this program was not used and was only briefly tested.

### ZOC17/16Px Output Cheat Sheet

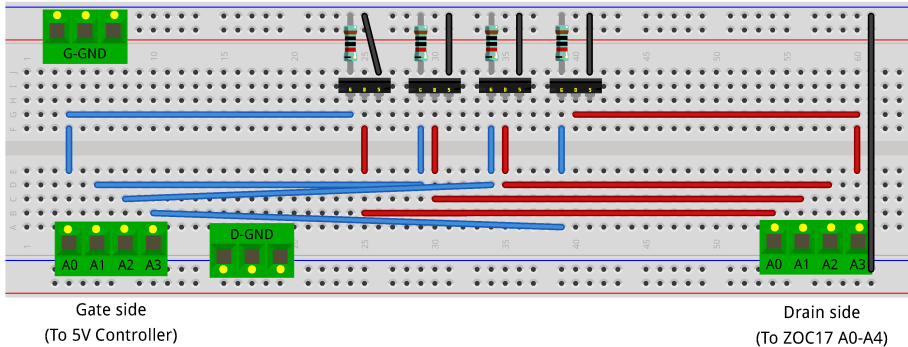
- 16 sensors, 2 calibration valves, 1 excitation board, 1 multiplexer/amplifier.
  - Sensors divided into 2 blocks of 8 sensors. All sensors in each block is referenced to the calibration/reference valve of the block.
- Powered by +/- 15V and also requires a connection to ground (Pin 6, 7, and 10). Required current is 100mA.
- Sensors are multiplexed and outputs a nominal +/- 2.5Vdc (Pin 11, 12)
  - Special factory configuration may have a +/-5V or +/-10V output range instead.
- Pin 9, 15 are unused. Pin 8, 13 is optional (temperature reading).



- To select a particular sensor (channel), send signal to A0-A5 (Port 1-5 and 14).
- A0-A5 are pulled high in the ZOC17. Ground them to send 0. If they're >11V, the ZOC will recognize it as 1.
- Sensor selection is based on the table above.
- Example: to select sensor (channel) 4, ground A2, A3, A4, A5 and send >11V to A0 and A1. Then, +OUT and -OUT will give the voltage for sensor 4.

**Figure C.3:** ZOC17 channel selection guide

## Breadboard View



- Yellow dots = pins TB006-508-03BE
- TB006-508-04BE
- N Channel MOSFET FQP30N06L
- 10 kΩ Resistor

### Instructions:

1. Plug gate side to a 3.3V/5V D/O port.
2. Plug the drain side into the ZOC17.
3. Plug D-GND into the ground of the ZOC17 power supply.
4. Plug G-GND into the ground of the DO port.
5. Send HIGH to A0-A4 on the gate side pulls A0-A4 on the ZOC to LOW, and vice versa.

## Schematic View (One Channel Shown)

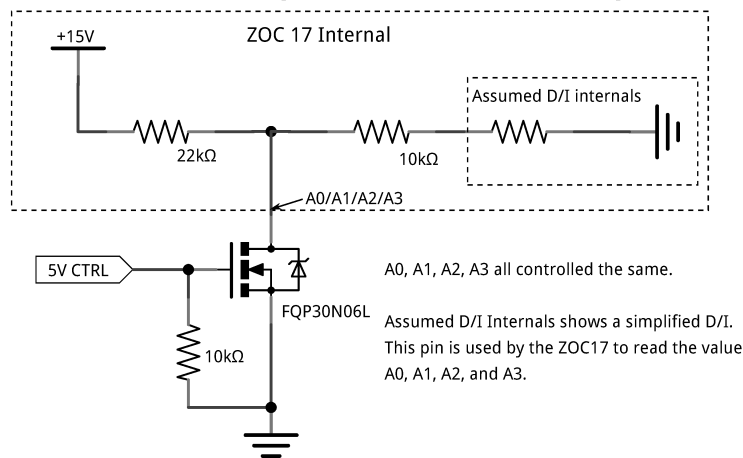


Figure C.4: ZOC17 channel selector circuit

## Listing C.2: ZOC17 channel selector program

```
#include <stdio.h>
#include <stdint.h>
#include "NIDAQmx.h"

int zoc17_g_daq_error = 0;
char zoc17_g_daq_error_msg[2048] = { 0 };

// Defines the number of ZOC17s we have.
#define NUMBER_OF_ZOC17 3
#define zoc17_daq_failed() DAQmxFailed(zoc17_g_daq_error)

TaskHandle zoc17_g_th_ax[NUMBER_OF_ZOC17] = { 0 };
TaskHandle zoc17_g_th_solenoid = 0;

static inline char* populate_daq_error_msg() {
    zoc17_g_daq_error_msg[0] = '\0'; // Ensure no buffer overflow occurs.
    if (zoc17_daq_failed()) DAQmxGetExtendedErrorInfo(zoc17_g_daq_error_msg, 2048);
    return zoc17_g_daq_error_msg;
}
```

```

static inline int check_zocidx(int zocidx) {
    if (zocidx >= 0 && zocidx < NUMBER_OF_ZOC17) {
        return 1;
    } else {
        zoc17_g_daq_error = -1;
        printf(
            "error: zocidx %d is not valid (must be between 0 and %d inclusive)\n",
            zocidx,
            NUMBER_OF_ZOC17 - 1
        );
        return 0;
    }
}

int zoc17_connect_to_ax(int zocidx, const char* ax_channels) {
    if (!check_zocidx(zocidx)) return zoc17_g_daq_error;

    zoc17_g_daq_error = DAQmxCreateTask("", &(zoc17_g_th_ax[zocidx]));
    if (zoc17_daq_failed()) return zoc17_g_daq_error;

    zoc17_g_daq_error = DAQmxCreateDOChan(
        zoc17_g_th_ax[zocidx],
        ax_channels,
        "",
        DAQmx_Val_ChanPerLine
    );
    return zoc17_g_daq_error;
}

int zoc17_connect_to_solenoid(const char* solenoid_channel) {
    zoc17_g_daq_error = DAQmxCreateTask("", &zoc17_g_th_solenoid);
    if (zoc17_daq_failed()) return zoc17_g_daq_error;

    zoc17_g_daq_error = DAQmxCreateDOChan(
        zoc17_g_th_solenoid,
        solenoid_channel,
        "",
        DAQmx_Val_ChanPerLine
    );
    return zoc17_g_daq_error;
}

int zoc17_select_transducer(int zocidx, uint8_t channel) {
    if (!check_zocidx(zocidx)) return zoc17_g_daq_error;

    int n = 0;
    uint8_t a[4] = { 1, 1, 1, 1 }; // A0, A1, A2, A3, defaults to channel 16
    switch (channel) {
        case 1:
            a[0] = 0; a[1] = 0; a[2] = 0; a[3] = 0;
            break;
        case 2:
            a[0] = 1; a[1] = 0; a[2] = 0; a[3] = 0;
            break;
        case 3:
            a[0] = 0; a[1] = 1; a[2] = 0; a[3] = 0;
            break;
        case 4:
            a[0] = 1; a[1] = 1; a[2] = 0; a[3] = 0;
            break;
    }
}

```

```

case 5:
a[0] = 0; a[1] = 0; a[2] = 1; a[3] = 0;
break;
case 6:
a[0] = 1; a[1] = 0; a[2] = 1; a[3] = 0;
break;
case 7:
a[0] = 0; a[1] = 1; a[2] = 1; a[3] = 0;
break;
case 8:
a[0] = 1; a[1] = 1; a[2] = 1; a[3] = 0;
break;
case 9:
a[0] = 0; a[1] = 0; a[2] = 0; a[3] = 1;
break;
case 10:
a[0] = 1; a[1] = 0; a[2] = 0; a[3] = 1;
break;
case 11:
a[0] = 0; a[1] = 1; a[2] = 0; a[3] = 1;
break;
case 12:
a[0] = 1; a[1] = 1; a[2] = 0; a[3] = 1;
break;
case 13:
a[0] = 0; a[1] = 0; a[2] = 1; a[3] = 1;
break;
case 14:
a[0] = 1; a[1] = 0; a[2] = 1; a[3] = 1;
break;
case 15:
a[0] = 0; a[1] = 1; a[2] = 1; a[3] = 1;
break;
case 16:
a[0] = 1; a[1] = 1; a[2] = 1; a[3] = 1;
break;
default:
    zoc17_g_daq_error = -1;
    printf(
        "error: incorrect channel specified (%d). value must be between 1 and 16.\n",
        channel
    );
    return zoc17_g_daq_error;
}

// Negated because the MOSFET inverts the bit sent to the ZOC.
// i.e. 1 to the MOSFET => 0 to the ZOC.
a[0] = !a[0]; a[1] = !a[1]; a[2] = !a[2]; a[3] = !a[3];

zoc17_g_daq_error = DAQmxWriteDigitalLines(
    zoc17_g_th_ax[zocidx],
    1,
    1,
    DAQmx_Val_WaitInfinitely,
    DAQmx_Val_GroupByChannel,
    a,
    &n,
    NULL
);
return zoc17_g_daq_error;
}

```

```
int zoc17_set_solenoid_valve(int opened) {
    uint8_t* data = { opened };
    zoc17_g_daq_error = DAQmxWriteDigitalLines(
        zoc17_g_th_solenoid,
        1,
        1,
        DAQmx_Val_WaitInfinitely,
        DAQmx_Val_GroupByChannel,
        data,
        NULL,
        NULL
    );
    return zoc17_g_daq_error;
}

int main() {
    zoc17_connect_to_ax(0, "Dev1/port0/line0:3");
    if (DAQmxFailed(zoc17_g_daq_error)) {
        printf("error while connecting to ZOC D/0: %s\n", populate_daq_error_msg());
        return 1;
    }

    zoc17_select_transducer(0, 1);
    if (DAQmxFailed(zoc17_g_daq_error)) {
        printf("error while selecting transducer: %s\n", populate_daq_error_msg());
        return 1;
    }

    return 0;
}
```

## Appendix D

# Supplemental material on the vortex filament method

Some of the implementation detail and the source code of the vortex filament algorithm described in Section 4.2 are contained in this appendix.

Since the velocity of each node is calculated based on the superposition of the induced velocity of every vortex segment, the algorithm to compute the next position of the entire vortex filament has a complexity of  $O(n^2)$ , where  $n$  is the total number of nodes. As such, the number of nodes must be kept at a reasonably small number to avoid a quadratic explosion in run time. However, as the vortex filament evolves during the computation, some segments are stretched to be very long and induce physically-inaccurate velocities on neighbouring nodes, causing the computation to diverge. This necessitates the division of the vortex segments as they stretch. Naïvely, the data structure representing the nodes of a vortex filament can be an 1D array. With such a data structure, every vortex division would result in a reallocation of the array, which would cause the overall algorithm to slow to  $O(n^3)$ . This results in unacceptable run times all vortex segment lengths of interest.

To get around this problem, a double-linked list is used to represent the vortex filament, where each node in the linked list represents a separate vortex segment node. As the algorithm iterates over each node and computes its next coordinates, division can simply be done via a double-linked-list insertion operation, which has a complexity of  $O(1)$ . Thus, the overall algorithm complexity remains to be  $O(n^2)$ , which was fast enough for physically accurate computations to be performed.

Additional optimizations were also developed in the code, but they had negligible impact in both the wall-clock duration of the computation and the position of the vortex filament at the end of each computation. As such, they were turned off for the analysis presented in the main text. These optimizations are (a) limiting the maximum range of influence of a particular vortex node and (b) the merging of neighbouring nodes when they are within a small distance of each other.

The final algorithm is written in Cython version 3 and displayed in Listing D.1.

#### Listing D.1: Vortex filament method source code

```
# cython: language_level=3

# Required libraries: numpy, scipy and VTK. VTK is used to export the vortex
# for post processing.
#
# To run this code, you must:
# 1. Compile this library via Cython possibly using some sort of setup.py
# 2. Import this library: from filament import Filament
# 3. Initialize the Filament with the right parameters (see source code for format):
# f = Filament(circulation, core_radius, max_sl, min_sl, max_range, coords, background_velocity)
# 4. Loop through the number of desired time step and call the step method on Filament:
# for i in range(n):
# f.save_single_timestep(fn_template)
# f.step()
#
# Reading the code below will be required to understand some of the parameters
# used in the function calls shown above. Familiarity with the VTK file format
# will help with the interpretation of the output files.

cimport numpy as np
from cpython.mem cimport PyMem_Malloc, PyMem_Free
from libc.math cimport sqrt, pi, sin

import numpy as np
import vtk
from vtk.util.numpy_support import numpy_to_vtk
from scipy.interpolate import interp1d
```

```

DTYPE = np.double
ctypedef np.double_t DTYPE_t

#####
# General Math #
#####

cpredef (double, double, double) cross(double x1,
                                       double y1,
                                       double z1,
                                       double x2,
                                       double y2,
                                       double z2) except *:

    return (
        y1 * z2 - z1 * y2,
        z1 * x2 - x1 * z2,
        x1 * y2 - y1 * x2,
    )

cpredef double norm(double x, double y, double z):
    return sqrt(x**2 + y**2 + z**2)

#####
# Background Velocity Functions #
#####

cpredef class SineBackgroundGenerator:
    cpredef DTYPE_t[:] amplitudes
    cpredef DTYPE_t[:] wavelengths
    cpredef DTYPE_t[:] phases
    cpredef np.int_t[:] directions
    cpredef int n
    cpredef object bottom_ufunc

    def __init__(self, background_velocity_file, amplitudes, wavelengths, phases, directions):
        self.amplitudes = amplitudes
        self.wavelengths = wavelengths
        self.phases = phases
        self.directions = directions

        self.n = self.directions.shape[0]

        data = np.load(background_velocity_file)
        self.bottom_ufunc = interp1d(data["y"], data["u"], kind="cubic")

    cpredef (double, double, double) evaluate(self, double x, double y, double z, int t) except *:
        cpredef double[3] v
        v[0] = self.bottom_ufunc(y)
        v[1] = 0.0
        v[2] = 0.0

        for i in range(self.n):
            v[self.directions[i]] += self.amplitudes[i] * sin(
                2 * pi / self.wavelengths[i] * (z + self.phases[i])
            )

        return v[0], v[1], v[2]

#####

```

```

# Filament Stuff #
#####

cdef struct Node:
    # This may be useful later to keep the point id in VTK constant so
    # the point don't move from timestep to timestep
    int id
    int born_on

    # Node information are valid for the node defined by xyz

    double x
    double y
    double z

    double vx
    double vy
    double vz

    double ivx
    double ivy
    double ivz

    # Vortex information for the present node are for the segment that's defined
    # by the current node and current.next.

    # A cached version of the node's coordinates
    double x_prev
    double y_prev
    double z_prev

    # Vortex center
    double vcx
    double vcy
    double vcz

    # Vortex length
    double sx
    double sy
    double sz
    double sl

    # Vortex strength
    double vol # volume should always be constant
    double r # radius changes depending on sl and vol.

    Node* prev
    Node* next

cdef Node* new_node(double x, double y, double z, double r, Node* prev, Node* next):
    cdef Node* node = <Node*> PyMem_Malloc(sizeof(Node))
    node.born_on = 0

    node.x = x
    node.y = y
    node.z = z

    node.vx = 0.0
    node.vy = 0.0
    node.vz = 0.0
    node.ivx = 0.0
    node.ivy = 0.0
    node.ivz = 0.0

```

```

# We cannot compute most of these as the filament needs to be completely
# constructed before they can be built.
node.x_prev = x
node.y_prev = y
node.z_prev = z

node.vcx = 0.0
node.vcy = 0.0
node.vcz = 0.0

node.sx = 0.0
node.sy = 0.0
node.sz = 0.0
node.sl = 0.0

node.vol = -1.0
node.r = r

node.prev = prev
node.next = next
return node

cdef class Filament:
    cdef int node_count
    cdef double circulation
    cdef double core_radius
    cdef double max_sl
    cdef double min_sl
    cdef double max_range
    cdef readonly int timestep
    cdef readonly double t
    cdef SineBackgroundGenerator background_velocity

    cdef Node* head
    cdef Node* tail

    cdef readonly int nodes_added
    cdef readonly int nodes_deleted

    def __cinit__(self,
                  double circulation,
                  double core_radius,
                  double max_sl,
                  double min_sl,
                  double max_range,
                  np.ndarray[DTYPE_t, ndim=2] coords,
                  SineBackgroundGenerator background_velocity):
        """
        circulation: circulation of the filament
        core_radius: the radius of the filament segment within where no velocity is induced.
                     this filters out the singularity.
        max_sl: the maximum length of the segment before splitting occurs.
        min_sl: the minimum length of the segment before merging occurs.
        max_range: the radius the filament segment outside where no velocity is induced.
                     this filters out the consistent influence from the edges?
        coords: the initial coordinates.
        """
        cdef double x, y, z
        cdef Node* prev_node
        cdef Node* current_node

```

```

self.node_count = coords.shape[0]
self.timestep = 0
self.circulation = circulation
self.core_radius = core_radius
self.max_sl = max_sl
self.min_sl = min_sl
self.max_range = max_range
self.background_velocity = background_velocity

self.nodes_added, self.nodes_deleted = 0, 0

if self.node_count < 2:
    raise ValueError("Must have at least two nodes")

x = coords[0, 0]
y = coords[0, 1]
z = coords[0, 2]
self.head = new_node(x, y, z, core_radius, NULL, NULL)
self.head.vx, self.head.vy, self.head.vz = self.background_velocity.evaluate(x, y, z, 0)
if not self.head:
    raise MemoryError()

prev_node = self.head
for i in range(1, self.node_count):
    x = coords[i, 0]
    y = coords[i, 1]
    z = coords[i, 2]

    current_node = new_node(x, y, z, core_radius, prev_node, NULL)
    current_node.vx, current_node.vy, current_node.vz = self.background_velocity.evaluate(
        x, y, z, 0
    )

    # Hook up nodes and compute segment property
    prev_node.next = current_node
    self.compute_single_segment_geometric_property(prev_node)
    prev_node.vol = pi * prev_node.r**2 * prev_node.sl

    prev_node = current_node

self.tail = current_node

def __dealloc__(self):
    cdef Node* current
    cdef Node* next

    current = self.head
    while current != NULL:
        PyMem_Free(current)
        next = current.next
        current = next

#####
# Operations to step through #
#####

cpdef step(self, double dt):
    # Compute the vortex center and lengths for the current timestep.
    # This is done before movement so the vortex segments are fixed when
    # induced velocities.
    #
    # Also splits a segment into two if it grows too long

```

```

self.compute_segments_and_repartition_if_needed()

# Actually move the nodes via induction
self.move_nodes_via_induction(dt)

# Bookkeeping
self.timestep += 1
self.t += dt

cdef compute_segments_and_repartition_if_needed(self):
    cdef Node* n1
    cdef Node* n2

    n1 = self.head
    n2 = self.head.next
    while n2 != NULL:
        self.compute_single_segment_geometric_property(n1)

        if n1.sl > self.max_sl:
            self.split_segment(n1, n2)
            self.nodes_added += 1
        elif n1.sl < self.min_sl and n1 != self.head:
            self.merge_segment(n1, n2)
            self.nodes_deleted += 1

        n1 = n2
        n2 = n2.next

cdef move_nodes_via_induction(self, double dt):
    cdef Node* ctrl_node
    cdef Node* vortex_node1
    cdef Node* vortex_node2

    cdef double rx, ry, rz, rl, k, u, v, w

    ctrl_node = self.head
    while ctrl_node != NULL:
        ctrl_node.vx, ctrl_node.vy, ctrl_node.vz = self.background_velocity.evaluate(
            ctrl_node.x,
            ctrl_node.y,
            ctrl_node.z,
            self.timestep
        )
        ctrl_node.ivx, ctrl_node.ivy, ctrl_node.ivz = 0.0, 0.0, 0.0

        vortex_node1 = self.head
        vortex_node2 = self.head.next
        while vortex_node2 != NULL:
            if self.influenced_by_segment(ctrl_node.x, ctrl_node.y, ctrl_node.z, vortex_node1):
                rx = ctrl_node.x - vortex_node1.vcx
                ry = ctrl_node.y - vortex_node1.vcy
                rz = ctrl_node.z - vortex_node1.vcz
                rl = norm(rx, ry, rz)

                k = self.circulation / (4 * pi * rl**3)

                u, v, w = cross(
                    vortex_node1.sx,
                    vortex_node1.sy,
                    vortex_node1.sz,
                    rx,
                    ry,

```

```

        rz
    )

    u *= k
    v *= k
    w *= k

    ctrl_node.ivx += u
    ctrl_node.ivy += v
    ctrl_node.ivz += w

    vortex_node1 = vortex_node2
    vortex_node2 = vortex_node2.next

    ctrl_node.vx += ctrl_node.ivx
    ctrl_node.vy += ctrl_node.ivy
    ctrl_node.vz += ctrl_node.ivz

    ctrl_node.x += ctrl_node.vx * dt
    ctrl_node.y += ctrl_node.vy * dt
    ctrl_node.z += ctrl_node.vz * dt

    ctrl_node = ctrl_node.next

#####
# Segment helpers #
#####
cdef split_segment(self, Node* n1, Node* n2):
    cdef Node* nmid

    nmid = new_node(n1.vcx, n1.vcy, n1.vcz, self.core_radius, n1, n2)
    nmid.born_on = self.timestep

    n1.next = nmid
    n2.prev = nmid
    self.node_count += 1

    # Need to recompute the length and vortex centers
    self.compute_single_segment_geometric_property(n1)
    self.compute_single_segment_geometric_property(nmid)

cdef merge_segment(self, Node *n1, Node *n2):
    n2.x = n1.vcx
    n2.y = n1.vcy
    n2.z = n1.vcz

    n2.born_on = self.timestep

    n2.prev = n1.prev
    n2.prev.next = n2

    self.node_count -= 1
    PyMem_Free(n1)

    self.compute_single_segment_geometric_property(n2)

cdef compute_single_segment_geometric_property(self, Node* n1):
    cdef Node* n2

    n2 = n1.next
    n1.vcx = (n1.x + n2.x) / 2.0
    n1.vcy = (n1.y + n2.y) / 2.0

```

```

n1.vcz = (n1.z + n2.z) / 2.0

n1.sx = n2.x - n1.x
n1.sy = n2.y - n1.y
n1.sz = n2.z - n1.z
n1.sl = norm(n1.sx, n1.sy, n1.sz)

n1.x_prev = n1.x
n1.y_prev = n1.y
n1.z_prev = n1.z

cdef bint influenced_by_segment(self, double x, double y, double z, Node* n1) except *:
    cdef double radius_of_influence, distance

    # First check if the segment is even close to the point in a spherical
    # sense.
    #
    # This sphere is just big enough to capture the cylinder that defines the
    # core.
    radius_of_influence = sqrt(n1.r**2 + (n1.sl / 2)**2)
    distance = sqrt((x - n1.vcx)**2 + (y - n1.vcy)**2 + (z - n1.vcz)**2)

    if distance < radius_of_influence:
        # If we're in the core, then find the perpendicular distance to the
        # segment
        distance = self.perpendicular_distance_to_segment(x, y, z, n1)

    return distance > n1.r and distance < self.max_range

cdef double perpendicular_distance_to_segment(
    self, double x, double y, double z, Node* n1
) except *:
    # Calculates the perpendicular distance to the line.
    # Using the cross product method
    # See also: http://mathworld.wolfram.com/Point-LineDistance3-Dimensional.html
    cdef double vec12x, vec12y, vec12z, vec01x, vec01y, vec01z
    vec12x, vec12y, vec12z = n1.sx, n1.sy, n1.sz
    vec01x, vec01y, vec01z = n1.x_prev - x, n1.y_prev - y, n1.z_prev - z

    # overwritten to save variable space
    vec01x, vec01y, vec01z = cross(vec12x, vec12y, vec12z, vec01x, vec01y, vec01z)
    return norm(vec01x, vec01y, vec01z) / norm(vec12x, vec12y, vec12z)

#####
# IO Helpers #
#####

cpdef str save_single_timestep(self, str fn_template):
    cdef Node* current
    cdef int i = 0
    cdef np.ndarray[np.int_t, ndim=1] point_ids
    cdef np.ndarray[DTYPE_t, ndim=2] velocities
    cdef np.ndarray[DTYPE_t, ndim=2] induced_velocities
    cdef np.ndarray[DTYPE_t, ndim=1] core_radiuses

    points = vtk.vtkPoints()
    points.SetNumberOfPoints(self.node_count)
    ugrid = vtk.vtkUnstructuredGrid()
    ugrid.Allocate(1)

    point_ids = np.empty(self.node_count, dtype=np.int)

```

```

velocities = np.empty((self.node_count, 3))
induced_velocities = np.empty((self.node_count, 3))
core_radiuses = np.empty(self.node_count)

current = self.head
while current != NULL:
    points.SetPoint(i, current.x, current.y, current.z)
    point_ids[i] = i

    velocities[i, 0] = current.vx
    velocities[i, 1] = current.vy
    velocities[i, 2] = current.vz

    induced_velocities[i, 0] = current.ivx
    induced_velocities[i, 1] = current.ivy
    induced_velocities[i, 2] = current.ivz

    core_radiuses[i] = current.r

    current = current.next
    i += 1

velocity_array = numpy_to_vtk(velocities)
induced_velocity_array = numpy_to_vtk(induced_velocities)
circulation_array = numpy_to_vtk(np.ones(self.node_count) * self.circulation)
core_radius_array = numpy_to_vtk(core_radiuses)

velocity_array.SetName("Velocity")
induced_velocity_array.SetName("InducedVelocity")
circulation_array.SetName("Circulation")
core_radius_array.SetName("CoreRadius")

ugrid.SetPoints(points)
ugrid.InsertNextCell(vtk.VTK_LINE, point_ids.shape[0], point_ids)
pd = ugrid.GetPointData()
pd.AddArray(velocity_array)
pd.AddArray(induced_velocity_array)
pd.AddArray(circulation_array)
pd.AddArray(core_radius_array)

writer = vtk.vtkXMLUnstructuredGridWriter()
fn = fn_template.format(self.timestep)
writer.SetFileName(fn)
writer.SetInputData(ugrid)
writer.Write()
return fn

cpdef coords(self):
    cdef Node* current
    cdef np.ndarray[DTYPE_t, ndim=3] coords

    coords = np.empty((self.node_count, 3))
    i = 0
    current = self.head
    while current != NULL:
        coords[i, 0] = current.x
        coords[i, 1] = current.y
        coords[i, 2] = current.z
        current = current.next

```

```
    i += 1

cpdef dump(self):
    cdef Node* current
    current = self.head
    while current != NULL:
        print("{}: {} {} {} ({}).format(current.x, current.y, current.z, current.next == NULL))
        current = current.next
```